A COMPREHENSIVE METHODOLOGY FOR WELL RAMP-UP OF OPEN HOLE

STAND-ALONE SCREEN COMPLETIONS

by
Mehmet Emin Karaaslan

A Dissertation submitted to the Faculty of the Department of Petroleum Engineering
University of Houston
in partial fulfillment of the requirements for the Degree of

Doctor of Philosophy

in Petroleum Engineering

Chair of Committee: Dr. George K. Wong

Committee Member: Dr. Mohamed Y. Soliman

Committee Member: Dr. Majeed Yousif

Committee Member: Dr. Konstantinos Kostarelos

Committee Member: Dr. Lori Hathon

University of Houston
May 2020

Acknowledgments

I would like to thank Dr. George K. Wong who guided me in every step of my research and made me confident during the challenging PhD work. I am honored to be his first PhD graduate at the University of Houston. I would like to thank Dr. Majeed Yousif for sponsoring this project and for his guidance throughout this study. Thanks are due also to Dr. Lori Hathon for the CT scan measurements of test samples and her help with the scan results. I would also like to thank Dr. Mohamed Y. Soliman and Dr. Konstantinos Kostarelos for serving as committee members and providing support during my PhD study. I also appreciate to Dr. Ali Rezai for his encouraging support during my study at the University of Houston. Finally, I want to thank my lovely wife, Sinem, for her patience and support throughout my study.

Abstract

Following the unloading of completion fluids, wells face the most critical step of ramping up production toward a peak rate for the first time. The challenge is delivering the maximum rate with limited well performance information and without damaging the completion integrity at the same time.

This research develops a production surveillance methodology to monitor and ramp-up production for open hole stand-alone screen (OH-SAS) completion that optimizes production by considering risks of production impairment and screen erosion failure. Laboratory evaluations of drill-in fluids showed non-uniform filter cake clean-up or presence of "pinholes" resulting in concentrated inflow around the wellbore. A combination of laboratory return permeability tests, CT scans and a developed reduced order model determines the pinhole size and filter cake properties to calculate the total pinhole flow area or concentrated inflow velocity using an established relationship. The pinhole inflow velocity is distributed into the radial and axial annular flow velocities in the OH-SAS wellbore using a network flow model to assess the screen erosion failure risks from direct impingement and convergence at the top of the screen assembly, respectively. The ramp-up strategy is to use successive PBU data of increasing production rates and evaluate the absolute and relative changes of completion pressure drop and velocities against established failure criteria.

The application of filter cake properties and PBU data showed the internal filter cake permeability has the most dominant effect on the inflow velocity. The completion pressure drop as a function of flow rate is non-linear and higher than the case without

pinholes. Results from the network model showed that convergent velocity is higher than the impingement velocity. Adding screen above the pay interval reduces the screen impingement erosion risk but increases the annular scouring risk. Scouring velocity is found to be significantly higher than the convergent velocity. This highlights the need to consider screen and borehole failure due to scouring erosion. The convergent velocities for pinhole and non-pinhole cases were similar and the implementation of pinhole in this methodology only affected the completion pressure drop or the completion impairment risk.

Table of Contents

List of Tables

List of Figures

Nomenclature

Acronyms

AC	Annular Clearance
ANAVO	Abbreviated from Analysis of Variance
bbls	Barrels
cm	Centimeters
CT	Computed Tomography
ID	Internal Diameter, inch
DPcom	Completion Pressure Drop
RPT	Return Permeability Test
HPHT	High Pressure High Temperature
ml	Milliliter
OFA	Open Flow Area Percentage (%)
OH-SAS	Open Hole Stand Alone Screen
PBU	pressure build-ups
psi	Pounds per square inch
PTA	Pressure Transient Analysis
ppg	pound per gallon
ROM	Reduced Order Model
SB-DIF	Synthetic Based Drill-in fluid
SBM	Synthetic Based Mud
Stbpd	Standard Barrel per Day

UFA	Unit Flow Area
WB-DIF	Water Based Drill-in fluid
WBM	Water Based Mud

Symbols

A	Area, cm^2
cP	Centipoise
E_k	Kinetic Energy
E_p	Potential Energy
F	Forchheimer number
f_t	turbulence scale factor
g	acceleration due to gravity, m/s^2
h	Height, inch or cm
ΔH	Net Rate of Enthalpy flow out of an Open system
k	permeability, md
L	Length, inch or cm
m	mass
p	pressure, psia
Δp	pressure drop, psi
$Q_{in,CV}$	Rate of heat into Control volume
r	radius, inch
q	rate, bpd

s	screen, skin
t	term
U	Internal Energy
V	Velocity, ft/s
W$_{by,cv}$	Work done by fluid in the Control Volume

Greek

μ	viscosity, cp
ρ	density, g/cm^3
β_{Ds}	Dimensionless scale factor
ξ	Flowpath coordinate

Subscripts

a	axial
c	completion
cv	Control volume
ec	external cake
int	internal
mc	mud cake
t	total

Chapter 1

Introduction

The open hole stand-alone screen (OH-SAS) is becoming a preferred sand control completion for reservoir rock that has some cohesion strength. In such a completion, casing or liner is installed above or in the formation. The reservoir section is drilled and left as an open hole, i.e., it has neither casing nor liner. Only a sand screen is installed in the completion interval to produce with sand control. The installation process is simpler and more cost efficient as compared to open hole gravel pack completion. However, without gravel pack supporting the borehole, some rock cohesion strength is needed to prevent borehole collapse during production which can localize flow and cause completion failure. Figure 1-1 presents a schematic of a typical OH-SAS completion.
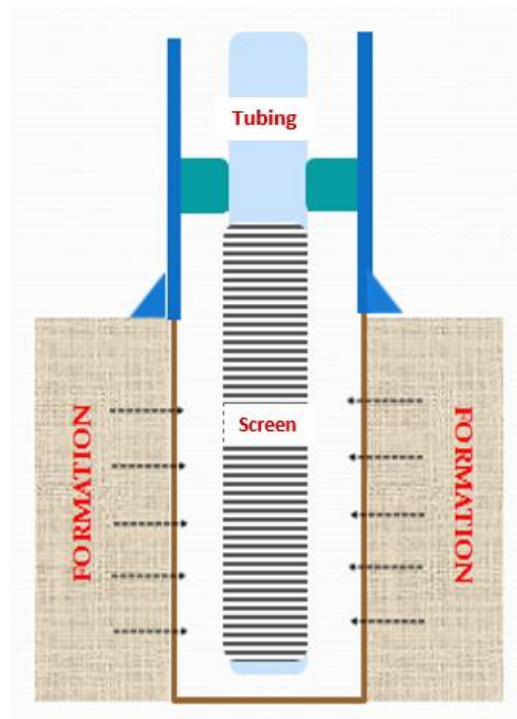
Figure 1-1: Schematic of OH-SAS Completion

Since production comes from open hole, the drilling fluid for the reservoir section can affect well productivity (Hodge, Burton, Fischer, & Constien, 2010). Unlike conventional drilling mud, this fluid is known as a reservoir drilling fluid or drill-in fluid (DIF). It is designed to minimize formation damage for optimum well productivity (Van Zanten, Horton, & Tanche-Larsen, 2011).

Following the well completion, the process of producing a new well generally involves following operations:

➢ Unload the completion fluids: This process consists of producing the completion fluids and lifting the solids from the wellbore. Depending on the reservoir temperature and suspension time prior to unloading, a lower portion of the OH-SAS interval might be covered with settled weighting solids in the DIF.

➢ Bean-up (choke change strategy): This step is an engineered sequence of choke setting which gradually increases the production to achieve the target rate.

➢ Ramp-up production to peak rate: Reaching the maximum target production rate for the first time.

➢ Re-start production after a shut-in: This is the process of opening up a well after an expected or unexpected shut down.

This dissertation focuses on ramp-up methodology for OH-SAS completions.

1.1 Motivation and Objective

After unloading, the well faces the most critical step of ramping up production toward its designed peak rate for the first time. The challenge is delivering this maximum rate with limited well performance information and without compromising the completion

integrity at the same time. Therefore, having surveillance information during the ramp-up process is critical in making proper adjustments and avoiding well impairment or failure before reaching the peak production rate.

Currently, there are limited monitoring tools installed across the completion interval with real-time data to help production engineers make real-time decision during the ramp-up process. Typically, the only available surveillance information is from pressure build-up (PBU) data measured by downhole pressure gauges. PBU uses the flowing and shut-in pressure data and the pressure transient analysis (PTA) method to calculate the reservoir properties and completion skin pressure drop (DPcom). The use of PBU data and PTA results provides a viable surveillance approach for well ramp-up operations.

The main objective of this research is to develop and present a production surveillance methodology to monitor and ramp-up production for OH-SAS completion. The aim is to ramp-up the well safely and optimize production by taking into account the risks of completion impairment or failure. The methodology utilizes reservoir, completion, and PBU data and develops an open hole filter-cake flow model with DPcom to calculate an average wellbore inflow velocity (V_c). This inflow is then distributed into the OH-SAS geometry as a direct screen impingement velocity (V_s) and the annular flow velocity at the top of screen or convergent velocity (V_a). Values of V_s, V_a and DPcom are used to monitor and operate the ramp-up operations by minimizing screen erosion failure and completion impairment risks. The strategy is to use successive PBU data of increasing production rates and evaluating the absolute and relative changes of V_s, V_a, and DPcom.

These provide a direct surveillance feedback to help adjust the ramp-up process. The methodology includes the followings:

➢ Choose impairment and failure mechanisms and associated criteria.

➢ Develop models to diagnose well performance and completion flow velocities.

➢ Propose a practical strategy of using diagnosed data to forecast well performance and failure risks for well ramp-up.

Finally, example and sensitivity analysis will be presented to demonstrate the performance of the developed methodology and identify areas of further studies.

1.2 Outline

This section describes the content of each chapter of the dissertation. Chapter 1 gives general information about OH-SAS completions and the importance of developing a ramp-up method for real-time surveillance. Chapter 2 describes the key requirements and strategy for a well ramp-up operation. Chapter 3 provides information about the experiments, measurements and models to determine input properties of the filter cake created by the DIF. Chapter 4 explains the relationship between completion pressure drop and flow through pinholes from the filter cake to estimate the inflow velocity V_c. Chapter 5 presents the development of network modeling of OH-SAS system and calculates the distribution of V_c into V_s and V_a. Chapter 6 shows example results and discusses their applications and implications. Finally, Chapter 7 summarizes the conclusions and recommendations for future studies.

Chapter 2

Production Ramp-up Methodology

This chapter presents the key requirements and strategy for the ramp-up of OH-SAS. A review of published literature is presented first, which followed with a summary of requirements for the ramp-up methodology.

2.1 Pertinent Literature on Production Ramp-up and Screen Failure

Numerous studies have been published on operation limits of maximum drawdown and velocity without a direct method to link back to surveillance data, such as PBU. Tiffin et al. (2003) recommended a range of completion drawdown limits between 500 psi and 1000 psi. This paper also proposed a simple correlation for determining the maximum safe production rate or flux for sand control wells. The correlation was developed based on data collected from 200 cased-hole gravel packs and fracpacks. The authors concluded that production rate that is too high or too low would result in unacceptable well failure rate or loss of production, respectively. Vaziri et al. (2002) conducted a comprehensive sand failure study and proposed drawdown guidelines and near wellbore velocity limits based on formation shear/tensile failures. A production impairment model based on fines mobilization caused by transient pressure gradient for bean-up operations was presented by Geilikman et al. (2005). The authors recommended carrying out smaller incremental drawdown steps and shorter time intervals between choke opening changes. Karantinos et al. (2015) proposed a choke management strategy to maximize well performance by reducing formation damage and sand production. Their results showed that selection of the best economic strategy depends on the length of ramp-up period.

There are limited surveillance methodologies that adjust the ramp-up operations based on well performance results from PBU data. Wong et al. (2003) presented a method for cased-hole gravel pack and fracpack completions. The method uses DPcom from PBU to calculate the perforation flow velocity at the casing inside diameter (V_c) and on the screen outside diameter (V_s). Using well failure data from the Gulf of Mexico, the paper proposed completion failure limits for gravel destabilization at V_c < 10 ft/s and screen erosion at V_s < 1 ft/s. The paper also provided three field examples to demonstrate a surveillance strategy of using successive PTA results, with increasing production rates, to assess completion performances and adjust the ramp-up operations.

Cameron et al. (2018) developed a probabilistic flux, erosion model and workflow to calculate the flow through sand screen along the wellbore utilizing wellbore, completion and reservoir properties. The authors presented four mechanisms for sand screen erosion namely; fines migration, poor annular pack, sand particles and direct impingement through voids. For velocity prediction, a coupled reservoir and wellbore flow simulator is used with input parameters of fracture geometry, perforation geometry, perforation efficiency and proppant pack permeability with reservoir properties. Based on the workflow, perforation velocities above 4 ft/s may result in pack destabilization under certain conditions. The authors applied CFD simulations to model and understand sand screen erosion mechanisms and the most influential parameters. They concluded that conventional guidelines, which give simple flux limits do not consider cumulative effect of sand production. Sand properties such as particle size range, shape, etc. are uncertain and the application of in-situ flow, acoustic, temperature and pressure monitoring may

provide additional insights. A screen erosion study to identify the flow parameters that effect screen erosion was presented by Procyk et al. (2015), which attempted to provide guidelines for safe operation of cased-hole frack pack and cased-hole gravel pack completions. Experiments on erosion and CFD simulations are conducted to determine erosion damage and to visualize particle flow paths. Based on the analysis, an operational envelope is provided for well operating limits using sand concentrations and screen inlet velocity (assumed to the perforation flow velocity) to identify safe operating limits for various service life. Based on the chart, velocities above 10 ft/s may decrease the service life of a screen to less than one year for cased-hole gravel pack system (Procyk et al., 2015). Mahmoudi et al. (2018) investigated standalone screen failures focusing on plugging. The authors analyzed macroscopic and microscopic plugging of different screen types. Based on the analysis of wire wrap screen samples, they observed severe erosion-corrosion of base pipe which resulted in significant mass loss and thickness reduction in the base pipe. Also, significant plugging of annular space between the base pipe and screen was observed.

For open hole sand control completions, different completion design factors affecting completion impairment and failure have been identified. Burton et al. (2010) compared open hole gravel pack and OH-SAS performances using analytical and experimental results. They identified and discussed different possible mechanisms that can impact open hole completion performance and failure. For OH-SAS they suggested the following failure mechanisms:

➢ Ineffective sand screen design leading to screen plugging & screen erosion

- ➢ Ineffective drilling mud and mud cake clean-up leading to loss of productivity

- ➢ Ineffective corrosion inhibition of the screen leading to screen corrosion failure

For open hole gravel pack, the interactions between the drilling fluid and its clean-up can be more significant. Using laboratory tests which closely emulated downhole conditions, Hodge et al. (2010) provided the following observations: The drilling filter cake is harder to clean-up with gravel pack in-place. A filter cake that is not effectively cleaned-up would lead to smaller inflow area. This would result in concentrated flow with impaired productivity and increased screen erosion risks.

Conclusions from Burton et al. (2010) and Hodge et al. (2010) highlighted the dominant effect of ineffective filter cake clean-up to wellbore concentrated inflow. This leads to increased DPcom or production impairment and screen erosion failure. In this study, both production impairment and screen erosion mechanisms are incorporated in the ramp-up methodology for OH-SAS.

2.2 Production Ramp-up Components

This section discusses the different components and steps, which are used to develop the ramp-up methodology for OH-SAS. This dissertation will follow closely the approach used in cased- hole gravel pack and fracpack completions by Wong et al. (2003). The section begins by comparing and discussing the ramp-up methodology requirements or components between the cased hole and OH-SAS. The section then ends by outlining and summarizing the different components or steps of the methodology with a flowchart shown in Appendix A. Table 2-1 presents the ramp-up methodologies of cased hole

(Wong et al., 2003) and OH-SAS completions. The table emphasizes the different and additional challenges that OH-SAS completion needs to be addressed.

Table 2-1: Ramp-up Methodology for Cased Hole Gravel Pack and OH-SAS

	Cased Hole Gravel Pack (Wong et al. 2003)	OH-SAS Completion
Mechanism & Failure criteria	➢ Well impairment (DPcom) ➢ Gravel Instability (V_c) ➢ Screen Erosion (V_s)	➢ Well impairment (DPcom) ➢ Screen erosion as direct impingement on screen (V_s) and screen erosion at the top of screen assembly (V_a)
Completion Inputs	➢ Perforation diameter and tunnel length ➢ Perforation's gravel permeability & beta factor	➢ Average filter-cake pinhole diameter ➢ Filter cake permeability & thickness
Surveillance DPcom & flow model. Completion flow geometry	➢ Linear flow in gravel packed perforation tunnel ➢ Flow from perforation (V_c) through gravel pack to screen (V_s)	➢ Formation radial to hemispherical flow through pinholes ➢ Pinhole inflow (V_c) to impingement flow velocity on screen (V_s) and convergent flow velocity (V_a) at the screen top
Ramp-up Strategy	Multiple ramp-up steps with PBU after each step	

The completion impairment and failure mechanisms and associated failure criteria are presented first. For a cased hole, there are perforations packed with impaired gravel. These perforations would lead to increased DPcom and concentrated flow velocities that can destabilize the annulus gravel pack (V_c) and screen erosion (V_s). With a casing installed in the wellbore, a high DPcom limit between 1000 and 1500 psi can be tolerated while the V_c and V_s limits of 10 ft/s and 1 ft/s were proposed by Wong et al. (2003). For open hole, as discussed by Burton et al. (2010) and Hodge et al. (2010), the filter cake clean-up is not always effective or uniform, which leaves the filter cake with non-uniform clean-up

or with "pinholes." This results in increased DPcom and concentrated flow. Without the annular gravel pack, the OH-SAS only considers screen erosion. This consists of direct impingement screen erosion (V_s) and converging velocity at the top of the screen assembly (V_a). Similar to cased hole a screen erosion limit of 1 ft/s for both V_s and V_a is assumed. For open hole and without the casing support, the limit for DPcom on borehole collapse is not considered. The assumption is that during the ramp-up process reservoir depletion has not yet taken place and the effect of DPcom alone on borehole collapse is small.

For the comparison of completion inputs, the cased-hole gravel pack needs inputs of perforation diameter and tunnel length which are known completion quantities. The remaining inputs of impaired gravel permeability and beta factor (for non-darcy flow) are obtained through field calibration data (Wong et al., 2003). For OH-SAS, on the other hand, the required inputs of pinhole diameter, filter cake permeability and thickness are not known and determined using experimental and computational methods. Chapter 3 discusses the necessary approaches to determine these inputs for a given DIF, reservoir conditions, and formation rock properties.

For the surveillance DPcom and flow model, there are major differences between the cased hole and open hole completions. The pressure drop and flow equation for a gravel packed perforation with known diameter and length are based on Darcy's flow with non-darcy flow component due to the expected high or concentrated flow rate (Wong et al.,2003). However, the pressure drop and flow equation for filter cake pinholes and filter cake damage in an open hole would involve radial and hemispherical flows, which is more

complex, as given by Furui et al. (2003). The solution of V_c or downhole flow area of

perforations and pinholes for cased hole and open hole completion, respectively is

determined by setting the flow pressure drop equals to DPcom from PTA. This approach

enables a direct link of using well surveillance results into the ramp-up process. Having

the V_c value the flow distribution through the cased-hole gravel pack or OH-SAS can be

obtained. However, the flow geometry and velocity distributions are significantly

different for these two completions. For the cased-hole gravel pack, the flow velocity

exiting the packed perforation (V_c) will mostly flow radially across the annular gravel pack

to the outside diameter of the screen (V_s). For the OH-SAS, without the annular gravel

pack, the inflow V_c will be separated into radial and axial flow components through the

annular region and into the screen. The radial flow gives the direct screen impingement

velocity V_s and the convergent velocity at the top of the screen, V_a. Solutions of V_s and V_a

from V_c will be discussed in Chapter 5.

The ramp-up strategy for both cased hole gravel pack and OH-SAS completions is

similar. The strategy uses multiple ramp-up steps with PTA following each step before

reaching the desired peak production rate. Using the PTA results after each rate enables

surveillance engineers to assess the well performance and the failure risks before deciding

to maintain or ramp-up to the next rate.

In this dissertation the components of the production ramp-up methodology are

organized and summarized as follows:

1. <u>Filter cake pinhole properties:</u> For open hole completion the filter cake is known to

     not clean-up uniformly, which results in the formation of pinholes that lead to

concentrated production flow. The filter cake clean-up performance depends on DIF, rock properties, and reservoir temperature and pressure conditions. Our approach needs three filter cake inputs, including a representative pinhole diameter, the filter cake permeability, and the filter cake thickness. These filter cake properties are determined using a combination of laboratory test named return permeability test (RPT), computer tomography (CT) scan of test samples, and modeling. Chapter 3 discusses RPT, CT-Scan and modeling approaches to determine these filter cake input parameters for the ramp-up methodology.

2. <u>Well Inflow Analysis:</u> The relationship between pressure drop and fluid flow through pinholes is established using results presented by Furui et al. (2003). Equating the known DPcom from PTA with the pinhole's pressure drop would solve the total pinhole flow area or velocity V_c. Chapter 4 presents these equations.

3. <u>Wellbore flow rate distribution:</u> After the pinhole or wellbore inflow velocity V_c is obtained, the next step is to calculate flow rate and velocity distribution in the OH-SAS completion. Figure 2-1 depicts a schematic of the flow distribution.   A network model will be built for the OH-SAS geometry to calculate the distribution of V_c into the impinging velocity on the sand screen (V_s) and converging through the screen (V_a) at the top of completion interval. Chapter 5 provides the formulation of this network model.
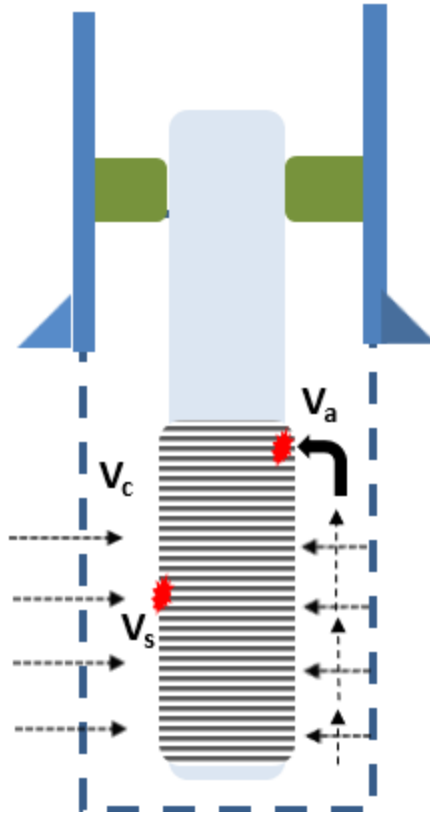
Figure 2-1: Schematic of Velocities in OH-SAS well

Appendix A shows a flow chart and summarizes these components.

Chapter 3

Filter Cake Pinhole Properties and Inputs

This chapter explains the pinholes phenomena in an OH-SAS completion and the procedures to determine the properties of the pinhole and filter cake, such as: pinhole diameter, filter cake thickness and permeability from laboratory testing and modeling. Depending on the design and effectiveness of the breakers in the DIF, laboratory experiments have shown non-uniform filter cake clean-up. Field production usually flows through a filter cake with pinholes.

Experimental observations show that the filter cake does not clean-up uniformly and there are "pinholes" that would lead to concentrated flow. Pinholing is a phenomenon where the filter-cake deforms locally and creates openings to enable fluid flow. Figure 3-1 shows photos of a filter cake from a water-based mud with visible pinholes (Cerasi & Soga 2001) and a filter cake from a synthetic based drill-in fluid where the presence of pinholes is not visible through the external filter cake.
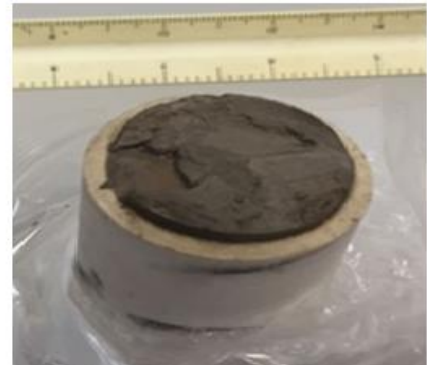
Figure 3-1: Picture of Pinholes in a WBM (Cerasi & Soga, 2001) and Non-Visible Pinholes in a SBM

Pinholes and filter cakes properties are formation and drill-in fluid (DIF) specific. They can be determined from a laboratory Return Permeability Test (RPT) and CT scans. Following sections will describe the experiments and measurements that are conducted for identifying the properties of the pinhole and filter cake.

3.1 Return Permeability Test Experiments

Drilling mud filter cake is a layer created by solid particles around the wellbore due to the pressure difference between fluid hydrostatic pressure and formation pressure. Figure 3-2 shows the schematics of the wellbore from side and top view to illustrate the external filter (mud) cake and internal filter cake. The internal filter cake is the result of filtration of the drilling mud into the formation.
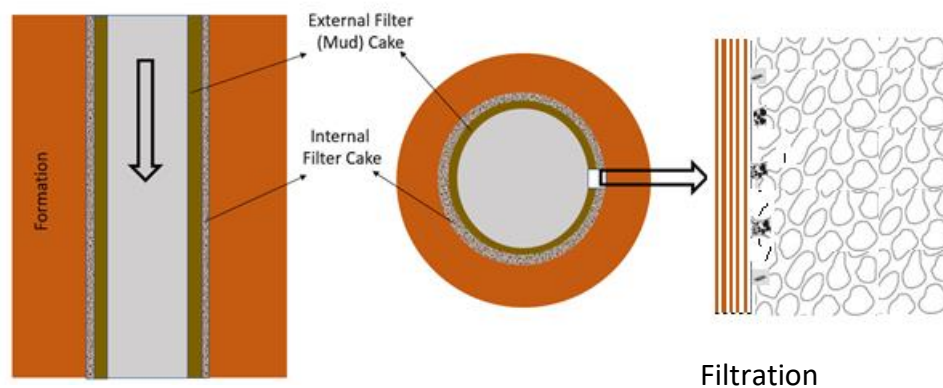
Figure 3-2: Wellbore from Side and Top View with Filter cakes and Filtration

During the drilling fluid selection, laboratory experiments of return permeability tests (RPT) are conducted to identify formation damages and effectiveness of fluid clean-ups from different formulations of drilling fluids (weighting particles and breakers) and with different mud cake lift-off or unloading conditions. Bailey et al. (1999) stated that during the initial stages of filter cake growth, particles are also forced into the formation, which

creates an internal filter cake that plugs the pores close to wellbore (Bailey et al., 1999). External and internal filter cakes can cause significant permeability reduction and result in high pressure drops. They investigated the solids invasion and their mobility during the clean-up process with water-based muds. Based on their study, fine particles invaded deep in the core and not easily removed by back flushing while larger particles have shallower invasion and bridge off near the surface. During their study, solids invasion profiles into sandstone cores for water-based drilling fluids were acquired employing scanning electron microscopy/ X-ray mapping (SEM-EDS) and synchrotron energy-dispersive X-ray diffraction tomography (EDD-T).

Zain et al. (2000) conducted experiments using 10 ppg water-based mud and flowback rates at 170 °F. Based on their analysis, external filter cake plays no role in determining flow initiation pressure (FIP) and return permeabilities. Rather it is solids and filtrate invasion that determine the flowback pressure profile during production (Zain, Suri, & Sharma, 2000).

Suri et al. (2010) explained the FIP as the drawdown required to initiate the flow when the well is put on production. They conducted experiments for two types of drilling fluids (sized calcium carbonate and bentonite) on sandstones and carbonates with a permeability range of 4 to 1500 md. Constant pressure flowback experiments were used to estimate the flow initiation pressures. According to their results, return permeabilities are controlled by the internal cake and not removal of the external cake.

In this dissertation, internal filter cake data of SB-DIF are provided by Shell Technology Center Houston (STCH) using their test cell and procedure of the Drill-in Fluid Production Return Perm Test (DIF-PRPT).

3.1.1 RPT Experimental Set-up

The experimental set-up used to conduct the Production Return Permeability Tests by Shell is shown in Figure 3-3. This is a High-Pressure High-Temperature set-up that allows experiments above 300 °F temperature and 1,000 psi overbalance pressure for long duration of lock-down times.

Figure 3-3: RPT Test Equipment

Figure 3-4 shows a schematic of the RPT system components separately and with the core or test plug. Above the test plug, the experimental RPT includes three sections: the ring spacer, annular gap spacer and a screen. All the components have fixed dimensions, whereby the injected fluid flows through these sections before reaching the outlet. The

ring spacer (0.13" thickness) is the component where the external filter cake builds and annular gap spacer (0.56" thickness) is where the mud cake settles.

During a regular experiment, production fluid is injected from bottom of the vessel through the test plug where pressure drop and flow rate values are measured to determine the initial permeability of the test plug. Following this step, the drill-in fluid is circulated at the top of the core to dynamically build the internal and external filter cakes with overbalance pressure (e.g., 300 psi) and for a given time period. At this point, in order to mimic the unexpected shut down conditions before the unloading of drill-in fluid, the experimental set-up can be locked down for several weeks at downhole conditions and the mud solids settle and form the mud cake. Finally, the production fluid is injected or produced again to measure the test plug return permeabilities.

The terminology used for the experiment and analysis is given below:

- Internal Filter Cake: The filter cake inside the core invaded with drilled solids and fluids filtrate.

- External Filter Cake: The filter cake built on top of the core

- Mud Cake: The section where DIF solids settles above the external filter cake.

- L_{core}=Length of test plug

- L_{int}=Thickness of internal cake

- L_{ec}=Thickness of external cake

- L_{mc}=Thickness of mud cake

- $L_{uninvadedcore}=L_{core}-L_{int}$

- $L_t=L_{core}+L_{ec}+L_{mc}$
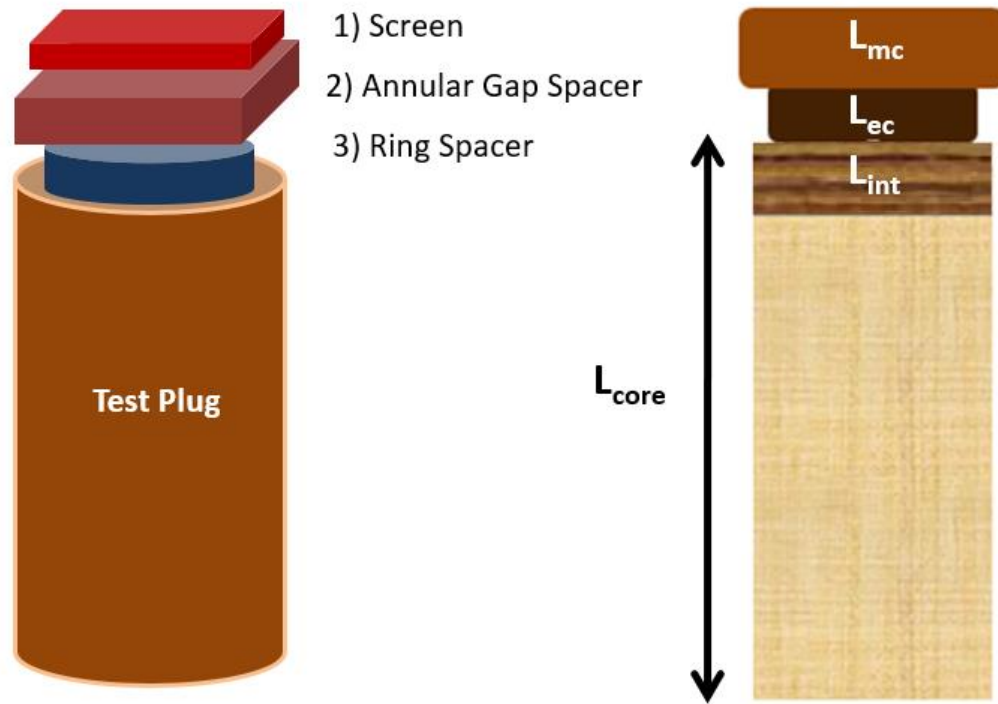
Figure 3-4: Schematic of RPT Equipment Components with Core

Figure 3-5 shows the side and top views of the external filter cake with core test plug taken after the experiment. There is no visible pinholes from the external filter cake of this SB-DIF.
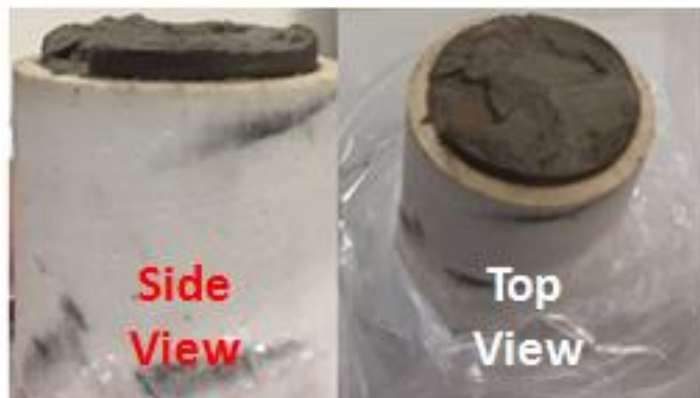
Figure 3-5: Picture of the External Filter Cake

3.1.2 Test Cores and Fluids

Four different RPT data were analyzed, including RPT 34, RPT 35, RPT 37 and RPT 38.
Table 3-1 summarizes the test plug dimensions (diameter by length), test lock-in
durations and production fluid.

Table 3-1: Test Core Properties

Test	Core Name	Dimension (inch)	Fluid	Test Lock in Duration (days)
1	RPT 34	1.48 by 3	Soltrol	15
2	RPT 35	1.49 by 3		60
3	RPT 37	1.50 by 3		14
4	RPT 39	1.50 by 3		6

3.2 CT-Scans and Pinhole Sizes

Following a Return Permeability Test, accurate measurement methods should be
applied to determine the size of the pinhole and depth of mud invasion into a core
sample. Computed-Tomography (CT) scan, which measures the density of the rock and
particles in the rock, is an applicable method. Van Overveldt et al. (2012) suggested CT-
Scans provides more detailed picture of the process than standard methods that are used
traditionally.

As mentioned earlier, in SB-DIF, pinholes are not visible to naked eye and cannot be
measured through direct measurements. The use of CT scans is most appropriate in this
situation. Following the Return Permeability Tests, tests plugs were CT-Scanned in the
Petroleum Engineering Department at the University of Houston. Scans are to provide
information on the thickness of the internal filter cake and an equivalent pinhole size at
the top of the core. The equivalent pinhole size is identified as the percentage of the

core's top surface area that has a relatively higher density or less invaded solids; thereby, more open for fluid flow.

In addition to the equivalent pinhole size and thickness of the internal filter cake, the permeability of the internal filter cake is also needed to develop the relation between pinhole pressure drop and PTA measurements (Chapter 4). Computational Fluid Dynamics (CFD) simulations are needed to calculate this permeability using the results obtained from RPT and CT Scans. The following section describes the steps used to conduct the global sensitivity analysis. This delivers a reduce order model to estimate the internal filter cake permeability without applying CFD simulations separately.

3.3 Global Sensitivity Analysis and Reduced Order Model for RPT measurements

CFD simulations are needed to estimate the internal filter cake permeability from the Return Permeability Test and CT Scan results. These simulations can be done using finite element method and existing commercial software packages, such as COMSOL Multiphysics®. To simplify and minimize the needs to perform simulations each time, a reduced order model using Sobol Analysis is used instead. Appendix B presents the mathematical background of the Sobol technique.

The goal of the global sensitivity analysis discussed in this section can be summarized as follows:

1. Identify and rank the dominant input parameters that have the most effects to the output parameter. In this case the input parameters are internal filter cake properties, pinhole size and flow rate. The output parameter is the pressure drop across the core plug. The main advantage of the Sobol method is its capability to capture not only the

effect of a single input parameter, but the interaction of input parameters on the variance of the output parameter.

2. Build a reduced order model that can be used to predict the inlet pressure of the core to calculate pressure drop across the core plug based on the dominant input variables identified by the global sensitivity analysis.

3.3.1 Sobol Technique

Unlike local sensitivity analysis, in the global sensitivity analysis the variation of the output parameter due to the variance in the input parameters can be evaluated (Sudret, 2008). This approach has the advantage of considering the effect of multiple input variables on the variation of the output variable. The Sobol method, which is a global sensitivity analysis, can be used for linear and nonlinear problems (Sobol, 2001; Sobol, 1993). This method is based on the measurement of the fractional contribution of the input parameters to the variance of the model output. The mathematical formulation of the technique is given in Appendix B.

Chapter 4

Wellbore Inflow and Well Surveillance

This chapter provides a brief background of wellbore skin and describes the calculation of wellbore inflow using the Pressure Transient Analysis. In the ramp-up methodology, following the measurement and calculation of filter cake and pinhole properties, the next step is developing the relationship between pinhole completion pressure drop and Pressure Transient Analysis skin.

Formation damage is considered as phenomena that reduce the potential of reservoir to produce fluids. It is generally caused by fluids used in drilling or completion operations. During drilling operation, the overbalance pressure between the DIF and formation can have mud particles invade the formation and cause permeability reduction in the near wellbore.

Van Everdingen & Hurst (1949) introduced the skin concept (s) to attribute for additional skin pressure drop (ΔP_s) in radial flow as

$$\Delta P_s = \frac{q\mu}{2\pi kL} s \ . \tag{4.1}$$

Hawkins (1956) worked on the skin concept as a concentric damaged region around the wellbore with damaged permeability (k_s) and radius (r_s) as

$$s = \left(\frac{k}{k_s} - 1\right) ln \frac{r_s}{r_w} \ . \tag{4.2}$$

This formation damage skin is one of the many skins, which contributes to the total skin or apparent skin. For radial flow, the total skin can be described as summation of

different skin components and Economides et al. (2013) gives the total skin factor equation as

$$s = \left(s_{comp}\right)_d + s_c + s_\theta + \Sigma s_{pseudo} \ . \tag{4.3}$$

(s_{comp})   : Combined effects of drilling, completion and permeability damage

s_c : Skin due to partial completion

s_θ : Deviated well skin effect

Σs_{pseudo}: Phase and rate dependent skin

Patel and Singh (2016) decomposed the last component, Σs_{pseudo} into two as; multiphase pseudo skin factor and non-darcy flow or rate-dependent high velocity or turbulent flow pseudo skin factor (s_{tur}) (Patel & Singh, 2016).

During the fluid flow from reservoir to wellbore, which is surrounded by internal filter cake and pinholes, different flow regimes will occur because of flow direction changes. In a wellbore with 100% open flow area, the only flow regime observed in a formation is radial flow. On the other hand, a wellbore with pinholes, the radial flow will transition to hemispherical flow due to convergence through the pinholes; thereby, introducing additional skin.

Furui et al. (2003) developed equations to predict skin factors for different completion types, such as: open hole, slotted liner, perforated liner, cased and perforated and gravel pack completions (Furui, Zhu, & Hill, 2003). Solutions accounts for the effects of formation damage, convergent flow to slotted or perforated liner. According to results, turbulence

effect skin factors for slotted or perforated liners would reach as high as tens of times larger than open hole alone where the rate-dependent skin factor may be negligible. Also, if formation sand plugs the slots or perforations, the turbulence skin can reach hundreds of times larger.

In this dissertation, Furui's solution of perforated liner is used for the calculation of the total pinhole area (or total number of pinholes flowing where each pinhole has a fixed diameter) as a function of the skin completion pressure drop. This approach replaces the perforations in the perforated liner as pinholes of the filter cake. Skin equation is given by Furui et al. (2003) as

$$s = s_{fo} + \frac{s_{L,r}^0}{k_{Ds}} + \beta_{Ds} f_{t,L} F_{o,w}, \qquad (4.4)$$

where $s^o_{L,r}$ is the rate-independent skin factor for perforated liner and s_{fo} is the conventional damage skin factor characterized by Hawkins' formula. k_{Ds}, $F_{o,w}$, $f_{t,L}$, β_{Ds} are dimensionless permeability ($k_{int}/k_{formation}$), Forcheimer number, turbulence scale factor and dimensionless scale factor, respectively. This equation considers the flow geometries for a well with perforated liner:

➢ Hemispherical flow region induced by perforation

➢ Radial flow region induced by perforation angular distribution

➢ Radial flow away from the perforations.

To calculate the total skin factor, completion skin pressure drop was estimated by taking the difference of the pressure drop between actual and ideal conditions. These

pressure drops were integrated along the actual (ξ) and ideal (ξ') flowpaths and they are given as follows:

$$\Delta P_{actual} = \int_{\xi_0}^{\xi_1} \frac{\partial p}{\partial \xi} d\xi = \int_{\xi_0}^{\xi_1} \left[\frac{q\mu}{kA(\xi)} + \beta\rho \left(\frac{q}{kA(\xi)} \right)^2 \right] d\xi, \tag{4.5}$$

$$\Delta P_{ideal} = \int_{\xi_0'}^{\xi_1'} \frac{\partial p}{\partial \xi'} d\xi' = \int_{\xi_0'}^{\xi_1'} \frac{qu}{kA(\xi')} d\xi', \tag{4.6}$$

and $\quad \Delta P_{skin} = \Delta P_{actual} - \Delta P_{ideal} = \frac{qu}{k} \left[\int_{\xi_0}^{\xi_1} \frac{d\xi}{A} - \int_{\xi_0'}^{\xi_1'} \frac{d\xi'}{A} \right] + \beta\rho q^2 \int_{\xi_0}^{\xi_1} \frac{d\xi}{A^2}. \quad$ (4.7)

Boundary of each flow region was calculated from the dimensionless parameters based on perforation number and distribution. Figure 4-1 shows a schematic of a liner with perforations where each perforation is considered as a pinhole. In these equations, the following parameters are used to calculate the rate independent part of the skin.

r_p=radius of perforations

l_s=perforation diameter:$2r_p$

r_{dp} =dimensionless radius: r_p/r_w

γ=Dimensionless parameter for axial convergence flow=r_{dp}/λ

λ=Perforation penetration ratio (perforation size per unit length): $2r_p/l_u$

m_p=Number of perforation units around the circumference of the liner

υ=Dimensionless parameter for perforation induced radial flow=$\sin(\pi/m_p)$
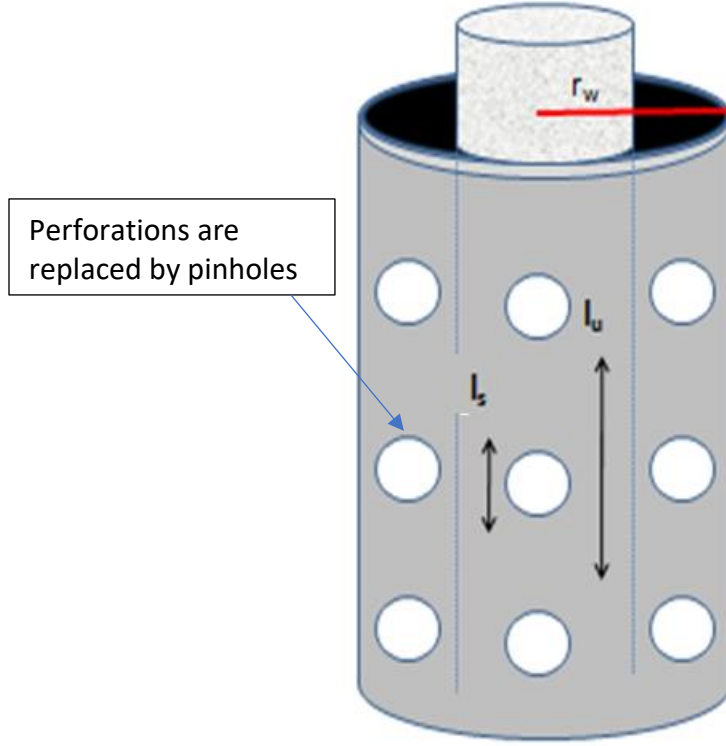
Figure 4-1: Schematic of Perforated Liner with Perforations Replaced by Pinholes

From the integrals, analytical skin equations for perforation liner are given by Furui et al.

(2003) as

For $\gamma < \upsilon$, high slot density;

$$s_{PL}^0 = \left(\frac{2}{m_p\lambda}\right)\left(\frac{3}{2} - \lambda\right) + \left(\frac{2}{m_p}\right)ln\left(\frac{\upsilon\lambda}{r_{Dp}}\right) - ln(1+\upsilon) \qquad (4.8)$$

and
$$f_{t,PL} = \left(\frac{2}{m_p\lambda}\right)^2\left(\frac{27}{8r_{DP}}\right) + \left(\frac{2}{m_p}\right)^2\left(\frac{1}{\upsilon}\right) + \frac{1}{1+\upsilon} \, . \qquad (4.9)$$

For $\gamma > \upsilon$;

$$s_{PL}^0 = \left(\frac{2}{m_p\lambda}\right)\left(\frac{3}{2} - \frac{r_{DP}}{\upsilon}\right) + \left(\frac{r_{Dp}/\lambda}{r_{Dp}+\lambda-1}\right)ln\left\{\left(\frac{\lambda+r_{Dp}}{1+\upsilon}\right)\left(1 + \frac{\upsilon(1-\lambda)}{r_{Dp}}\right)\right\} - ln\left(1 + \frac{r_{Dp}}{\lambda}\right) \qquad (4.10)$$

$$f_{t,PL} = \left(\frac{2}{m_p\lambda}\right)^2 \left(\frac{27}{8r_{Dp}} - \frac{r_{DP}^2}{v^3}\right) + \left(\frac{r_{Dp}/\lambda}{r_{Dp}+\lambda-1}\right)^2 \left\{\frac{1}{1+v} - \frac{1}{1+r_{Dp}/\lambda} + \frac{1-\lambda}{(1-\lambda)v+r_{Dp}} - \frac{\lambda(1-\lambda)}{r_{Dp}} - \right.$$

$$\left.\left[\frac{2(1-\lambda)}{r_{Dp}+\lambda-1}\right] ln\left[\left(\frac{\lambda+r_{Dp}}{1+v}\right)\left(1 + \frac{v(1-\lambda)}{r_{Dp}}\right)\right]\right\} + \left(\frac{r_{Dp}}{1+r_{Dp}/\lambda}\right). \qquad (4.11)$$

In our ramp-up methodology, using the completion skin obtained from the pressure transient analysis, the open flow area of pinholes in filter cake or perforations in perforated liner area will be calculated iteratively after re-arranging the above equations as follows:

For $\gamma < v$, high pinhole density;

$$s_P^0 = t_1 t_2 + t_3 - t_4, \qquad (4.12)$$

where;

$$t_1 = \frac{2r_p}{4r_w A_o}, \qquad (4.13)$$

$$t_2 = \frac{3}{2} - \frac{4r_w A_o}{m_p r_p}, \qquad (4.14)$$

$$t_3 = \frac{2}{m_p} ln\left(\frac{sin\left(\frac{\pi}{m_p}\right)4r_w^2 A_o}{m_p r_p^2}\right), \qquad (4.15)$$

$$t_4 = ln\left(1 + sin\left(\frac{\pi}{m_p}\right)\right), \qquad (4.16)$$

and $\qquad f_{t,P} = k_1 + k_2 - k_3, \qquad (4.17)$

where;

$$k_1 = \frac{27r_p}{32r_w A_o^2} \quad , \tag{4.18}$$

$$k_2 = \frac{4}{m_p^2 sin\left(\frac{\pi}{m_p}\right)} \quad , \tag{4.19}$$

and
$$k_3 = \frac{1}{1+sin\left(\frac{\pi}{m_p}\right)} \quad . \tag{4.20}$$

For $\gamma > \upsilon$,

$$s_P^0 = \left(\frac{2r_p}{4r_w A_o}\right)\left(\frac{3}{2} - \frac{r_p}{r_w sin\left(\frac{\pi}{m_p}\right)}\right) + \left(\frac{m_p r_p^2}{4r_w^2 A_o\left(\frac{r_p}{r_w}+\frac{4r_w A_o}{m_p r_p}-1\right)}\right) ln\left[\left(\frac{\frac{4r_w A_o}{m_p r_p}+\frac{r_p}{r_w}}{1+sin\left(\frac{\pi}{m_p}\right)}\right)\left(1 + \frac{sin\left(\frac{\pi}{m_p}\right)\left(1-\frac{4r_w A_o}{m_p r_p}\right)r_w}{r_p}\right)\right] - ln\left(1 + \frac{m_p r_p^2}{4r_w^2 A_o}\right) \tag{4.21}$$

$$f_{t,P} = \left(\frac{r_p^2}{4r_w^2 A_o^2}\right)\left(\frac{27r_w}{8r_p} - \frac{r_p^2}{r_w^2\left(sin\left(\frac{\pi}{m_p}\right)\right)^3}\right) + \left(\frac{r_p^2 m_p}{4r_w^2 A_o\left(\frac{r_p}{r_w}+\frac{4r_w A_o}{m_p r_p}-1\right)}\right)^2 \left\{\left(\frac{1}{1+sin\left(\frac{\pi}{m_p}\right)} + \frac{1}{1+\frac{r_p m_p r_p}{4r_w^2 A_o}} + \frac{1-\frac{4r_w A_o}{m_p r_p}}{\left(1-\frac{4r_w A_o}{m_p r_p}\right)sin\left(\frac{\pi}{m_p}\right)+\frac{r_p}{r_w}} - \frac{\frac{4r_w A_o}{m_p r_p}\left(1-\frac{4r_w A_o}{m_p r_p}\right)r_w}{r_p}\right) - \left(\frac{2\left(1-\frac{4r_w A_o}{m_p r_p}\right)}{\frac{r_p}{r_w}+\frac{4r_w A_o}{m_p r_p}-1}\right) ln\left[\left(\frac{\frac{4r_w A_o}{m_p r_p}+\frac{r_p}{r_w}}{1+sin\left(\frac{\pi}{m_p}\right)}\right)\left(1 + \frac{sin\left(\frac{\pi}{m_p}\right)\left(1-\frac{4r_w A_o}{m_p r_p}\right)r_w}{r_p}\right)\right]\right\} + \left(\frac{1}{1+\frac{r_p m_p r_p}{4r_w^2 A_o}}\right). \tag{4.22}$$

The Open Flow Area (OFA) is the total area of all flowing pinholes over the surface area of the open hole completion interval calculated from above equations. This OFA will be used in the ramp-up methodology to estimate the average pinhole flow velocity and calculate the pinhole completion pressure drop for each production rate increment. A

29

well with "100% OFA" will be labelled as the Hawkins' case, where Hawkins completion pressure drop is applied. On the other hand, a well with OFA less than 100 % is called as the pinhole case whereby additional pressure drop occurs due to converging flow introduced by pinholes. Figure 4-2 depicts the two scenarios with 100% OFA (Hawkins case) and less than 100% OFA (Pinhole case).
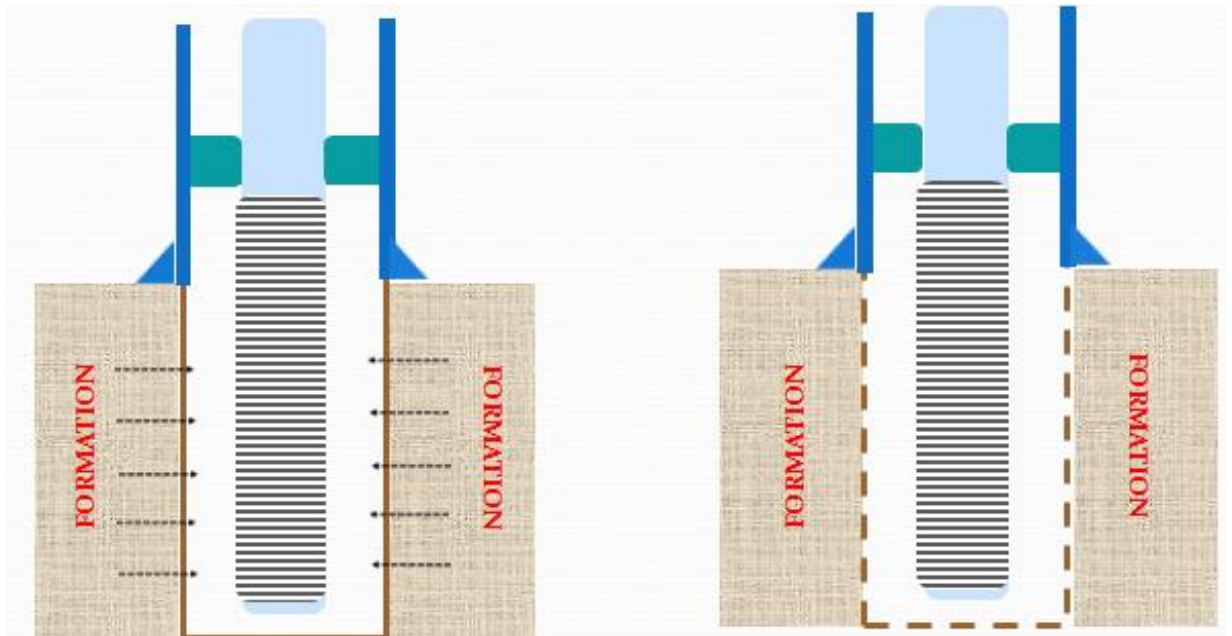
Figure 4-2: Schematic of Hawkins (A) and Pinhole (B) Cases

4.1 Limitations and Discussion

Production ramp-up is the operation after completion fluids have been unloaded. At this early stage, water production is not expected and assumed not to be present. As a result, permeability and skin interpreted from PTA analysis, and applications of the ramp-up methodology are based on single-phase fluid flow. Extension of this research to

multiphase flow or with water production has not been addressed. For such ramp-up and

surveillance applications, multiphase PTA interpretations would need to be considered.

Chapter 5

Flow Distribution of OH-SAS System by Network Modeling

Following calculation of the Open Flow Area (%) and velocities coming from pinholes, identifying the flow rate distribution in annulus and the velocity distributions in completion interval, such as the velocity distributions impinging on the screen (V_s) and converging to the top screen (V_a), is required. This helps make decisions during production ramp-up and improves design of the OH-SAS completion. The development of the flow distribution is achieved by modelling the OH-SAS system as a network shown in Figure 5-1. As a first step, the well is discretized into n sections, where the completion system with all its components are mapped onto a network system consisting of nodes and elements connecting all components. In the network system each section has the following components which creates resistance to the flow:

1) Annulus, fluid flow through the annulus

2) Sand Screen, fluid flow into the screen

3) Inside Screen, fluid flow through inside the screen or base pipe

The network system will be solved numerically by satisfying conservation of mass and mechanical energy balance equations.
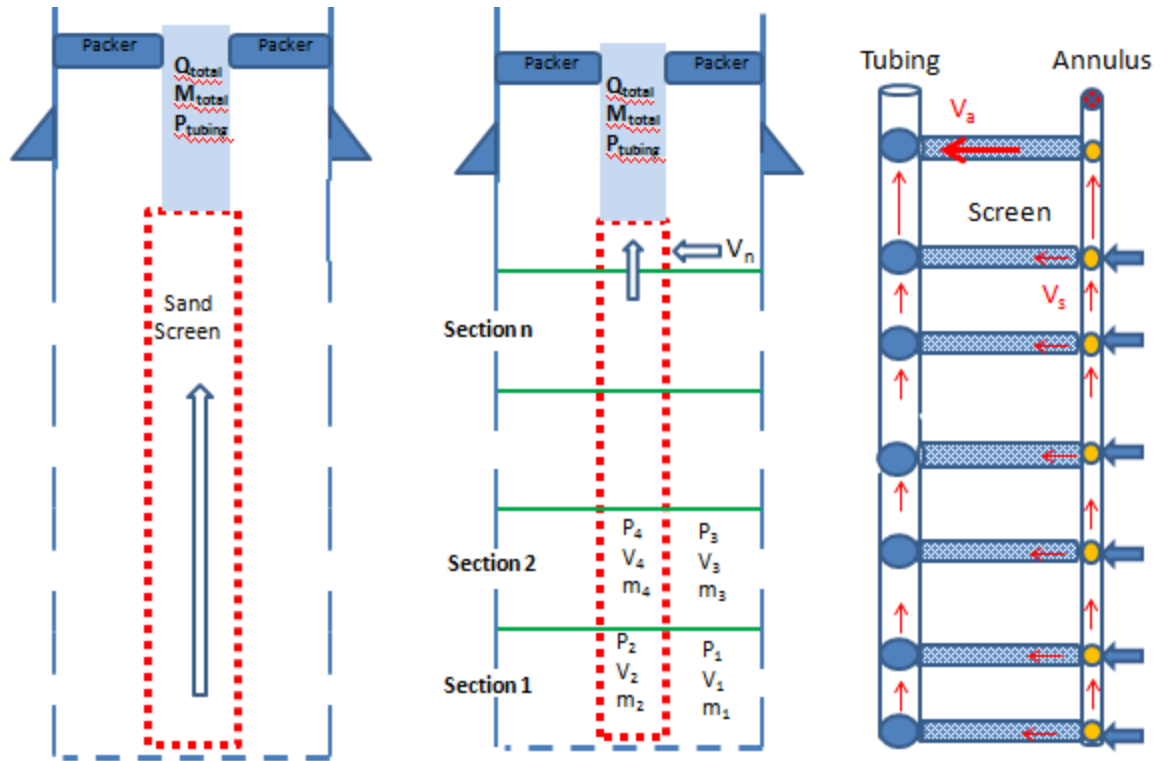
Figure 5-1: a) OH-SAS Well Schematic b) Discretized Completion c) Completion as Network System

In order to identify the flow distribution, an analogy was made with Kirchhoff's first and second law. Kirchhoff's Circuit laws are described by Gustav Kirchhoff in 1845. These laws include two equalities for current and potential in the lumped element model of electrical circuits. Kirchhoff's first law states that algebraic sum of currents in a network of conductors meeting at a point is zero. The second law defines that directed sum of the potential differences (voltages) around any closed loop is zero. Figure 5-2 depicts both Kirchhoff laws.

Cross (1936) studied analysis of networks employing different methods to solve the Kirchhoff's first and second laws. He employed Method of Balancing Flows and Method of Balancing Heads for Kirchhoff's first and second law, respectively. Li et al. (2003) presented methods to solve natural gas pipeline flow problems using electrical load flow

techniques (Li, An, & Gedra, 2003). He studied to integrate a natural gas network with an electrical power network for a combined distribution network. Raoni et al.(2017) proposed a method solving looped pipeline networks where Kirchhoff's laws are met in the system (Raoni, Secchi, & Biscaia, 2017). Their method used a modular procedure to determine the problem pressure difference equations and grouped them to be solved successively.

Pipeline network system analyses are inspired by Kirchhoff's laws by utilizing the following analogies for their solution:

First Law Analogy: The flow at any node is equal to sum of the flows that feeds the node

Second Law Analogy: The total pressure drop in a closed loop equals to zero.

The first and second analogy laws are equivalent to the mass (continuity) and energy conservation law. The following section presents the network equations that are solved, which provide the flow rate and pressure distributions in the OH-SAS completion system.
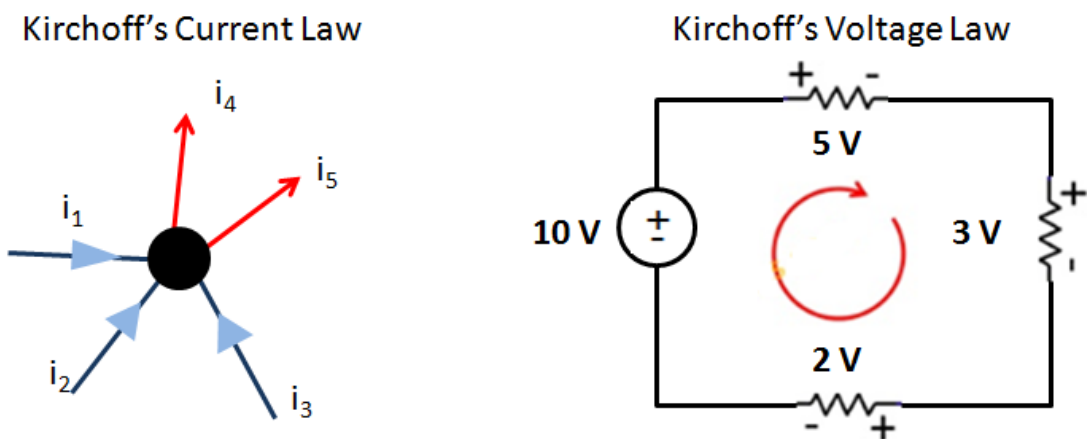

Figure 5-2: Kirchhoff's Current and Voltage Law

5.1 Energy Balance Equations

General mechanical energy balance and mass balance equations are solved simultaneously to determine the flow rates along the wellbore.

In an open system, the steady state energy balance can be written as (Morrison, 2013):

$$\Delta E_k + \Delta E_p + \Delta H = Q_{in,CV} + W_{s,by,CV} \quad , \tag{5.1}$$

where;

$$\Delta E_k = m\left(\frac{v_2^2}{2} - \frac{v_1^2}{2}\right), \tag{5.2}$$

$$\Delta E_p = mg(z_2 - z_1), \tag{5.3}$$

and
$$\Delta H = m\left(\hat{U}_2 - \hat{U}_1 + p_2/\rho_2 - p_1/\rho_1\right). \tag{5.4}$$

On the right-hand side, $Q_{in, CV}$ and $W_{s,by,CV}$ are the rate of heat into control volume and shaft work done by fluid in the control volume. For an incompressible fluid, its density is constant and substituting all the results above back into the open-system energy balance and dividing by m yields to Eq. 5.6

$$\left(\frac{v_2^2}{2} - \frac{v_1^2}{2}\right) + g(z_2 - z_1) + \left(\hat{U}_2 - \hat{U}_1\right) + (p_2/\rho_2 - p_1/\rho_1) = \frac{Q_{in,cv}}{m} + \frac{W_{s,by,CV}}{m}, \tag{5.5}$$

$$\frac{\Delta p}{\rho} + \frac{\Delta(v^2)}{2} + g\Delta z + \left[\Delta U - \frac{Q_{in,cv}}{m}\right] = -\frac{W_{s,by,CV}}{m}. \tag{5.6}$$

For the isothermal condition both terms in the square bracket are negligible. Grouping these terms together and calling them the friction term, F, Eq. 5.6 becomes

$$\frac{\Delta p}{\rho} + \frac{\Delta(v^2)}{2} + g\Delta z + F = -\frac{W_{s,by}}{m}. \tag{5.7}$$

In the left-hand side of Eq. 5.7, the four terms represent the change of pressure, kinetic energy, potential energy and the sum of friction, respectively. On the right hand of the equation is the additional or external work added.

Dividing by dL and ignoring the external work term;

$$\left.\frac{dp}{dL}\right)_{Total} = \left.\frac{dp}{dL}\right)_{elevational} + \left.\frac{dp}{dL}\right)_{accelerational} + \left.\frac{dp}{dL}\right)_{frictional}. \qquad (5.8)$$

The above equation is another way of writing the mechanical energy balance equation. The mass balance and mechanical energy balance equations are applied to each component of the network system and all the network equations are solved simultaneously to determine the velocity and pressure distributions in the system.

The resistance of fluid flow through a wire-wrapped screen is given in Appendix C using an equation that was obtained experimentally (Richard, Montagna, & Penberthy, 1997).

5.2 Hawkins and Pinhole Approach

The Hawkins approach represents the case where the wellbore's surface area across producing interval is open (100% flow area case). The reservoir interval is discretized into n sections and the total production rate is divided equally into n sections (i.e., rate/section) and distributed equally to nodes of each section as sources. The Pinhole approach represents the case with less than 100% flow area and with concentrated flows. Since both cases produce the same total flow rate, the pinhole case will have higher fluid velocity (V_c) coming out of the pinholes and entering the annulus region. To emulate this higher inlet velocity, the total number of nodal sources will be reduced proportionally to

the percentage of the pinhole open flow area; thereby, resulting in higher rate per source node. Figure 5-3(a) and Figure 5-3(b) depict the Hawkins and Pinhole Cases, respectively.

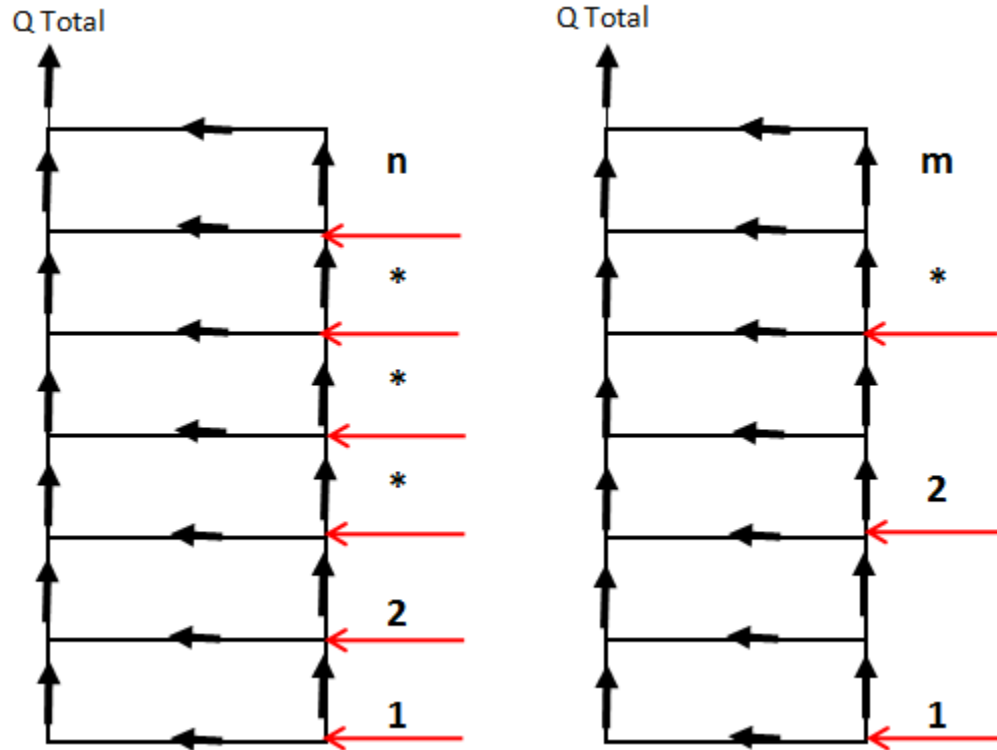Figure 5-3: a) Hawkins Case b) Pinhole Case

For n number of loops, there is a total of 3n+1 unknown flow rates which require 3n+1 non-linear equations to be solved numerically. As shown in Figure 5-4, the number of non-linear equations in the system equals to n loops plus 2n+1 mass bass balance equations.
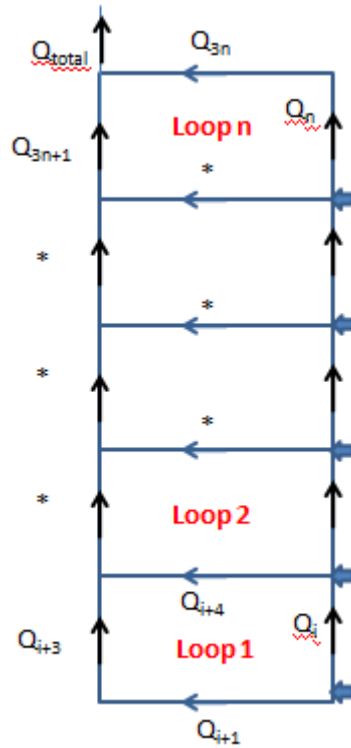
Figure 5-4: Loops and Flow Distribution

5.3 Limitations and Discussion

Modelling the wellbore as a network system composed of loops requires fluid flow at each branch. For a completion configuration with the screen's top inside or below the reservoir's top, there will be a loop containing reservoir inflow, annular flow and a screen without flow (or blank pipe section). This screen section without flow is not allowed in the network system solution. The network flow approach used in this research can only consider completion configurations with screen's top above the reservoir interval.

38

Chapter 6

Results and Discussions

This chapter presents the results and discusses the ramp-up methodology

components. Results will be provided for each component as follows

- ➢ Pinhole Size and Filter Cake Properties

  - ○ Return Permeability Test (RPT)

  - ○ CT Scan

  - ○ Global Sensitivity Analysis and Reduced Order Model

- ➢ Wellbore Inflow and Well Surveillance

- ➢ Flow Distribution of OH-SAS System by Network Modeling

6.1 RPT Experimental Results and Analysis

RPT test results for four different combination of DIF and test plug were provided by

Shell. The initial test plug permeability (without filter cake), k_{core}, and the final test plug

permeability (with the varying DIF filter cake and back flow clean-up), k_f, were analyzed.

Both k_{core} and k_f are obtained by analyzing the pressure drop across the length of the test

plug vs. flow rate. The ratio of final to initial permeability is the reported return

permeability result in percentage that characterizes the effectiveness of DIF used or its

damage potential after the filter cake clean-up. Both initial and final permeability are

measured using the producing fluids Soltrol. Table 6-1 shows these test results with

sample RPT 37 having the highest return permeability value.

Table 6-1: Measured Core Permeabilities

Test	Initial Permeability (k_{core}) Before Cake Build-up (mD)	Final Permeability (k_f) After Cake Build-up (mD)	k_f/k_{core} (%)
RPT 34	632	348	55.1
RPT 35	640	176	27.3
RPT 37	589	509	86.3
RPT 38	676	458	67.7

6.2 CT Scans Results and Analysis

Return permeabilities include combined effects of all three cake layers (mud cake, external filter cake and internal filter cake) from the DIF as shown previously in Figure 3-4. The ramp-up model assumes the external cake and the mud cake are produced through the sand screen during the completion fluid unloading process. The completion pressure drop in the pinhole model requires inputs of internal filter cake permeability (k_{int}), internal filter cake thickness (L_{int}), and an equivalent pinhole flow area or Unit Flow Area (UFA). Both the thickness and the equivalent pinhole area are determined from the CT scans.

Figure 6-1 shows the CT scans side view of samples RPT-34 and RPT-37. The scans show L_{int} of 0.02" and 0.004", for RPT 34 and RPT 37, respectively. The CT scans of the core samples from the top view are presented in Figure 6-2. In the figure, the bright regions indicate areas of higher density caused by invaded filtrate liquid and mud solids that were not effectively cleaned-up or with damaged permeability. The darker regions are areas of lower density with less invaded solids that were more effectively cleaned-up or with less damaged permeability. In this dissertation, the undamaged area or darker region will be approximated as the pinhole flow area or unit flow area (UFA). RPT 37 has a few small

bright spots representing a very uniform filter cake clean-up or a large pinhole flow area.

RPT 34 has a larger and non-uniformly distributed brighter region representing a smaller

pinhole flow area. Table 6-1 supports these observations with RPT 37 having a higher

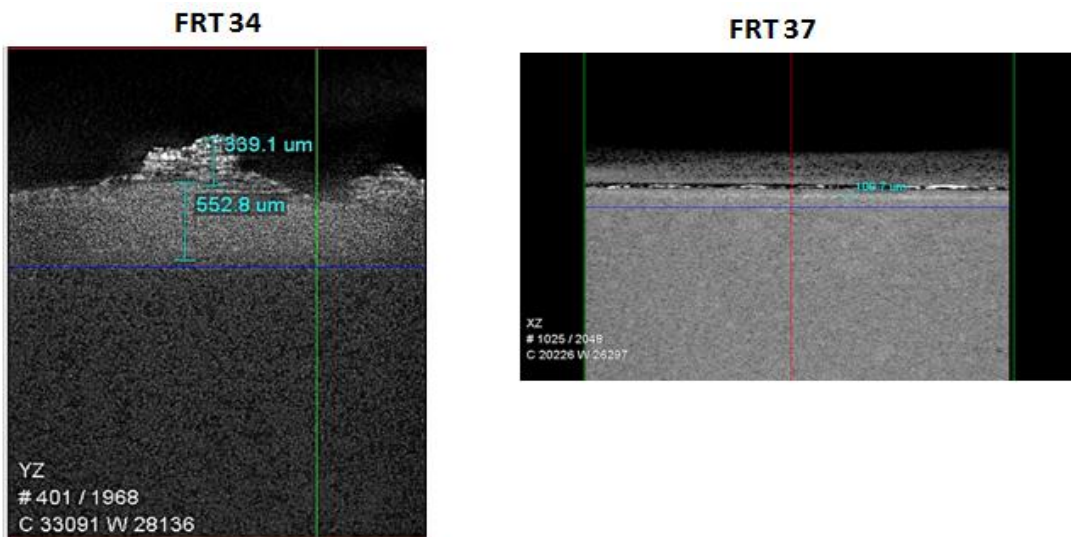return permeability ratio than RPT 34.
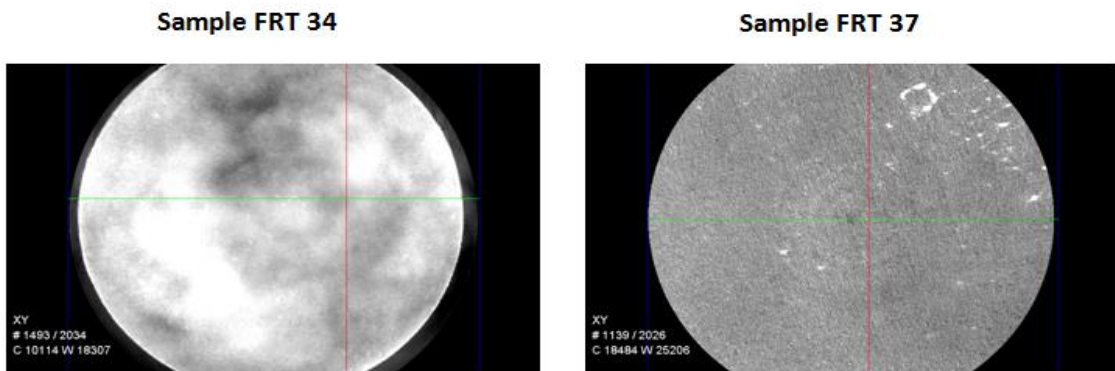

Figure 6-1: CT Scans Side View

Figure 6-2: CT Scans Top View

The pressure drop across the test sample is taken over the entire cross section area of the test plug and including the presences of mud cake, external filter cake, and internal filter cake as depicted in Figure 3-4. Using Darcy's law and a flow in series across these three layers, Eq. 6.1 can be written as

$$\frac{L_t}{k_{total}} = \frac{L_{uninvaded\_core}}{k_{core}} + \frac{L_{int}}{k_{int}} + \frac{L_{ec}}{k_{ec}} + \frac{L_{mc}}{k_{mc}}.$$ (6-1)

Where k_{int}, k_{ec} and k_{mc} are the permeabilities of internal filter cake, external filter cake and mud cake, respectively. Figure 3-4 defines the other variables in Eq. 6-1. As the values of each layer's permeability is not known separately, the following approach is applied for two scenarios. In the first approach, k_{mc} (mud cake permeability) is assumed to be infinite (i.e., no mud cake), which results in a minimum value for k_{int}+ k_{ec}. In the second approach, both k_{ec} and k_{mc} are assumed to be infinite (i.e., both mud cake and external filter cake are not present), resulting in a minimum value for k_{int}. Table 6-2 provides the results for RPT-34, which has an internal filter cake length or L_{int}=0.02 inch (552.8 µm) from the CT-Scan (Figure 6-1).

Table 6-2: Minimum Permeabilities, RPT 34

RPT 34	Minimum k_{int} +k_{ec} (mD)	k_{mc} (mD)	
Internal+External Cake	34	∞	
	k_{int}	k_{ec}	k_{mc}
Only Internal Cake	7	∞	∞

6.2.1 Pinhole Size and Filter Cake Permeability Calculation with CFD

The permeability of internal filter cake (k_{int}) in Table 6-2 is determined using the entire cross section area of the test plug, i.e., the pinhole diameter equals to the core plug diameter or 100% UFA. However, the measured pressure drop from the RFT is affected by the combined effects of L_{int}, k_{int}, and UFA as a system. This means computational fluid dynamics (CFD) simulations are needed to investigate the effect of different pinhole diameters (UFAs) on k_{int} for a given set of L_{int}, undamaged core permeability (k_{core}), produced fluid properties (Soltrol density and viscosity) and RPT pressure drop and flow rate. COMSOL Multiphysics® is used for these simulations with a circular pinhole in the middle of the test core. Simulations used an axisymmetric 2D model representing the test plug with the internal filter cake and pinhole.Figure 6-3 illustrates the axisymmetric model and its main inputs for the CFD simulations.
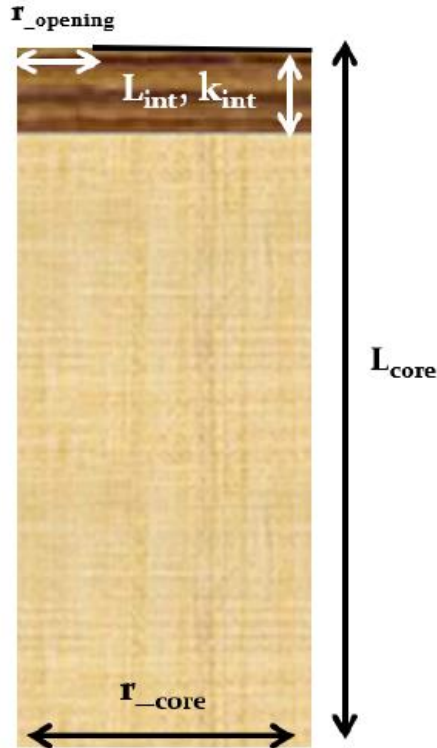
Figure 6-3: CFD Axisymmetric model and Main Inputs

Table 6-3 gives the calculated k_{int} as a function of different values of concentric circular pinhole flow area or UFA of 100%, 75%, 50%, and 25% of the test plug cross section area. These simulation results are based on a constant L_{int} of 0.02 inch and RFT pressure drop of 0.8 psi and flow rate of RPT 34. It is important to emphasize that k_{int} increases as the pinhole flow area reduces when all other parameters are held constant. As expected, for the case with UFA of 100% the k_{int} of 6.8 mD is close to the calculated k_{int} of 7 md shown in Table 6-2.

Table 6-3: Internal Filter Cake Perm vs. Different Pinhole UFA for RPT 34

UFA (%)	k_{int} (mD)	Δp (psi)
100	6.8	0.8
75	9	0.8
50	14	0.8
25	31.5	0.8

A CFD output screenshot from these simulations is presented in Figure 6-4. It shows, the pressure profile along the length of the core sample for a case with UFA less than 100%.
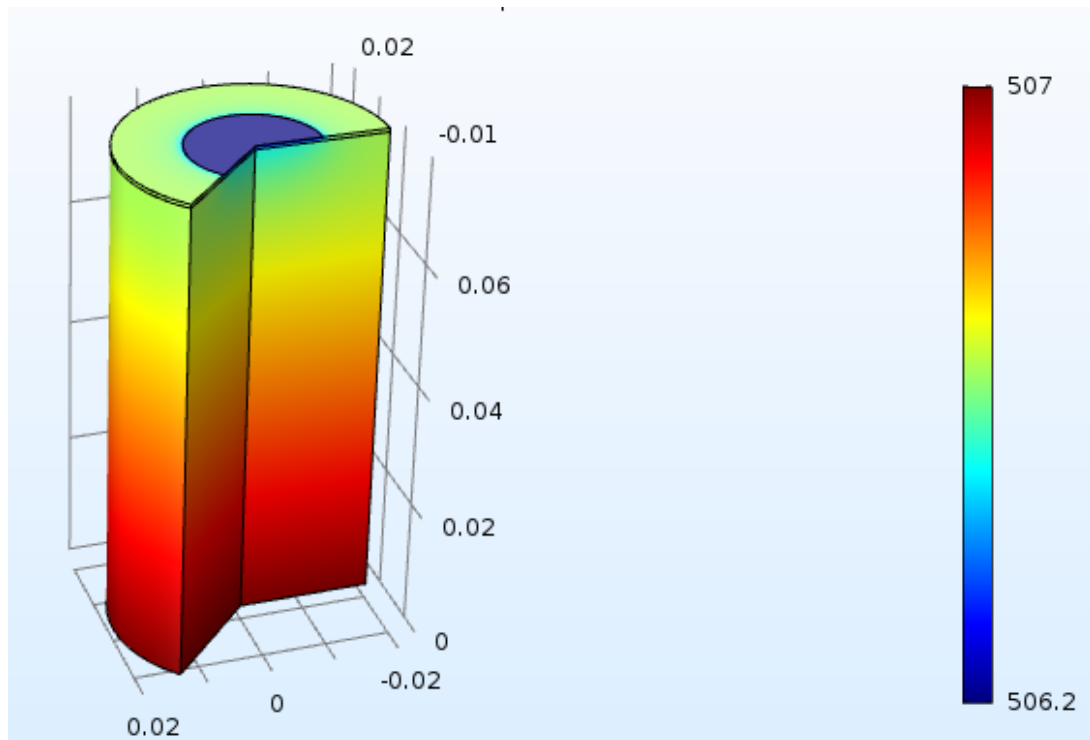

Figure 6-4: CFD Simulation Screenshot

Figure 6-5 shows the pressure profiles, streamlines and flow velocity vectors in the axisymmetric cross section of the test plug that includes the pinhole outlet with internal

filter cake permeability and thickness. As expected, the pressure drop increases

significantly as the fluid flow approaches the pinhole outlet because of the smaller outlet

area. Similarly, the streamlines and flow velocity vectors converge and increase in the

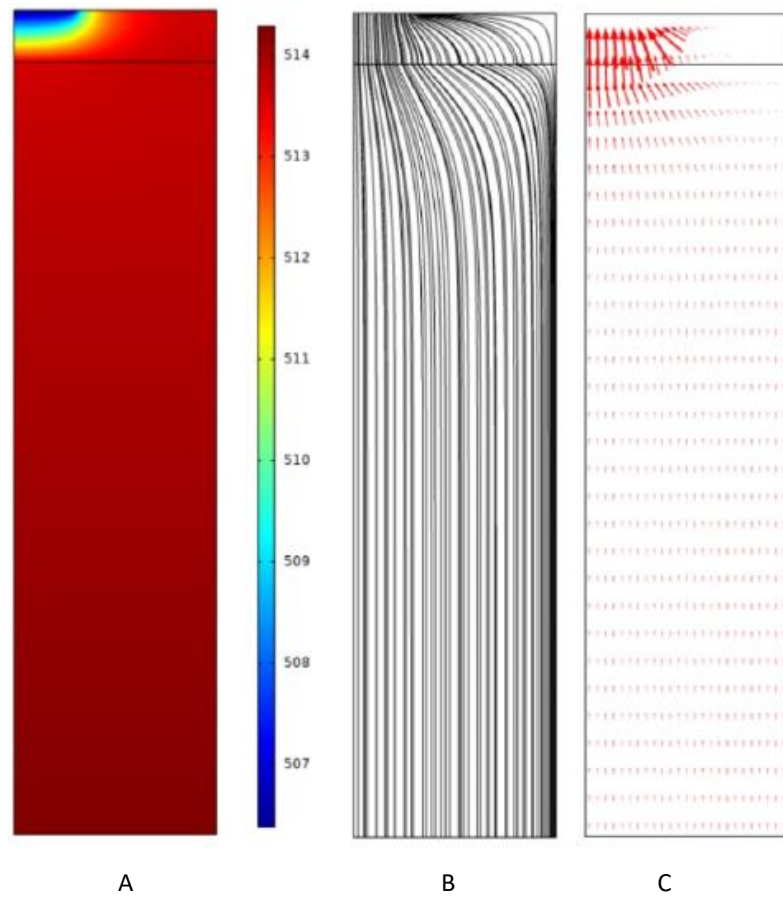pinhole outlet. They are accentuated by the effects of internal filter cake properties and

thickness.

Figure 6-5: CFD Simulations 2D Slice

6.3 Global Sensitivity Analysis and Reduced Order Model for RPT Measurements

As explained in previous section, CFD simulations are required to estimate the internal filter cake permeability using RPT and CT scan results. Instead of making CFD simulations each time with different RFT and CT scan results, the global sensitivity analysis with developed reduced order model is performed. This approach would enable the estimation of k_{int} with known RFT and CT-scan data.

6.3.1 A Reduced Order Model for RPT

Four independent input variables are selected for the global sensitivity analysis, which have critical effect on the pressure drop of the RPT. These variables are radius of pinhole (note, this can be determined using UFA) at the top of the core, $r_{opening}$, injection velocity, v_i, internal filter cake permeability, k_{int} , and internal filter cake thickness, L_{int}. CFD simulations are necessary to analyze the interaction and combined effects from these variables. Here, the CFD simulations are conducted to develop the function f in Equation B.1 in Appendix B. As the function is not known, Monte-Carlo simulations must be conducted in order to carry out the integration numerically. Table 6-4 shows the chosen variables and their ranges, which are selected for the global sensitivity analysis. The parameters are divided into core radius, length, permeability and maximum velocity, respectively to make them dimensionless and select ranges expected of a typical RPT. Also shown in the table, the associated Sobol index for each parameter are given as S_i.

Table 6-4: Dimensionless Parameters

	$r_{opening}$	L_{int}	k_{int}	V
	(-)	(-)	(-)	(-)
Minimum	0.22	0.001	0.003	0.01
Maximum	0.97	0.1	0.06	1
Sobol Index	S1	S2	S3	S4

A total of 8,000 CFD simulations were conducted using CFD software (COMSOL Multiphysics®) and including combination of input variables needed for Sobol Analysis. Figure 6-6 and Figure 6-7 show the individual and interaction contributions of the input variables, respectively. As can be seen in Figure 6-6, among the single term Sobol indices, the internal cake permeability (S_3) has the biggest effect (~0.32) on the total pressure drop. This means 32% of the inlet pressures changes is contributed by the internal cake permeability alone. The second and third most dominant variables are the pinhole radius (S_1) and the injection velocity (S_4), with 15% and 13% effects, respectively.
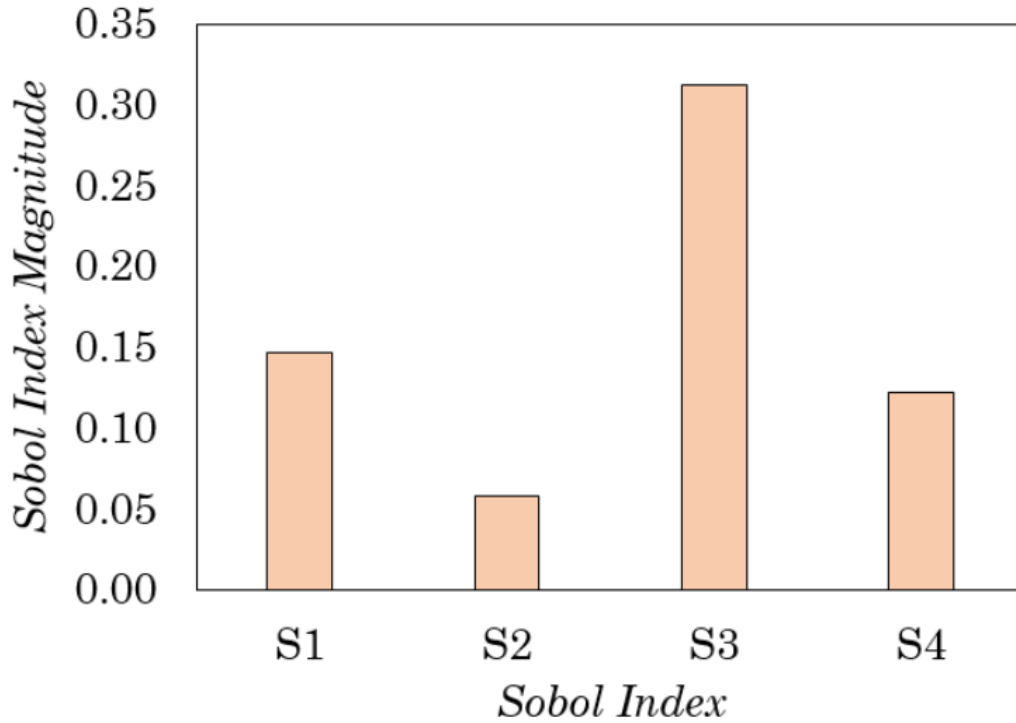
Figure 6-6: Sobol Indices Individual Effects

As it was mentioned before, the advantage of the Sobol technique is its capability to capture the interaction effects among the input variables. Figure 6-7 shows the Sobol indices of the second order interactions of the input variables. Among the higher order terms, S_{13} is the Sobol index of the variance in inlet pressure from changing both variables S_1 and S_3 together. Figure 6-7 shows S_{13} has the most dominant effect as compared to other second order indices. Note that the next higher order Sobol terms, such as S_{123} are neglected, since the sum of all indices up to the second order already contributed to 96 % of the total changes. If more precise results are desired, one can include the higher order terms with the same methodology described earlier.
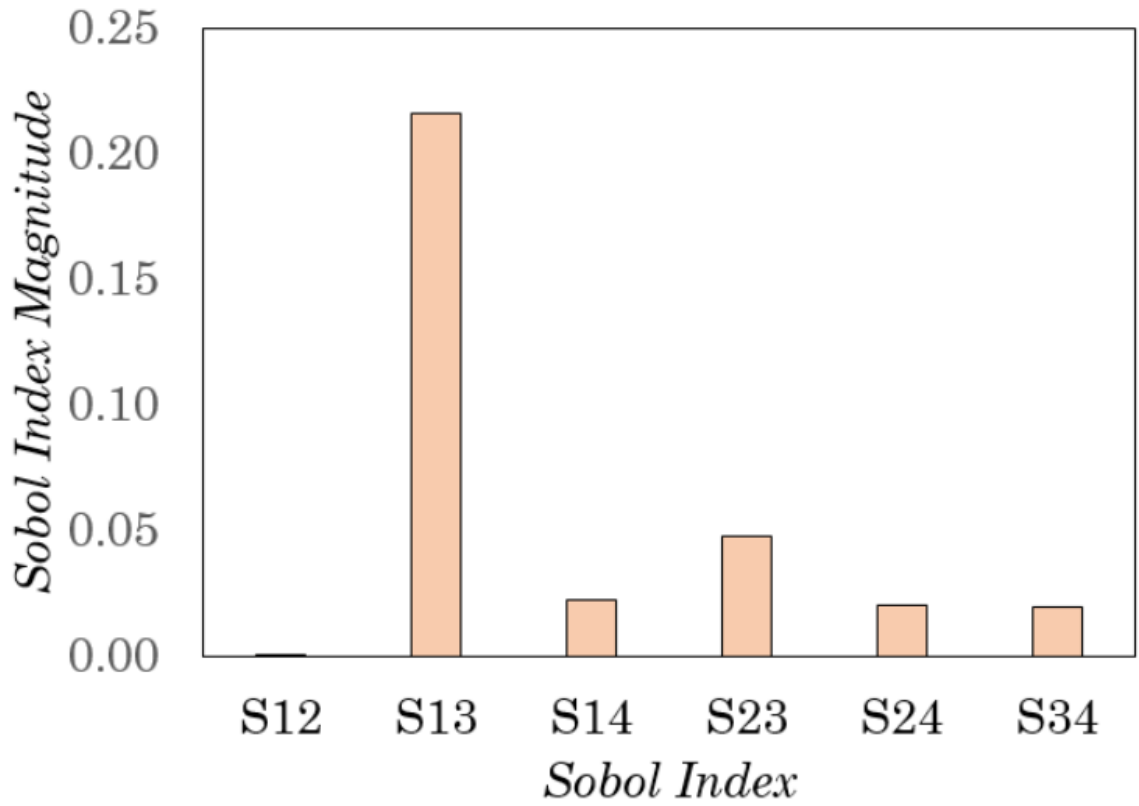
Figure 6-7: Interaction Effects

Below is the summation of all the Sobol first order and second order indices which

are equals to 0.96, as given by

$$S_1 + S_2 + S_3 + S_4 + S_{12} + S_{13} + S_{14} + S_{23} + S_{24} + S_{34} = 0.96.$$

Since, some of the indices have small effect, the indices selected to develop the

reduced order model are given by

$$S_1 + S_2 + S_3 + S_4 + S_{13} + S_{23} + S_{34} = 0.92.$$

Figure 6-8 to Figure 6-14 show the variation of the Sobol functions with respect to the

corresponding input variables. First four graphs present the individual function of each

parameter. As can be seen in Figure 6-8, pressure at the core inlet decreases as the

dimensionless radius at the top of the core increases due to a larger outlet. Figure 6-9

shows that an increase in the internal filter cake thickness increases the inlet pressure.

The individual effect of the internal cake permeability is shown in Figure 6-10, where the

inlet pressure decreases with increasing permeability. The last individual effect is the inlet

velocity that is shown in Figure 6-11, which can be linearly correlated with the pressure.

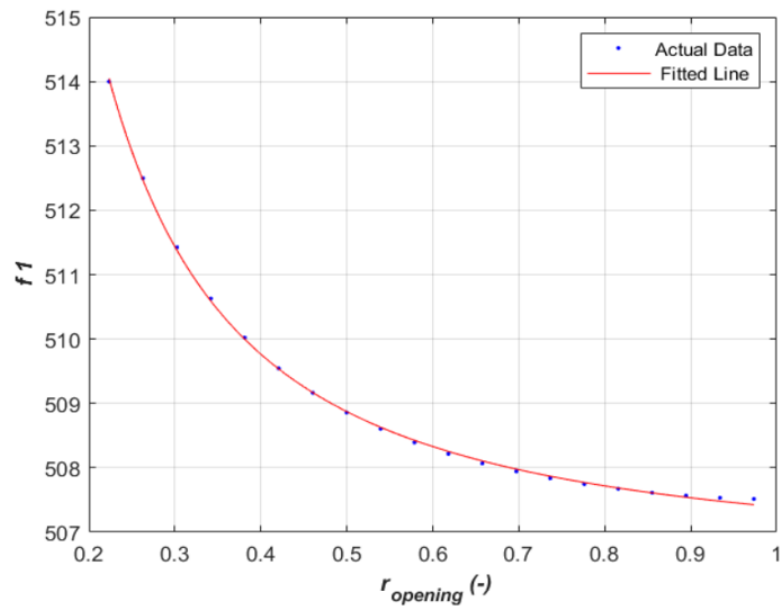Each one of these functions contains the least square regression equation.

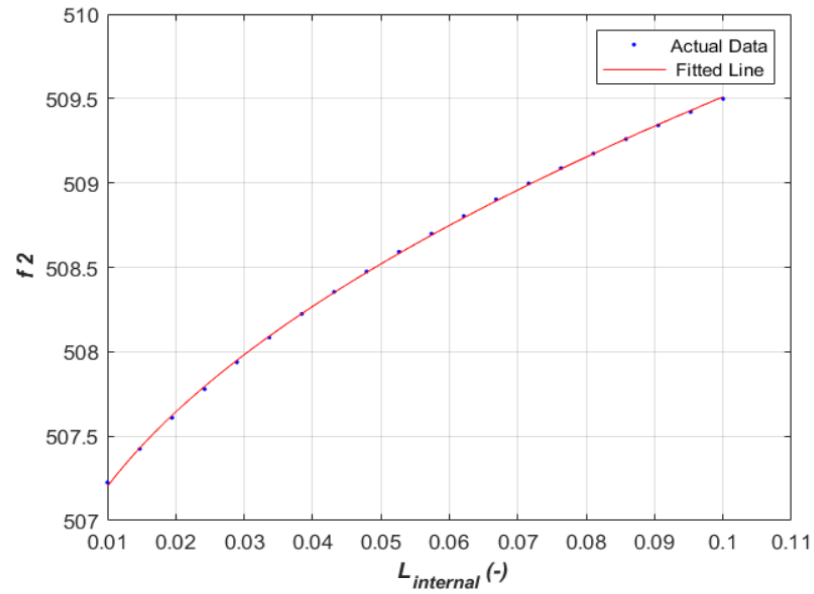Figure 6-8: $r_{opening}$ vs $f1$

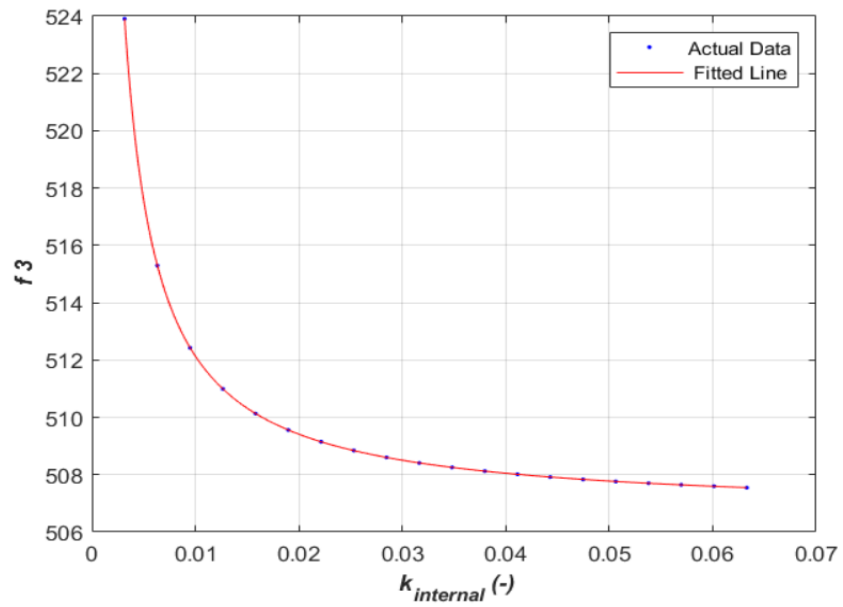Figure 6-9: L_{int} vs $f2$

Figure 6-10: k_{int} vs $f3$

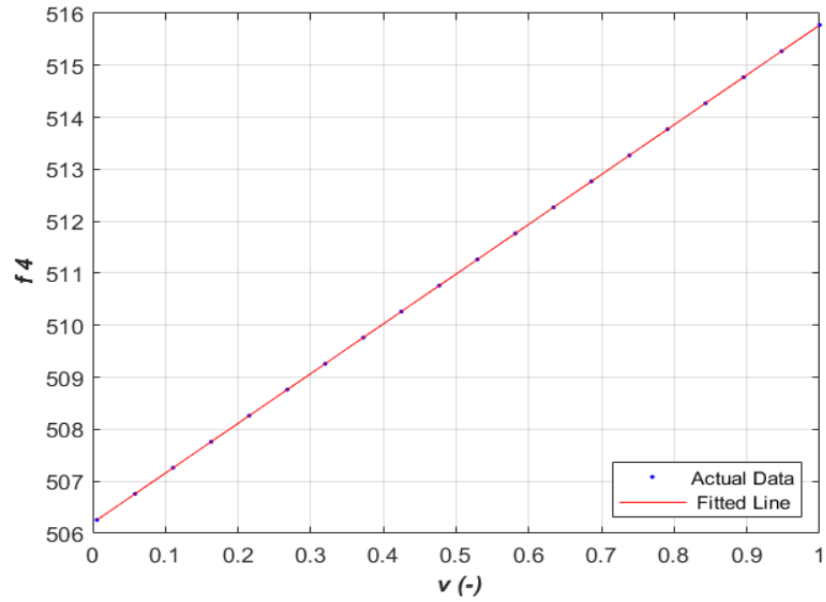Figure 6-11: v vs *f4*

The changes of f_{13}, f_{23}, and f_{34} with respect to their variables are presented in Figure 6-12 through Figure 6-14. The dots on the plot give the model output while the surfaces represent the least square regression.
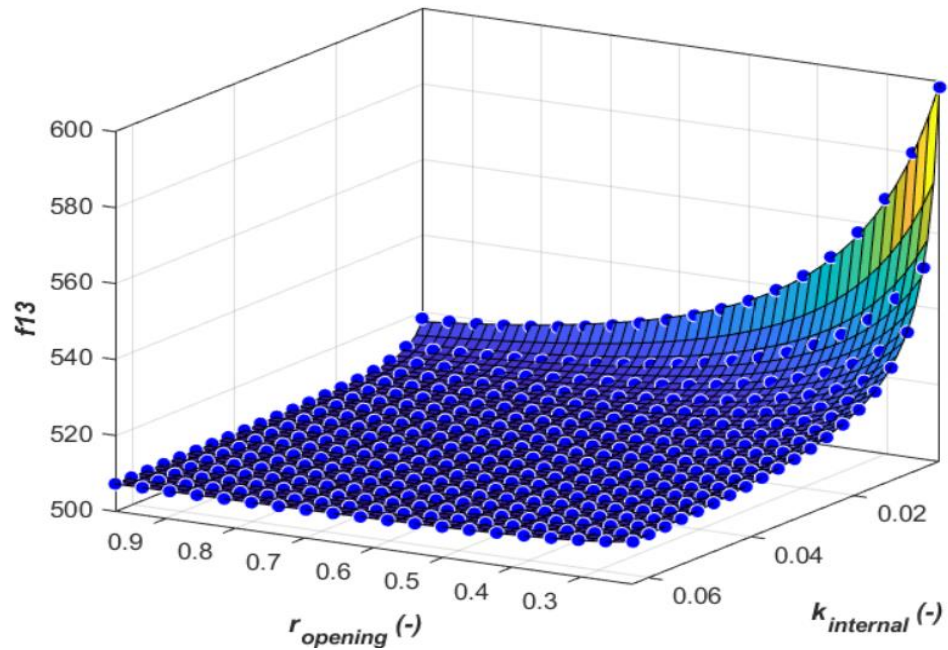

Figure 6-12: $r_{opening}$ & k_{int} vs *f13*
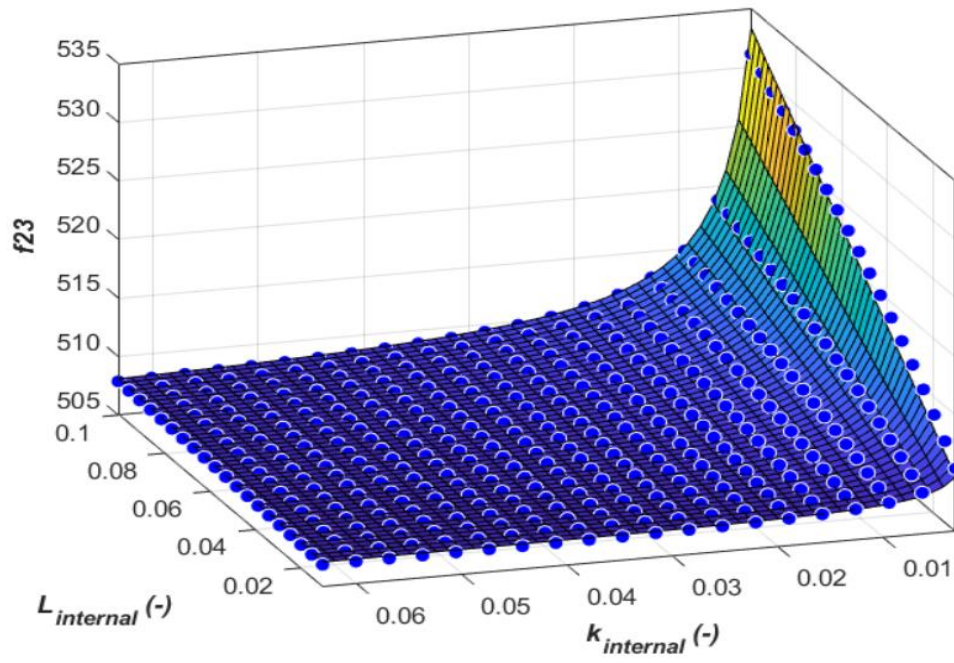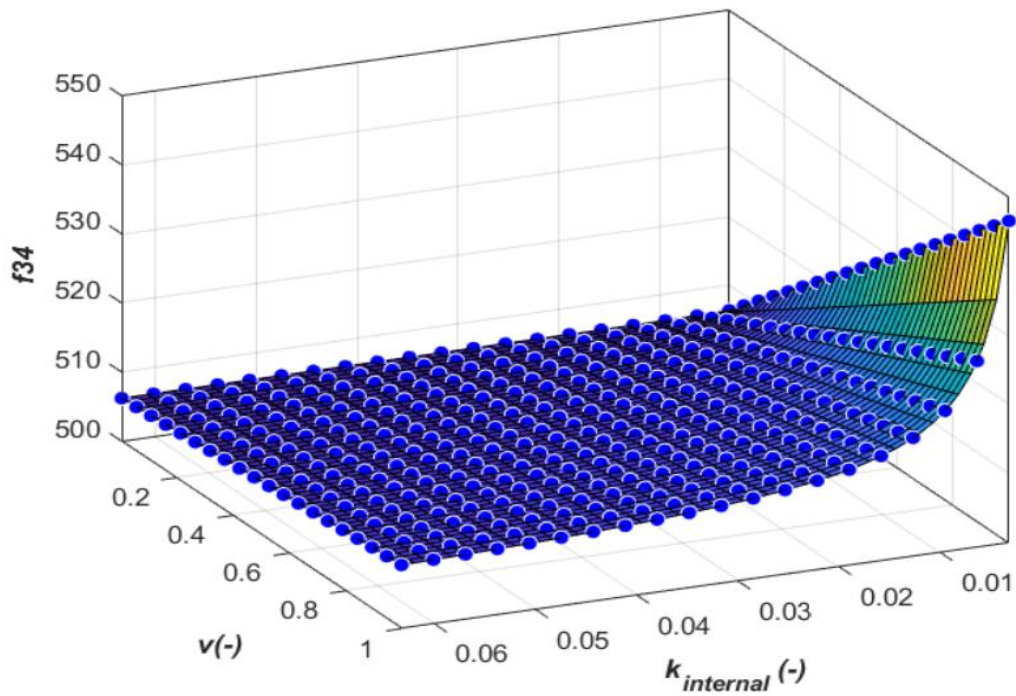
Figure 6-13: L$_{int}$ & k$_{int}$ vs *f23*

Figure 6-14: v & k$_{internal}$ vs *f34*

The equations are extracted from the above figures are written based on technique to

generate the functions for the calculation of the inlet pressures, as follow:

$$f_0 = 510.2, \tag{6.2}$$

$$f_1' = 0.85 r_{opening}^{-1.45} + 506.5 - f_0 \ , \tag{6.3}$$

$$f_2' = 10.7 L_{int}^{0.5} + 506.1 - f_0 , \tag{6.4}$$

$$f_3' = 0.05 k_{int}^{-0.99} + 506.7 - f_0 , \tag{6.5}$$

$$f_4' = 9.57 v + 506.2 - f_0 , \tag{6.6}$$

$$f_{13}' = (r_{opening})(k_{int}) + 0.033(r_{slot}^{-1.4})(k_{int}^{-0.99}) + 506.6 - f_0 - f'_1 - f_3' \ , \tag{6.7}$$

$$f_{23}' = (L_{int})(k_{int}) + 0.54 L_{int}(k_{int}^{-1.07}) + 507 - f_0 - f_2' - f_3', \tag{6.8}$$

$$f_{34}' = 0.121(k_{int}^{-1})(v) + (k_{int}^{-0.02})(v) + 506.2 - f_0 - f_3' - f_4', \tag{6.9}$$

and the proposed reduced order model can be presented as

$$Inlet\ Pressure = f_0 + f_1' + f_2' + f_3' + f_4' + f_{13}' + f_{23}' + f_{34}' .$$

6.3.2 Error Analysis

Error analysis is conducted in order to quantify the accuracy of the developed reduced

order model. The analysis is carried out by comparing the predictions of the model with

the CFD simulations. Figure 6-15 shows the error in percentage for all 8,000 simulations.

As can be seen from the figure, maximum error is around 8% which is less than the sum

of the Sobol indices, namely, 0.92. Figure 6-16 compares the model prediction against the simulation results. In order to test the performance of the proposed reduced order model, a new data set is used. This set is selected from the parameter values that are not used while developing the reduced order model.

Additional 260 simulations are conducted using the new data set, which is not used initially for the development of the reduced order model. The CFD simulation results are compared with the reduced order model predictions in Figure 6-17 and Figure 6-18. As can be seen, the maximum percentage error for all simulations conducted is again less than 8%. This demonstrates that the proposed reduced order model can replace the CFD simulations with confidence. If smaller errors are desired, more Sobol terms must be added to the reduced order model.
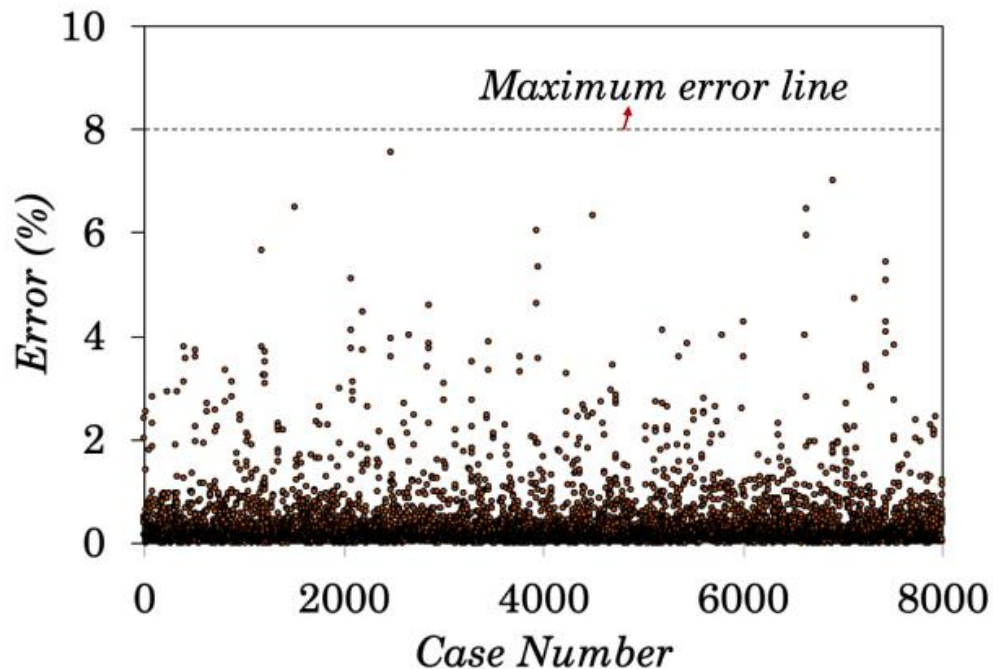

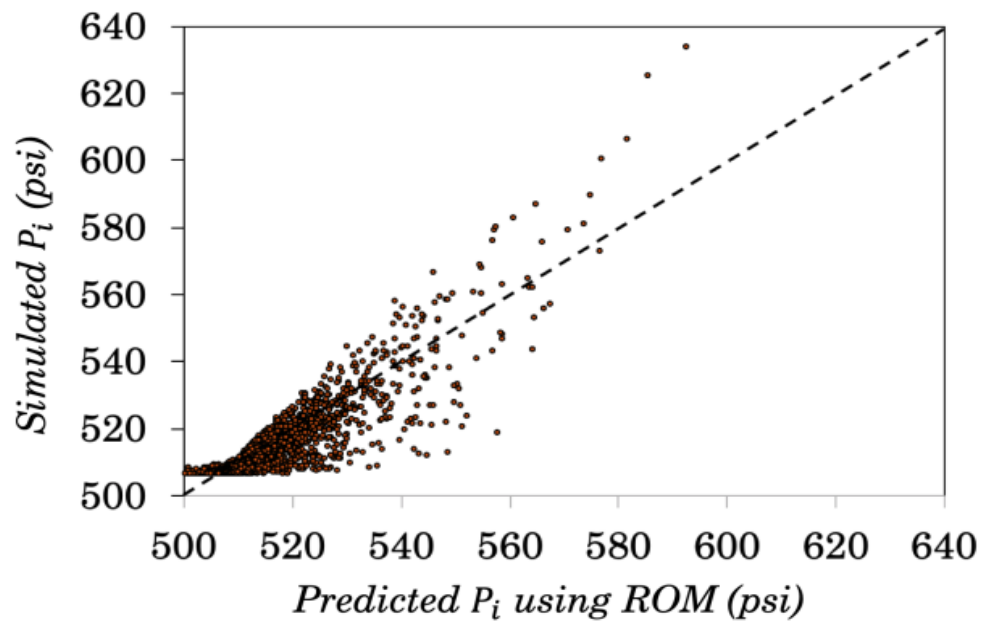Figure 6-15: Error Analysis, Error vs. Case Number

Figure 6-16: Simulation Results vs. Model Prediction
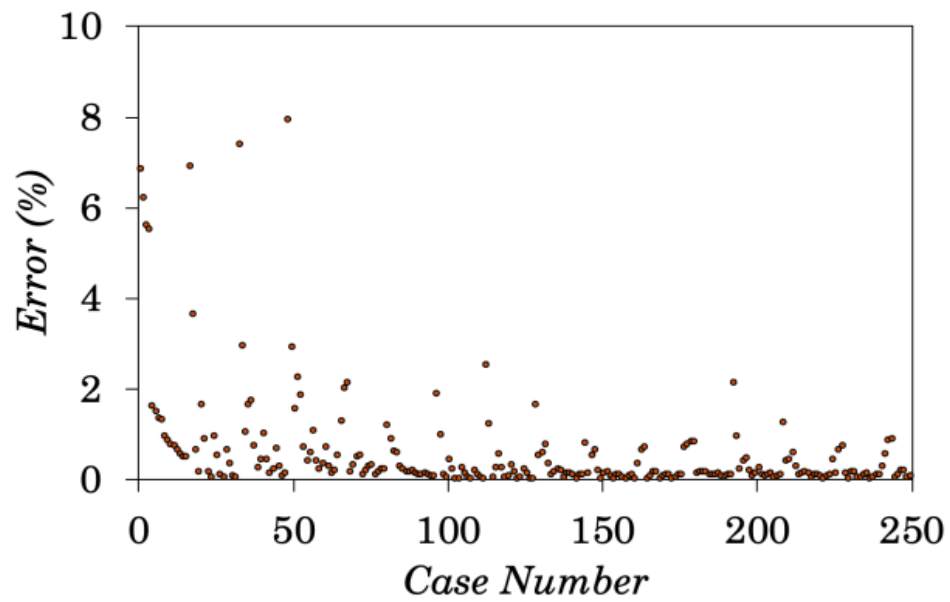
Figure 6-17: Error Analysis, Testing
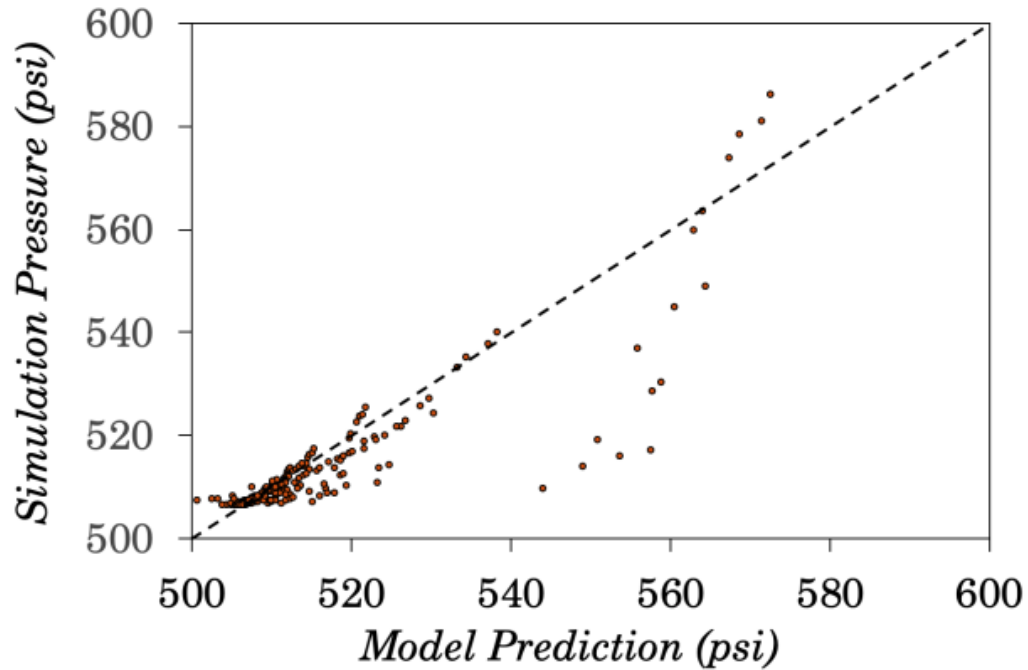
Figure 6-18: Simulation Results vs. Inlet Pressure, Testing

6.4 Ramp-up Methodology Wellbore Inflow and Well Surveillance

This section describes the proposed strategy to ramp-up production to the peak rate. The approach is to take several increasing flow rates and taking PTA after each rate to assess well performance and screen erosion risk before proceeding to the next higher rate. For example, taking 3 steps to reach the desired peak rate with each step increasing by 1/3 of the peak rate. After each production rate is stabilized, a PTA is taken to assess the well performance before continuing to the next higher rate. The completion performance is evaluated using the relationship of DPcom and pinhole flow of Equations 4-4 and 4-12 to 4.22, described in Chapter 4. Figure 6-19 is a plot of production rate versus DPcom to help explain the first 2 steps of using this strategy with PTA to monitor well performance.

- From the 1st PTA at q_1 the completion skin or its skin completion pressure drop (DPcom$_1$) is obtained. Using the inputs of pinhole and filter cake properties (UFA, L_{int}, and k_{int}) and DPcom$_1$ in Equations 4.4 to 4.10, the actual pinhole flow area (i.e., total number of pinholes times UFA) is determined. The pinhole curve of q versus DPcom is then generated by keeping the filter cake properties and calculated pinhole flow area constant. From the 1st PTA, with known q_1 and DPcom$_1$, we can also generate results of Hawkins' model (Eq. 4.2) or the entire reservoir OH wellbore flowing (100 % flow area). From the Hawkins' model, we use the same input L_{int} from CT Scan and adjust the k_{int} to satisfy the measured DP_{com1}. The Hawkins' line is generated by keeping these filter cake properties constant. Note, the k_{int} value is different for the Hawkins and pinhole cases. Using the pinhole curve, the next higher rate (q_2) can be decided based on the magnitude of DPcom forecasted and accepted within the completion impairment risk.

- Following the ramp-up to q_2 and after the rate is stabilized, a 2nd PTA at q_2 is collected and the completion response DPcom$_2$ is determined. The placement of this DPcom$_2$ and q_2 point on the q vs DPcom plot can reveal how the completion is performing relative to the predicted performance curve from the 1st PTA. In this example, 5 possible values of DPcom$_2$ at q_2 are shown as Points a, b, c, d, and e in Figure 6-19.

  ➢ At Point a, DPcom$_2$ is less than predicted by Hawkins and Pinhole curves. The completion is performing better than predicted or cleaning up. For Hawkins' model the second k_{int} has increased as compared to k_{int1}. For Pinhole's model

the number of pinholes or the total pinhole flow area has increased (since pinhole UFA, L_{int} and k_{int} are assumed unchanged between rate changes).

➤ At Point b, DPcom$_2$ is on the Hawkins curve but still less than Pinhole model prediction. The completion is performing as predicted by Hawkins and better than the Pinhole's prediction.

➤ At Point c, DPcom$_2$ is higher than predicted by Hawkins but is still less than predicted by the Pinhole curve. So, according Hawkins' model the completion is impairing or k_{int} is reducing. However, according to the Pinhole's model the completion is still cleaning up.

➤ At Point d, DPcom$_2$ is even higher than predicted by Hawkins but DPcom$_2$ is on the Pinhole curve. So, according Hawkins' model the completion is impairing but is performing as expected for the Pinhole's model.

➤ Finally, at Point e, DPcom$_2$ is higher than predicted by Hawkins and Pinhole curves. In this case the completion is impairing for both models.

DPcom results from these 5 points illustrate how PTA response from a lower production rate can be used to assess the completion performance at a higher rate. This provides direct feedbacks to surveillance engineers and enables evaluations before deciding to continue ramp-up or taking other appropriate actions. If the Hawkins' model were used then Points c, d and e show increasing risks of completion impairment and decision to choke back might be imposed. However, if the Pinhole's model is used, only Point e shows completion impairment. So, using Hawkins' model can potentially limit ramping-up well due to impairment concern as compared to Pinhole's model.

- Assuming that the actual $DPcom_2$ is on Point c, a new Pinhole curve is generated using the larger number of pinholes (Point c is cleaning up). The decision for the next higher rate q_3 can then be decided based on the forecasted $DPcom_3$. The process repeats with a 3rd PTA at q_3.
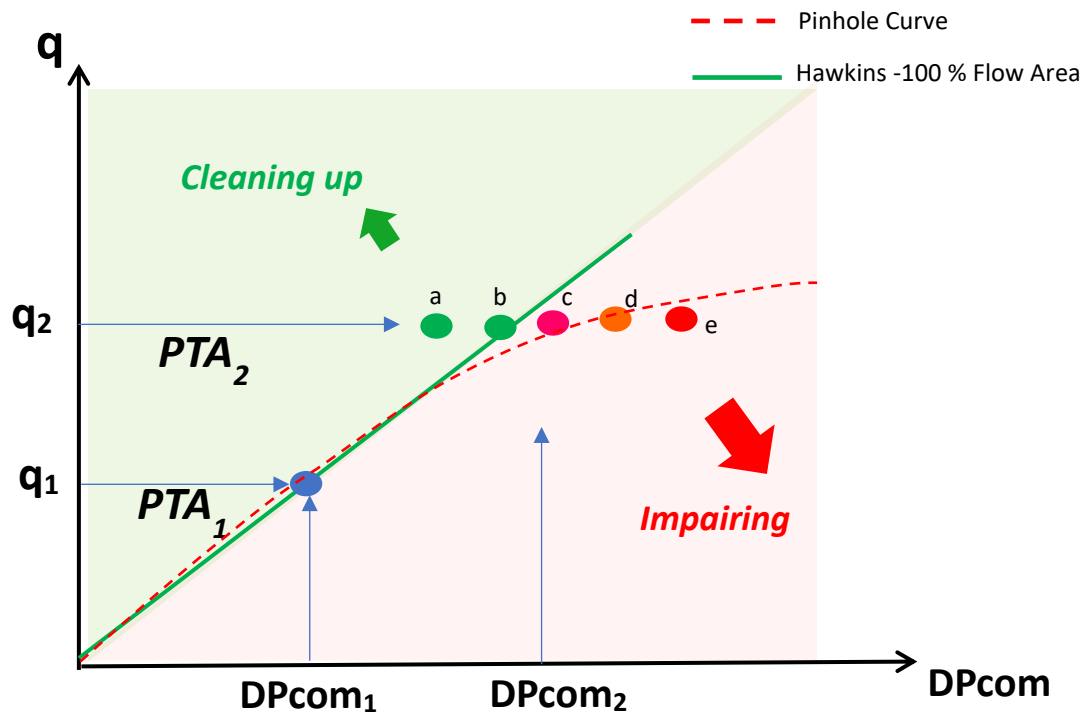
Figure 6-19: Flow Rate vs. Completion Pressure Drop Schematic

Next, an example will be used to illustrate the application of the pinhole model. Required inputs to calculate the total number of pinholes for a given completion skin and pinhole information are given in Table 6-5 as software input screenshot. There are two parts namely: Formation & Pressure Transient Analysis Data and Completion & Lab Data. The completion interval is vertical with a net height of 300 ft and the formation has a permeability of 200 mD. Inputs for the pinhole and filter cake properties are in the

"Completion & Lab Data" Section. Required pinhole inputs are: pinhole UFA, internal filter cake thickness and permeability. These values are obtained using RPT, CT-Scans, and Reduced Order Modeling presented in Chapters 3 and 6. For this example we assumed a filter cake permeability (k_{int}) and thickness (L_{int}) of 2 mD and 0.02 in, respectively. The pinhole diameter can be calculated using a "Core Test Unit Flow Area" of 50% from a "Core Test Diameter" of 1.5 in from following equation.

$$D_{pinhole} = \sqrt{\frac{UFA}{100}} D_{test} \, .$$

(6.10)

From the first PTA at a production rate of 10,000 STB/d, the mechanical skin value is 3 units.

Table 6-5: Required Inputs for Calculations

Formation & Pressure Transient Analysis Data

Formation Permeability (md)	k_form	200
True Stratigraphic Net Pay Thickness (ft)	h	300
Formation Volume Factor (RB/STB)	B_o	1.30
Formation Fluid Viscosity (cp)	μ_o	0.70
Formation Fluid Density (lb_m/ft^3)	ρ_o	49.85
Formation Drainage Radius (ft)	r_e	2,000
PTA: Production Rate (STB/d)	q	10,000
PTA: Mechnical Skin (-)	S_{mech}	3

Completion & Lab Data

Drill Bit or Bore Hole Diameter (in)	D_w	7.25
Bore Hole to Screen OD Annular Clearance (in)	AC	0.5
Measured Length of Open Hole Interval (ft)	L	300
Core Test Unit Flow Area (%)	UFA	50
Core Test Diameter (in)	D_{test}	1.5
Internal Filter Cake Thickness (in)	L_{int}	0.02
Internal Filter Cake Perm (md)	k_{int}	2

1) Figure 6-20 presents the simulation results and shows two calculated curves. The first PTA with a skin of 3 units at 10,000 STB/d resulted in a $DPcom_1$ of 64.2 psi (Eq. 4-1) (Blue circle). Using the relationships of completion skin for perforated liner (Eqs. 4.8-4.22), we can calculate the total pinhole flow area and pinhole inflow velocity, (V_c), to be 164 ft^2 and 0.0052 ft/s, respectively. With the known pinhole flow area and inputs of k_{int} and L_{int}, the pinhole curve (red color) for increasing flow rate is generated. The Hawkins' curve (green color) for 100% open flow area of 569 ft^2 is also drawn after calculating a filter cake permeability that matches the

inputted skin of 3. The Hawkins' velocity at 10,000 STB/d is 0.0015 ft/s. As expected with a smaller total pinhole flow area the inflow velocity (V_c) is larger than the Hawkins' case. Similarly, as can be seen from the generated q vs DPcom curves, the DPcom for a given rate is higher for the pinhole case than Hawkins. However, flow velocities for both pinhole and Hawkins cases are small.

2) Based on the pinhole curve, the next ramp-up rate of 20,000 STB/d with a forecasted DPcom of 200 psi was chosen. This 200 psi is viewed to be low and acceptable. After the 20,000 STB/d was stabilized a 2nd PTA was taken and resulted in a skin of 9.3 units or a DPcom$_2$ of 400 psi. This 2nd PTA point (DPcom$_2$ of 400 psi and q of 20,000 STB/d) is depicted in Figure 6-21. Because DPcom$_2$ is higher than the pressure forecasted from the 1st PTA, this suggests the completion is experiencing impairment with a reduction of total pinhole flow area from 169 to 137 ft^2.

3) A new curve is created based on the new flow area from the 2nd PTA as shown in Figure 6-22. Based on this new curve and depending on the risk tolerance for a maximum acceptable DPcom, the next ramp-up rate can be selected. For example, the DPcom is 720 psi for the next ramp-up rate of 30,000 STB/d. This process can then be repeated with a PTA following with each higher rate and generating a new curve to assess the risk of impairment and acceptable DPcom value.
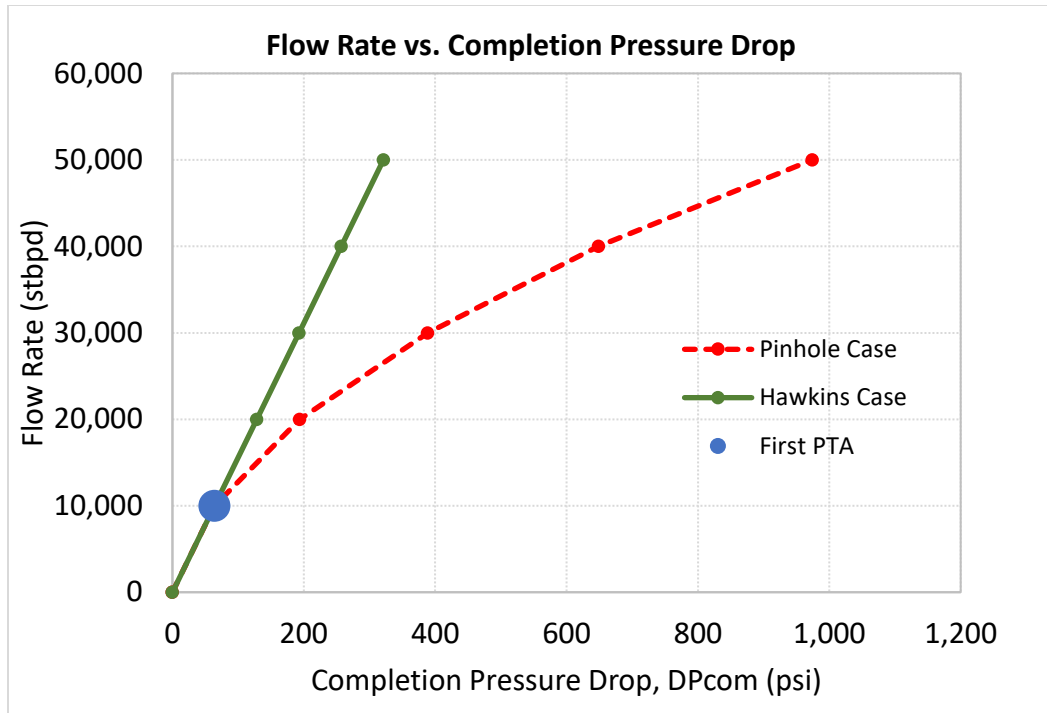
Figure 6-20: Flow Rate vs. Completion Pressure Drop for the First PTA at 10,000 STB/d
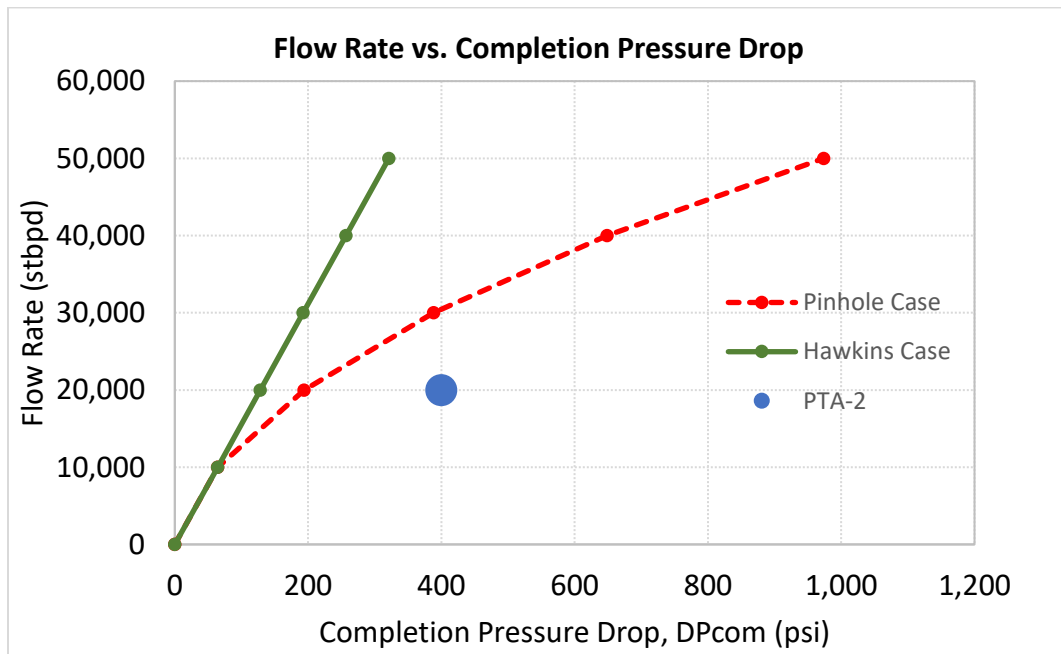

Figure 6-21: Flow Rate vs. Completion Pressure Drop with 2nd PTA
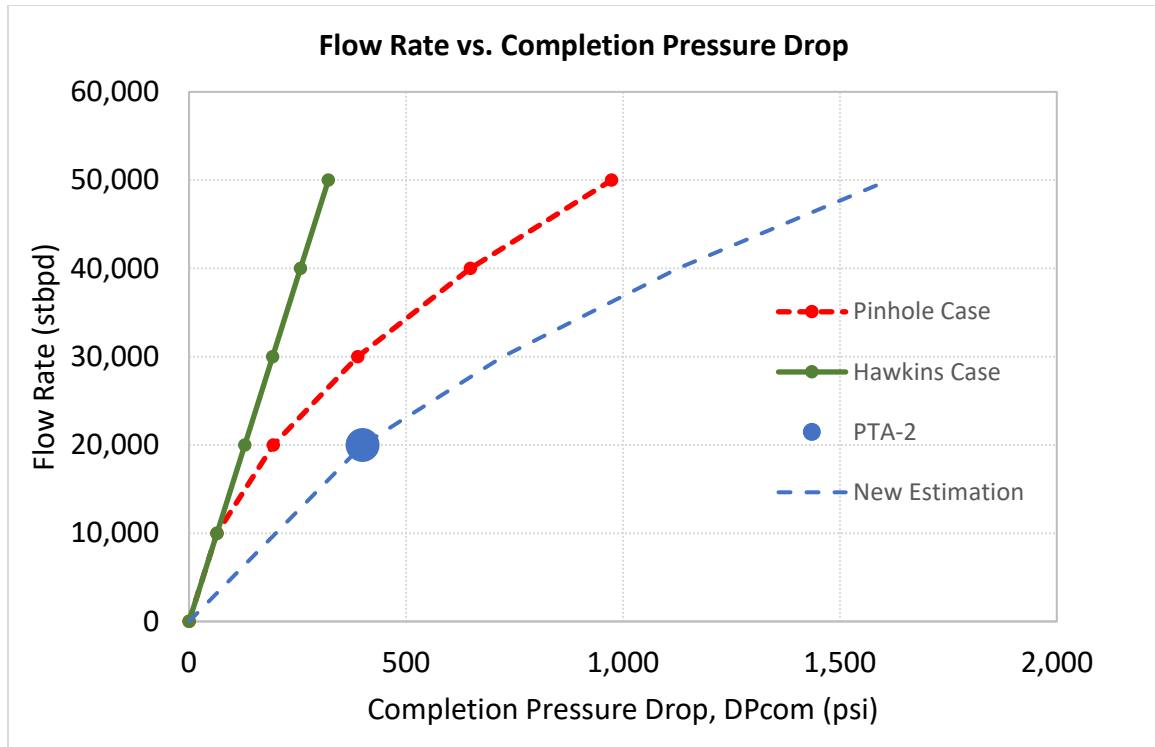
Figure 6-22: Flow Rate vs. Completion Pressure Drop with New Estimation

Based on the total pinhole flow area of the 1st PTA, both flow velocities converging at the top of the screen, V_a, and impinging to the screen, V_s are plotted against the total production rate in Figure 6-23. These velocities are calculated based on a screen surface area along a 1 ft section. Results showed the highest velocity is V_a and suggests the top of the screen is most vulnerable to erosion failure.

Figure 6-23: Flow Rate vs. V_a and V_s

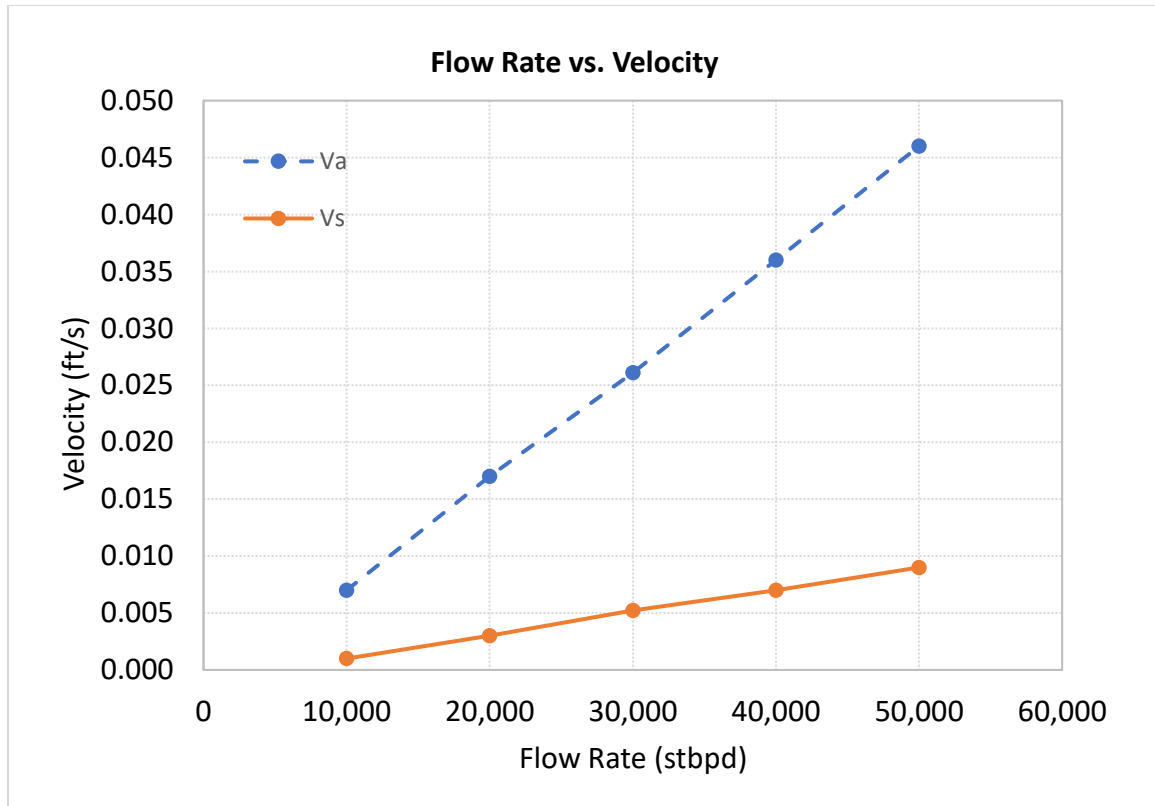Input values of pinhole diameter (UFA) and filter cake properties of k_{int} and L_{int} should be taken as a system. The combination of RPT and CT-Scan provides accurate ΔP across the test sample and L_{int}; however, k_{int} depends on the interpreted UFA. This was demonstrated in Table 6-3 using lab results of RPT 34 sample (ΔP of 0.8 psi and L_{int} of 0.02 in (Figure 6-1)) and showing the calculated k_{int} for different UFA values. Even with a CT-Scan image of Figure 6-2, the determination or interpretation of UFA can be difficult. We evaluated the effects of using each pair of k_{int} and L_{int} for a given UFA as input into the pinhole flow model. These runs were made with a production rate of 10,000 STB/d and a DPcom of 64.2 psi. Table 6-6 summarizes these results. From the table, the selection of the pinhole UFA and corresponding k_{int} has a large impact on the calculated results.

Reducing the UFA from 75% to 25% increases the pinhole inflow velocity (V_c) from 0.0070

ft/s to 0.0178 ft/s. Therefore, it is not appropriate to make sensitivity runs by changing

any one of the three pinhole & filter cake inputs (UFA, k_{int}, and L_{int}) without adjusting the

others two. The application of the Reduced Order Model (ROM) in Section 6.3 facilitates

the determination of these inputs as a system.

Table 6-6: Sensitivity Cases L_{int}, k_{int} and UFA on Pinhole Completion Velocity

Case	Input			Output		
	L_{int}	k_{int}	UFA	Total Pinhole Number	Total Pinhole Area	V_c
	inch	mD	%	-	ft^2	ft/s
1	0.02	9	75.0	13127	120.8	0.0070
2	0.02	14	50.0	15013	92.1	0.0092
3	0.02	31.5	25.0	15506	47.6	0.0178

Figure 6-24 shows the comparison of the Hawkins case with the Pinhole case that has

100% UFA (i.e., the pinhole diameter is the same as the core sample diameter in the RFT).

As can be seen from the graph, the result of pinhole case with 100% UFA is not equal to

the Hawkins Case. The reason is that uncovering the entire surface area of the OH

completion interval with pinholes will still leave areas (between pinholes) that are

covered with damaged permeability and not contributing flow. The Hawkins case

assumes 100% of the OH surface area is open for production. Therefore, for a given

production rate, pinhole model always predicts a higher DPcom than Hawkins model. For

well surveillance applications, having a PTA's DPcom larger than Hawkins' model might

still be less than the pinhole's model. To avoid limiting production unnecessarily the pinhole model should also be checked.
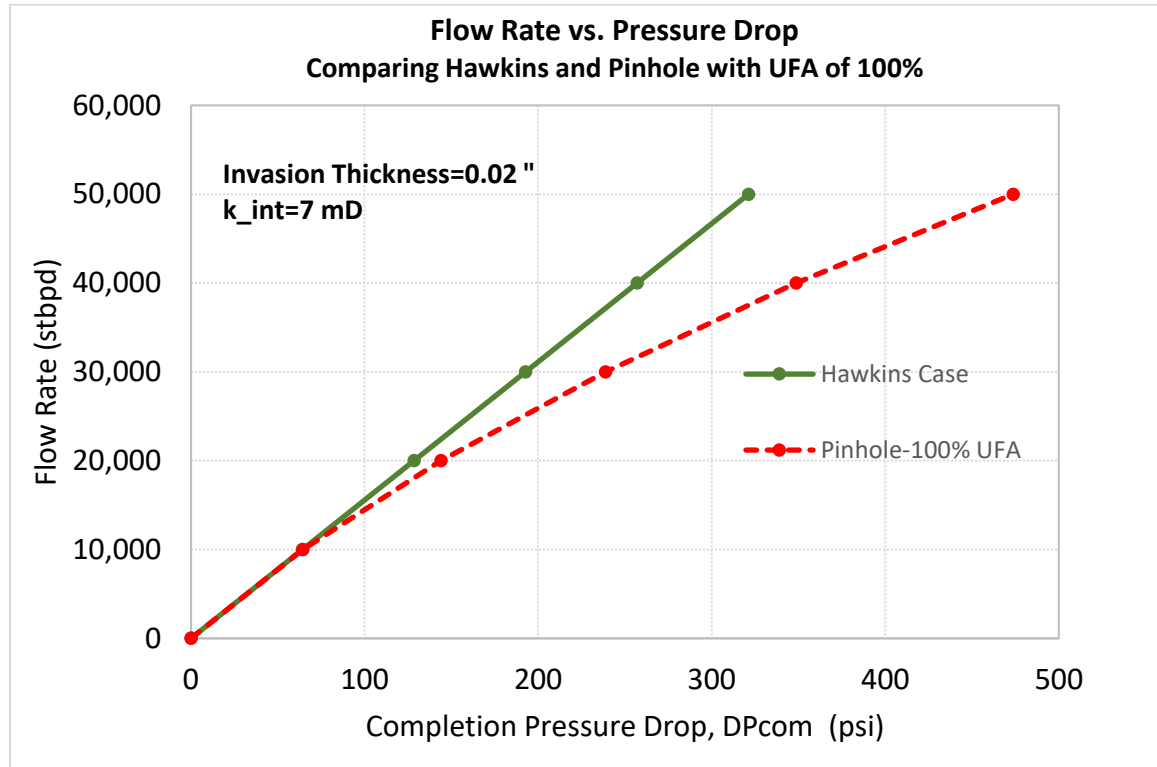

Figure 6-24: Flow Rate vs. Completion Pressure Drop, 100% UFA Pinhole Case

Additional sensitivity analyses are conducted to evaluate the prediction of completion pressure drop vs. flowrate as a function of different completion variables. Figure 6-25 presents the completion pressure drops for different internal cake permeabilities. For given rate, UFA and L_{int}, the completion pressure drop increases with decreasing internal cake permeability where k_{int} has high impact on DPcom. As explained before, UFA and k_{int} are coupled for a given L_{int}, therefore for a UFA of 50% and L_{int} of 0.02 in, there is only one k_{int}. The application of ROM is an effective tool to calculate the correct k_{int}. As can be seen from the figure, selecting random k_{int} for the specific UFA and L_{int} will result in different completion pressure drops.

69

Figure 6-26 presents the effect of formation permeability (k_form) on completion

pressure drop. As a surveillance tool, skin and k_form are paired and varying k_form result

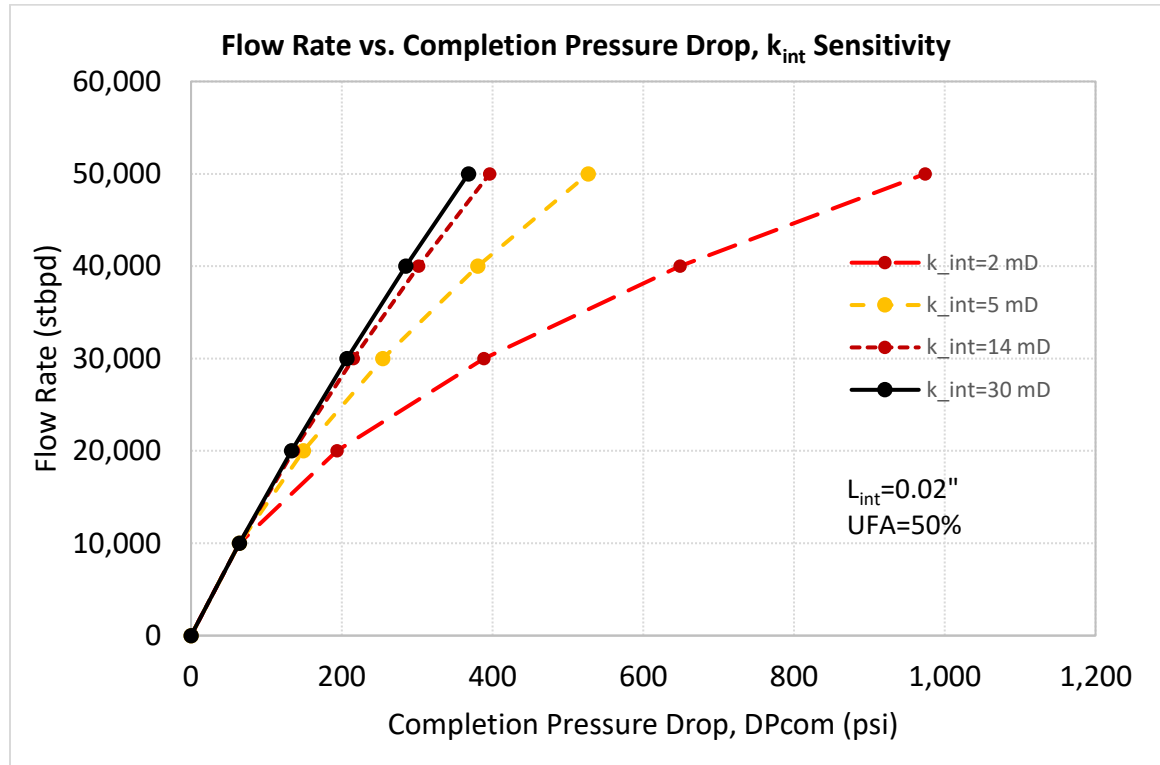in different completion pressure drop estimations.

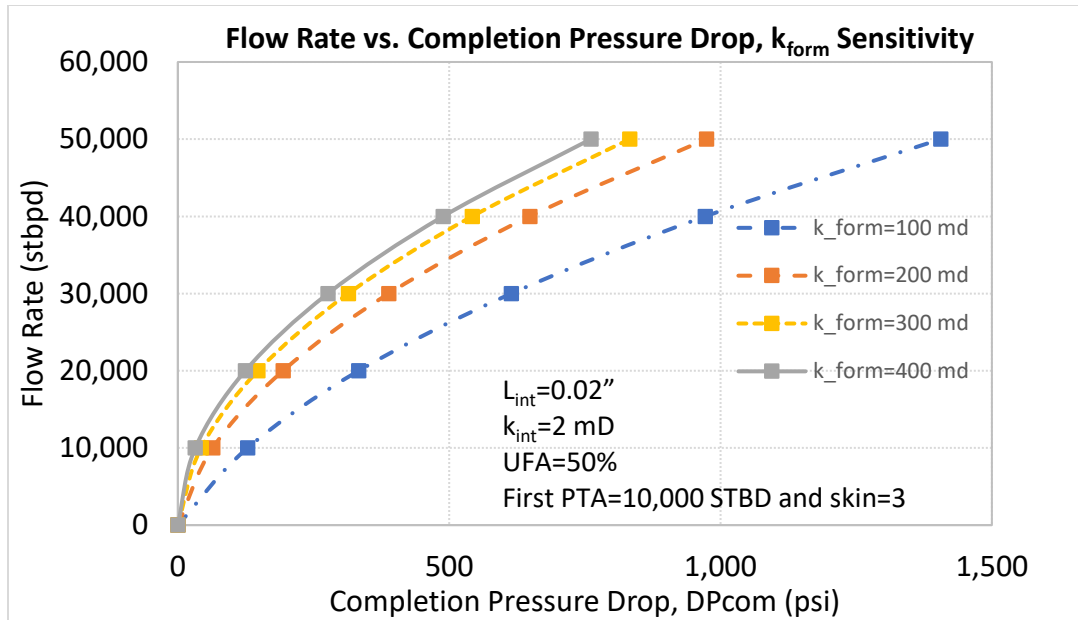Figure 6-25: Flow Rate vs. Completion Pressure Drop with k_{int} Sensitivity

Figure 6-26: Flow Rate vs. Completion Pressure with, k_form sensitivity

Figure 6-27 presents flow rate vs. completion pressure drops as a function of mechanical skin value from the first Pressure Transient Analysis where increasing the skin will result in higher completion pressure drop values.
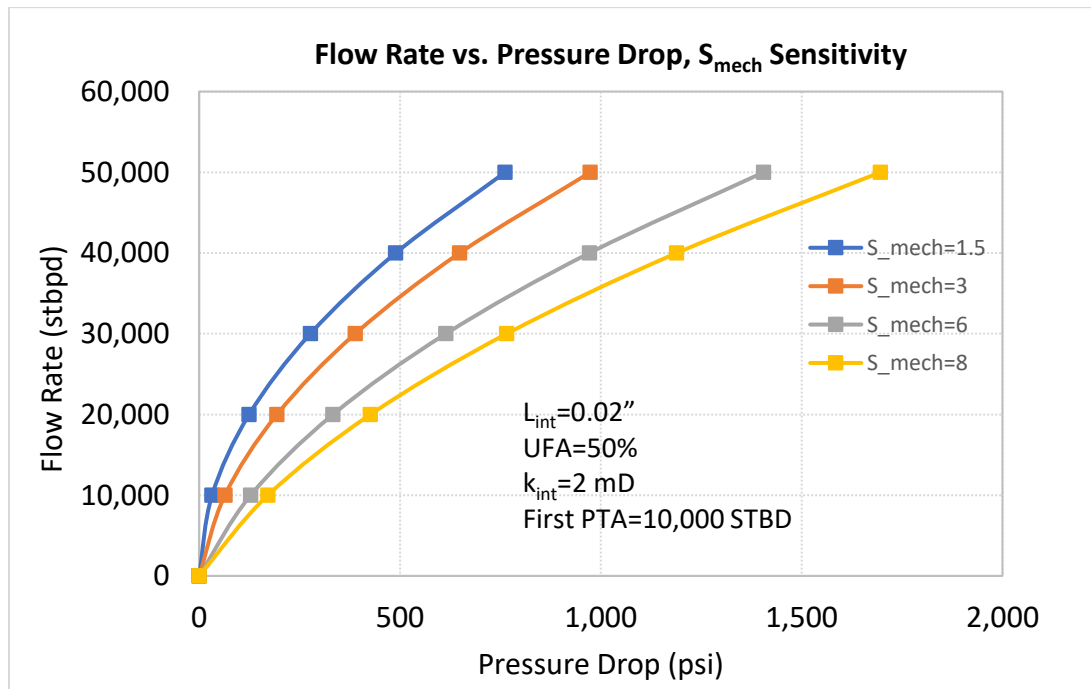

Figure 6-27: Flow Rate vs. Completion Pressure Drop Schematic, S_mech sensitivity

6.5 Flow Distribution of OH-SAS System by Network Analysis

This section shows the network system built to model the flow velocity distributions in the OH-SAS completion. The section also provides results for different completion scenarios to understand the impacts of completion designs and pinhole flow on velocity distributions.

Analysis started with creating various network models and comparing model results with PIPESIM®, a software that allows steady state flow simulation of pipeline network systems. Figure 6-28 presents a screenshot from PIPESIM® graphical user interface. The first model consists of a pipeline system of 2 loops with 7 branches and 2 sources. Output comparisons between PIPESIM® and network model of flow rate and pressure drops are shown in Table 6-7 and Table 6-8, respectively. Network model and PIPESIM® results are in the range of 1%.
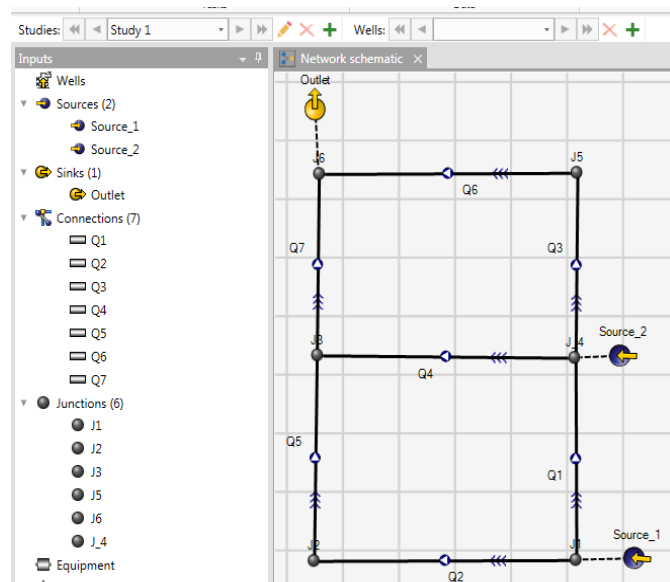

Figure 6-28: PIPESIM Model Graphical User Interface

Table 6-7: Flow Rate Comparison between PIPESIM and Network Model

Branch	PIPESIM	Network Model	Error
Flow Rates (bpd)			
Q1	4,701	4,702	0%
Q2	5,299	5,298	0%
Q3	8,859	8,861	0%
Q4	5,842	5,841	0%
Q5	5,299	5,298	0%
Q6	8,859	8,861	0%
Q7	11,141	11,139	0%

Table 6-8: Pressure Drop Comparison

	PIPESIM	Network Model	Error
Total Pressure Drop (psi)			
J1-J2	0.334	0.330	1%
J2-J3	43.70	43.73	0%
J4-J3	0.40	0.40	1%
J1-J4	43.63	43.66	0%
J4-J5	44.23	44.26	0%
J3-J6	44.70	44.73	0%
J5-J6	0.87	0.86	1%

A second example is a 5 loop system with 5 sources as depicted in Figure 6-29. Table 6-9 compares calculated flow rates between network model and PIPESIM®. Results have errors of less than 1%.
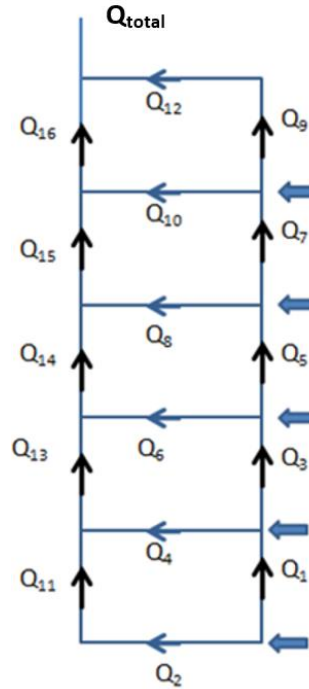
Figure 6-29: Schematic of 5 Loop, 5 Source System

Table 6-9: Flow Rate Comparison Between Network Model and PIPESIM for 5 Loop and 5 Source System

	Flow Rates (bpd)		
	Network System	PIPESIM	Error (%)
Q1	4,997	4,996	0.02
Q2	5,003	5,003	0.00
Q3	9,986	9,986	0.00
Q4	5,010	5,010	-0.01
Q5	14,924	14,923	0.01
Q6	5,062	5,063	-0.01
Q7	19,466	19,462	0.02
Q8	5,458	5,461	-0.05
Q9	21,134	21,125	0.04
Q10	8,332	8,336	-0.05
Q11	5,003	5,003	0.00
Q12	21,134	21,125	0.04
Q13	10,014	10,014	0.00
Q14	15,076	15,077	-0.01
Q15	20,534	20,537	-0.01
Q16	28,866	28,874	-0.03

A final comparison is for the same 5 loop network but with 3 sources distributed every other node as depicted in Figure 6-30. Table 6-10 shows the flow rate comparisons between the network model and PIPESIM®. Again errors are less than 1%. These 3 examples demonstrate the network model developed in the dissertation is delivering accurate results as predicted by PIPESIM®.
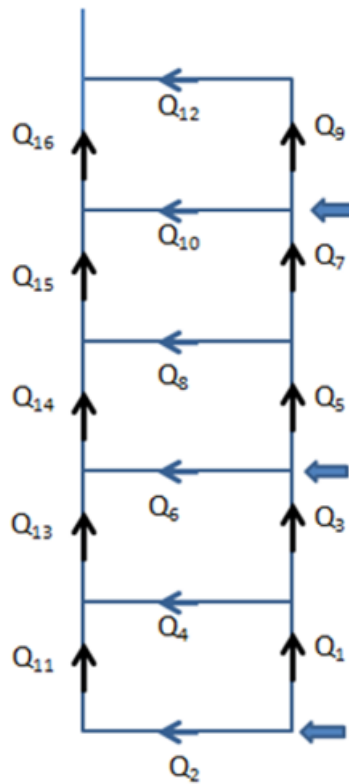

Figure 6-30: Schematic of 5 Loop, 3 Source System

Table 6-10: Flow Rate Comparison, 5 Loop, 5 Source

	Flow Rate (bbl/d)		
	Network System	Pipesim	Difference (%)
Q1	9,682	9,684	-0.02
Q2	6,984	6,982	0.03
Q3	7,170	7,168	0.03
Q4	2,512	2,515	-0.12
Q5	17,299	17,301	-0.01
Q6	6,537	6,533	0.06
Q7	15,038	15,030	0.05
Q8	2,261	2,271	-0.44
Q9	21,405	21,398	0.03
Q10	10,299	10,298	0.01
Q11	6,984	6,982	0.03
Q12	21,405	21,398	0.03
Q13	9,497	9,498	-0.01
Q14	16,034	16,032	0.01
Q15	18,294	18,303	-0.05
Q16	28,594	28,602	-0.03

Following the verification of the network results with PIPESIM®, the network model is used to describe and analyze the flow rate distributions of OH-SAS completion. Simulations are conducted for two different sand screen configurations. They are shown in Figure 6-31 and can be described as follows:

1) Sand screen starts from the top of the reservoir (no screen overlap)

2) Sand screen starts from above the reservoir (with screen overlap)

where

V_c: Downhole flow rate over the total open flow area of the completion

V_s: Radial velocity impinging on the screen

V_a: Maximum convergent (radial) velocity entering to the top screen

V_{sc}: Maximum scouring velocity flowing axially in the annulus

AC: Annular clearance or annular gap. AC = r_w – (screen OD/2)

Screen Overlap = Length of screen above the reservoir formation (can't be less than 0)

Screen Length = Reservoir height (h) + Screen Overlap

The following cases will be done for the Hawkins' model or with 100% wellbore inflow area. This means each reservoir node in the network model will have a production source. All simulations will have a formation height of 300 ft, sand screen of 4.5" ID, and a total production rate of 20,000 BPD. Other inputs for these simulations are presented in Appendix C.
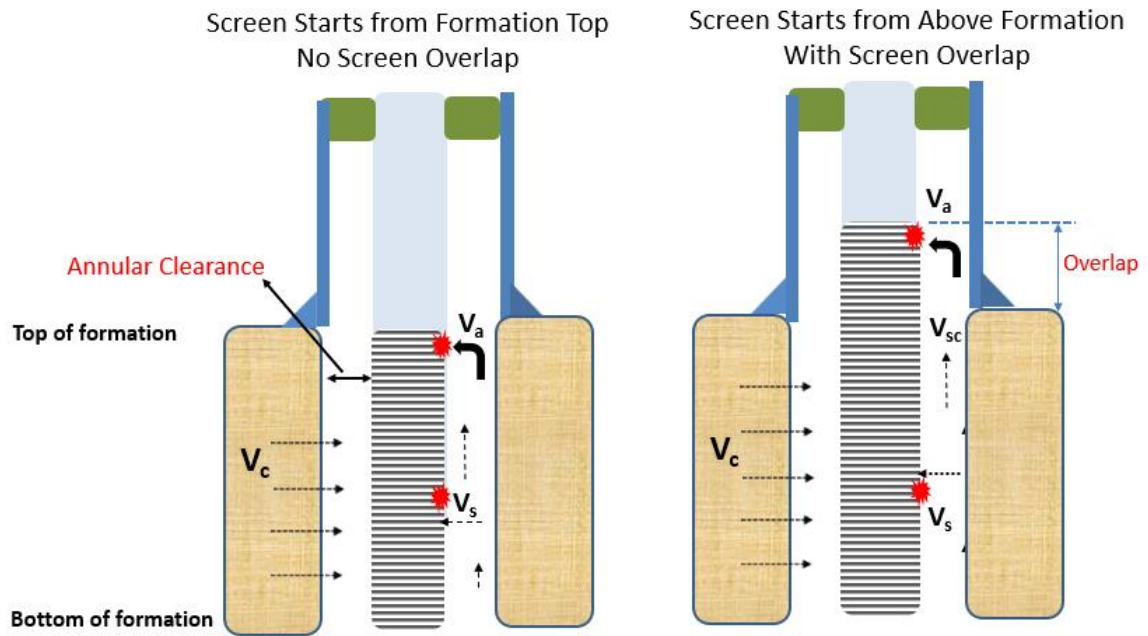
Figure 6-31: Sand Screen Installation Without and With Screen Overlap

Case 1: No screen overlap. Figure 6-32 presents the cumulative axial flow rate profile in the annulus along the length of the screen. The bottom of the screen is at 0 ft and the top of the screen is at 300 ft (since there is no screen overlap). Figure 6-33 shows the schematic of this annular (axial) flow in the wellbore. As shown in Figure 6-32 , the flow rate increases or accumulates as it flows up along the annulus from bottom to top of screen. Because of the packer, the annular flow reaches a maximum rate and begins to slow down as the axial flow diverts radially to enter into the top sections of the screen.
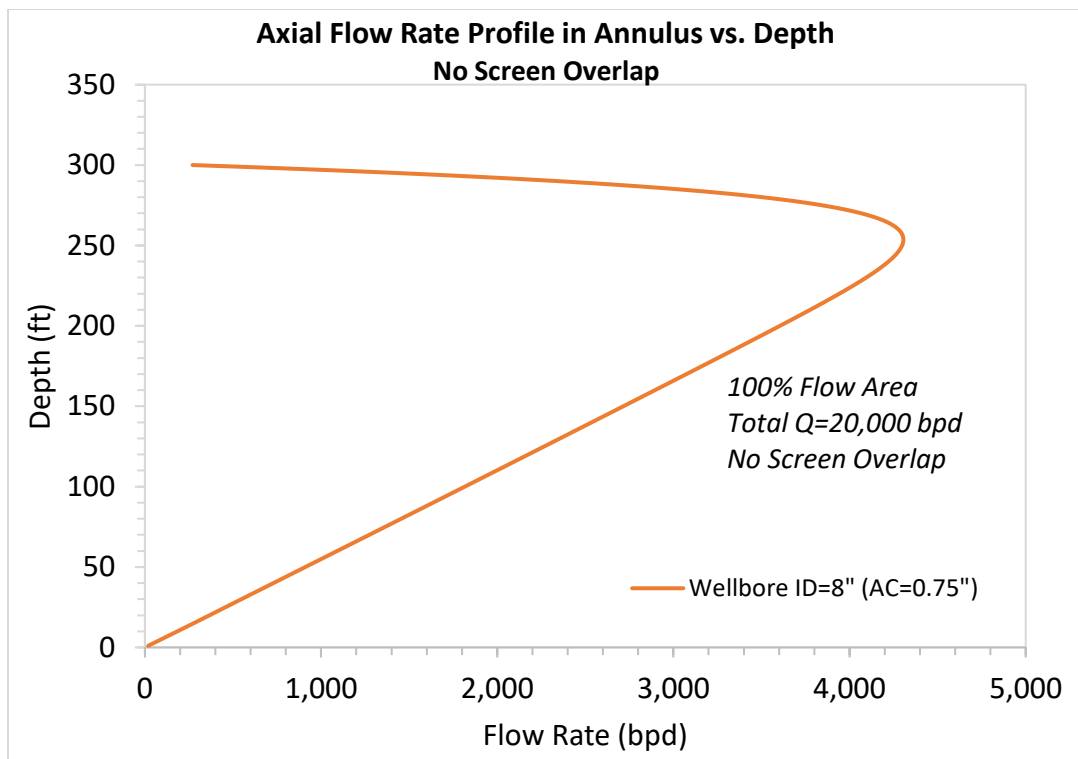
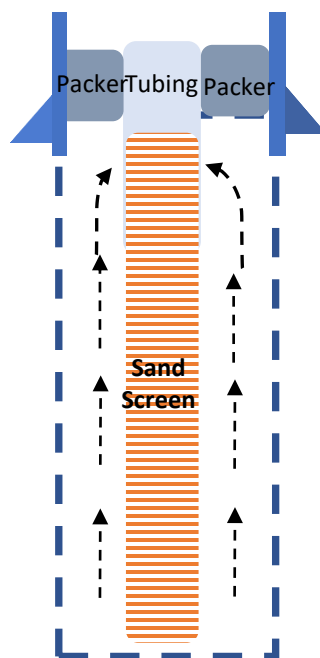Figure 6-32: Axial Flow Rate Profile in Annulus-No Screen Overlap

Figure 6-33: A Schematic of Flow in the Annulus

Fluid flow rate impinging radially onto screen, as a function of depth is plotted in Figure 6-34 and the flow schematic is illustrated in Figure 6-35. As shown in Figure 6-34, radial flow rate onto the screen stays constant up to a specific depth and starts to increase. The highest radial flow rate is at the top of the screen because the axial annular flow must turn radially into the screen from the top because of the packer's presence.
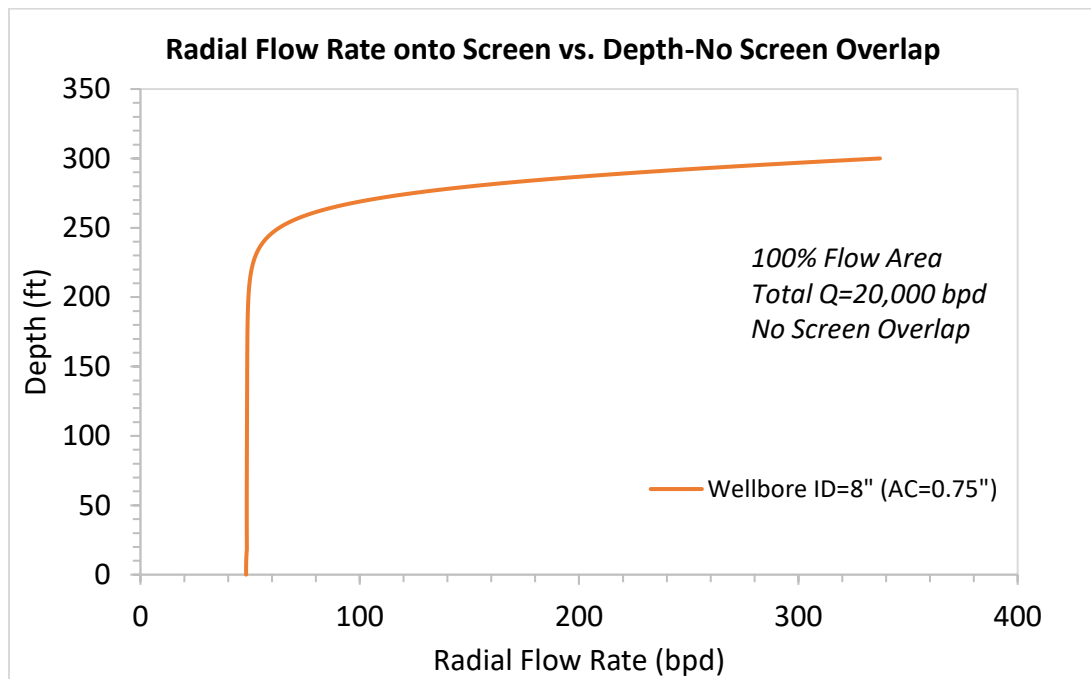

Figure 6-34: Radial Flow Rate onto the Screen-No Screen Overlap
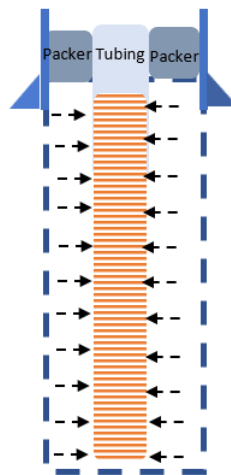

Figure 6-35: Radial Flow onto Screen

Figure 6-36 shows the profile of scouring velocity in the annulus as a function of depth. The scouring velocity is calculated by dividing the annulus flow rate (axial direction) by the area of the annular gap. As can be seen from the plot, the scouring velocity in the annulus increases to a maximum velocity of 2.35 ft/s and then starts to decline as it reaches to the inlet from top of screen. This maximum scouring velocity is labelled as V_{sc}. Figure 6-37 presents the radial velocity magnitude that enters the screen as a function of depth. This radial impingement velocity is calculated based on a screen surface area of 1 ft long. The screen impingement velocity , V_s, remains relatively constant along the screen length and increases until it reaches the maximum value of the convergent velocity, V_a , at the top of the screen. Therefore, the screen impingement erosion risk is highest at the top of the screen due to this maximum convergent velocity, V_a. Note, calculated V_s and V_a values are based on a screen's surface area of 1 foot in length. Screen velocities calculated with different screen lengths will result in different values. However, the axial scouring velocity is based on the annulus' cross section area and is independent of the length interval.
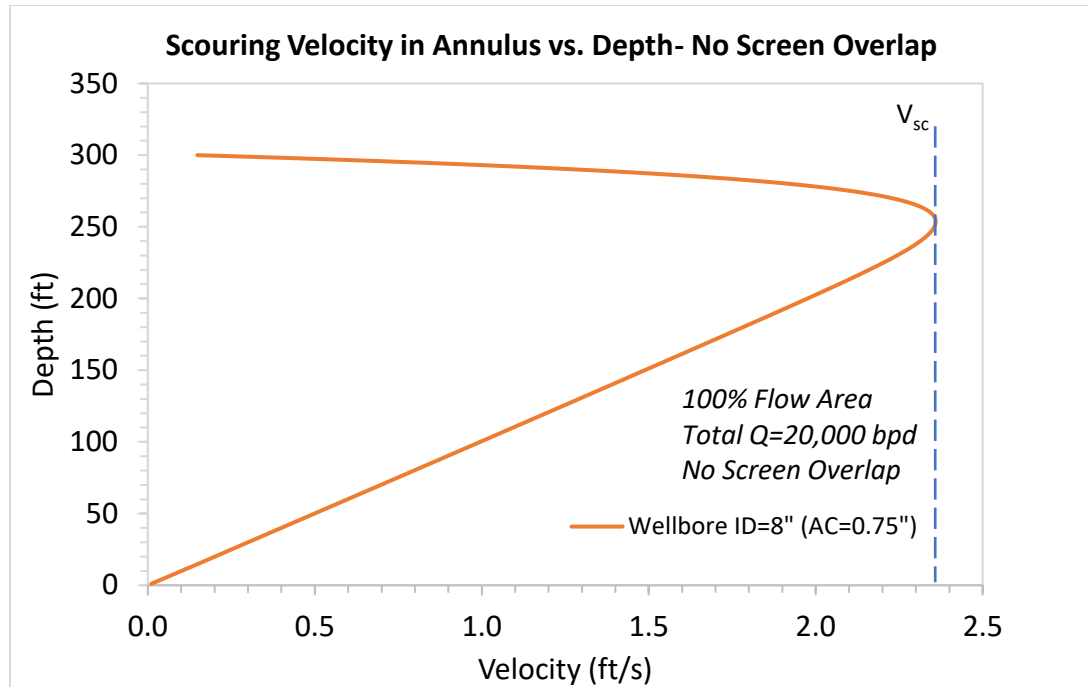
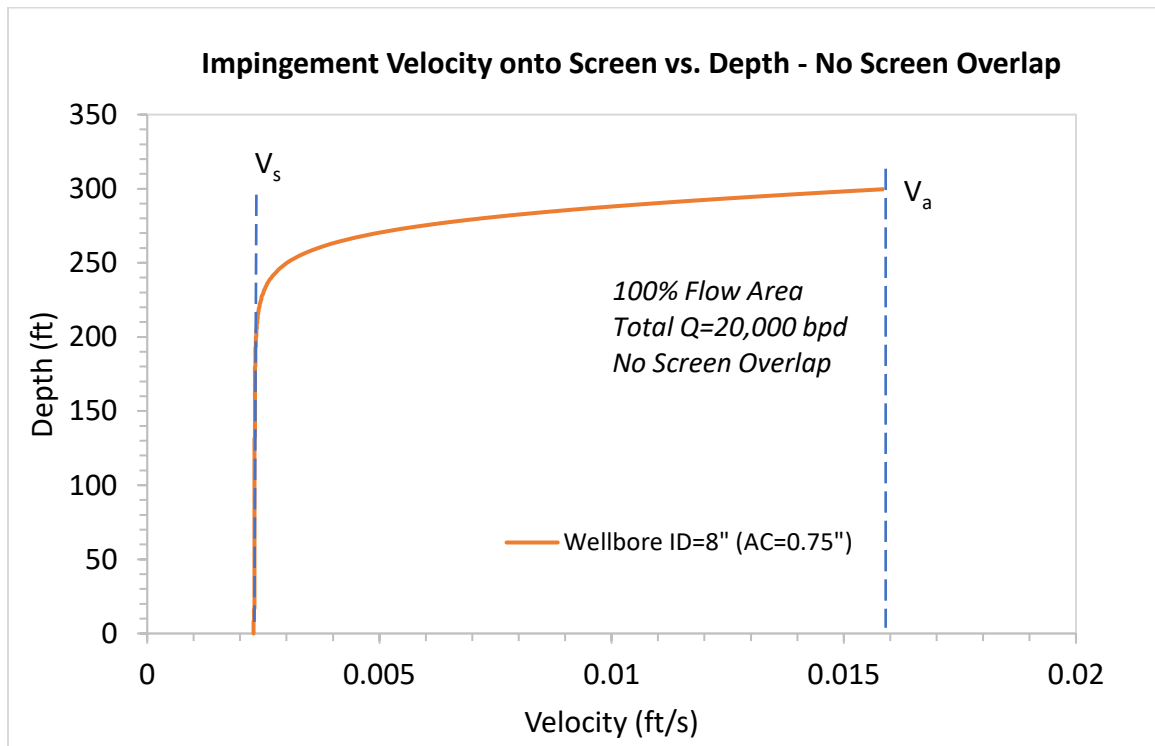Figure 6-36: Scouring Velocity in Annulus vs. Depth – No Screen Overlap

Figure 6-37: Radial Velocity onto Screen vs. Depth – No Screen Overlap

Figure 6-38 presents the scouring, V_{sc}, screen impingement, Vs, and convergent, Va velocities as a function of flow rate. The scouring velocity is much larger than the convergent and impingement velocities. For example, at 30,000 STB/d the scouring velocity is 3.6 ft/s and the convergent velocity at the top of screen is 0.025 ft/s. The high scouring velocity raises potential concerns and risks of screen scouring erosion and borehole enlargement.
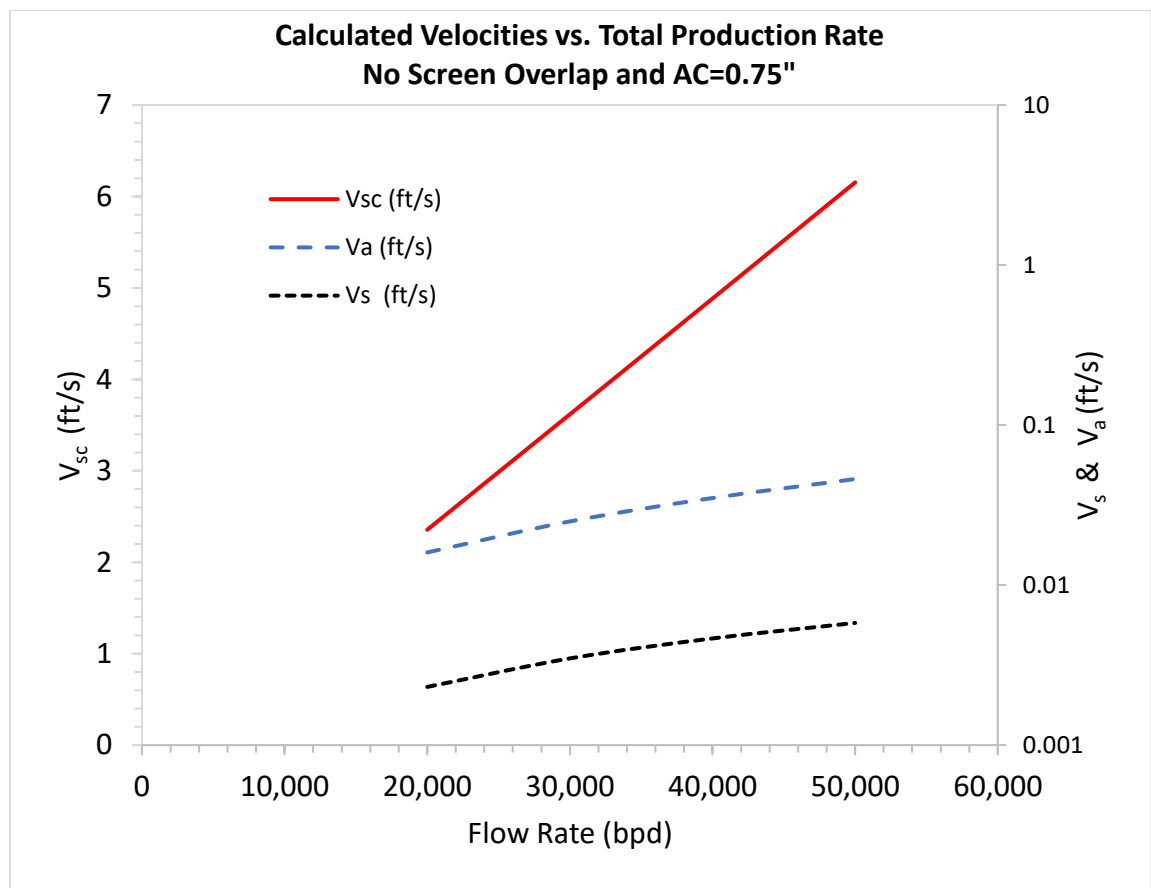

Figure 6-38: Velocities vs Flow Rate (8" Wellbore ID-AC=0.75") – No Screen Overlap

The following sensitivities are conducted to analyze the effect of Annular Clearance (AC). This is the gap between wellbore and the screen as shown in Figure 6-39. Figure 6-40 and Figure 6-41 present the axial flow rate profile in the annulus and the radial flow

rate profile onto screen, for different values of AC, respectively. These figures show increasing the annular clearance diverts more axial flow into the annular region and radial flow at the top of the screen; thereby, increasing the annulus scouring risk (V_{sc}) and screen impingement erosion (V_a) risk, respectively.
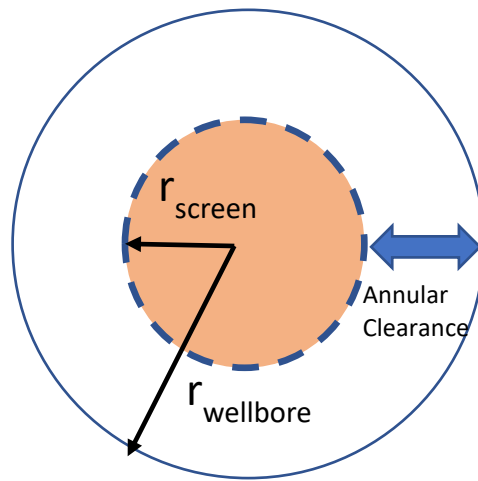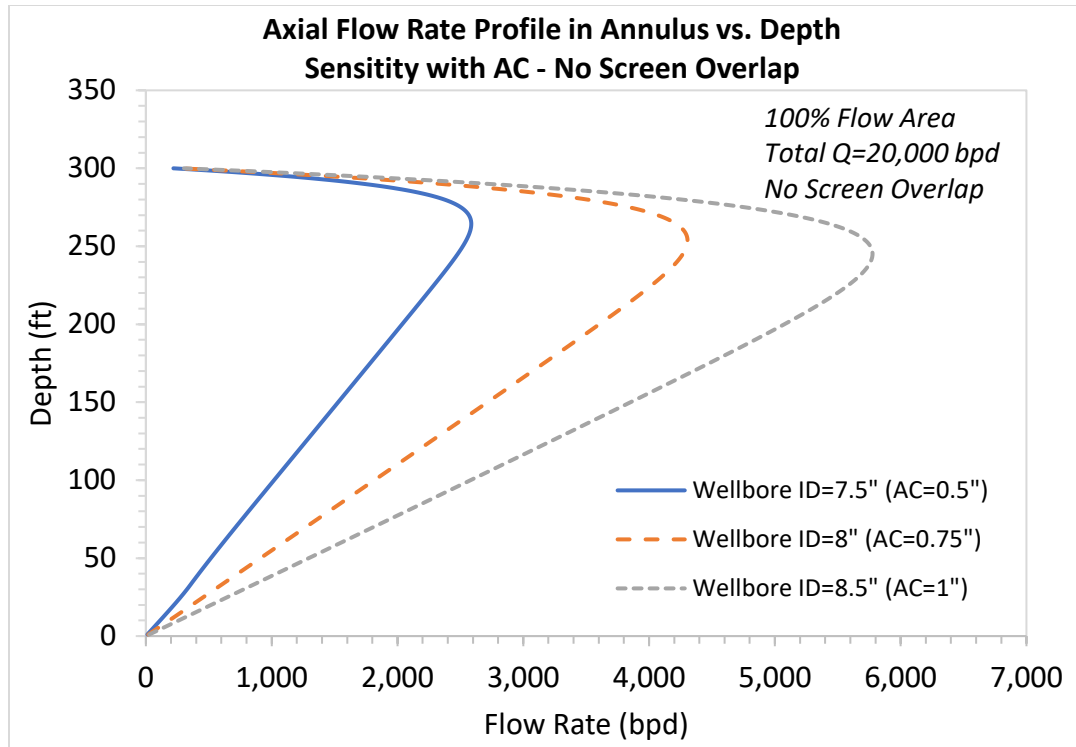

Figure 6-39: Well Top View

Figure 6-40: Axial Flow Rate Profile in Annulus with Different AC - No Screen Overlap
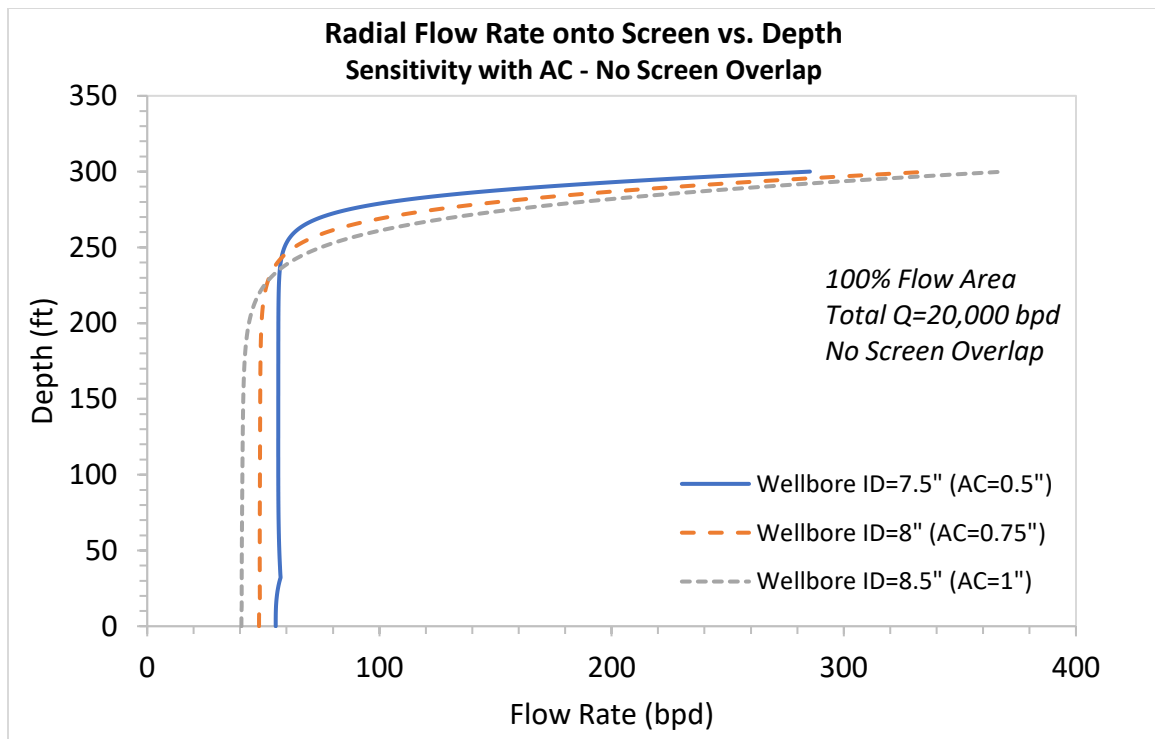
Figure 6-41: Radial Flow Rate onto the Screen with Different AC - No Screen Overlap

To assess the effect of changing the annular roughness on the scouring and impingement flow rate profiles, additional sensitivity runs were made. They are for a constant AC of 0.75 in and flow rate of 20,000 STB/d. Figure 6-42 and Figure 6-43 show reducing the annular roughness from 0.12 in to 0.012 in, increases the axial flow rate in the annulus and the radial flow rate at the top of screen. This is not unexpected as reducing the frictional pressure drop in the annulus will divert more flow into the annulus and more flow converging at the top of the screen.

Figure 6-42: Axial Flow Rate Profile in Annulus with Wellbore Roughness Sensitivity
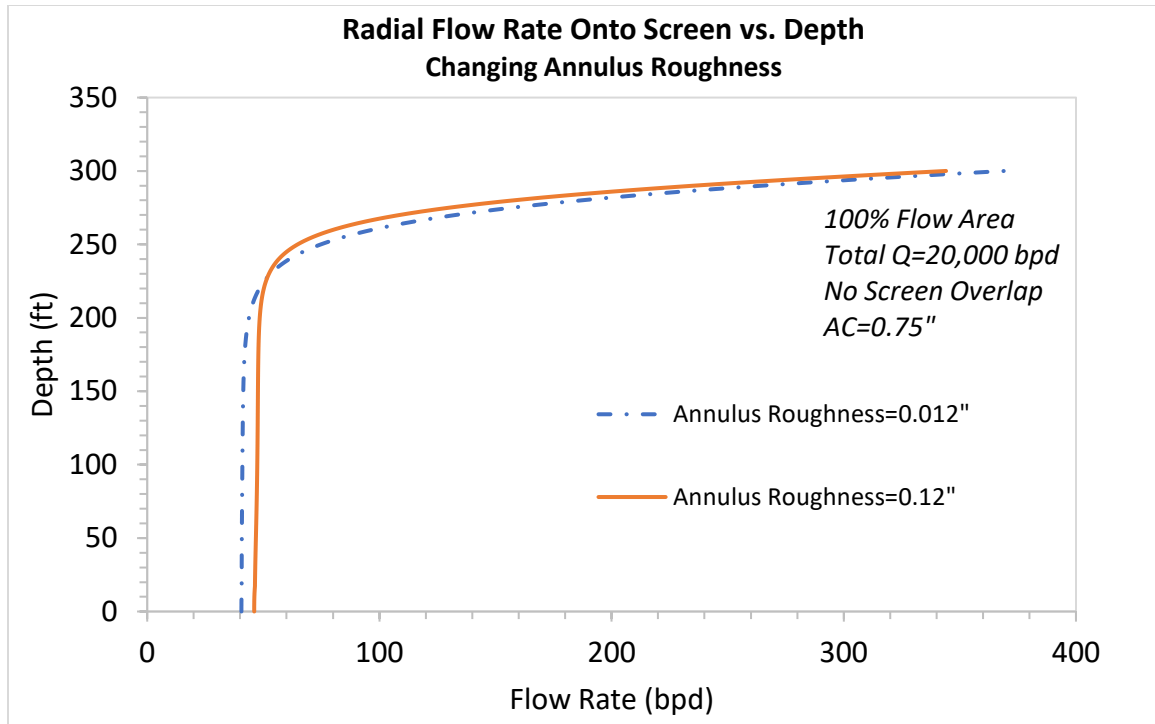
Figure 6-43: Radial Flow Rate onto Screen with Wellbore Roughness Sensitivity

Case 2: With 30 ft of screen overlap.   In this case the top of screen is at 330 ft and the top of formation is at 300 ft. Figure 6-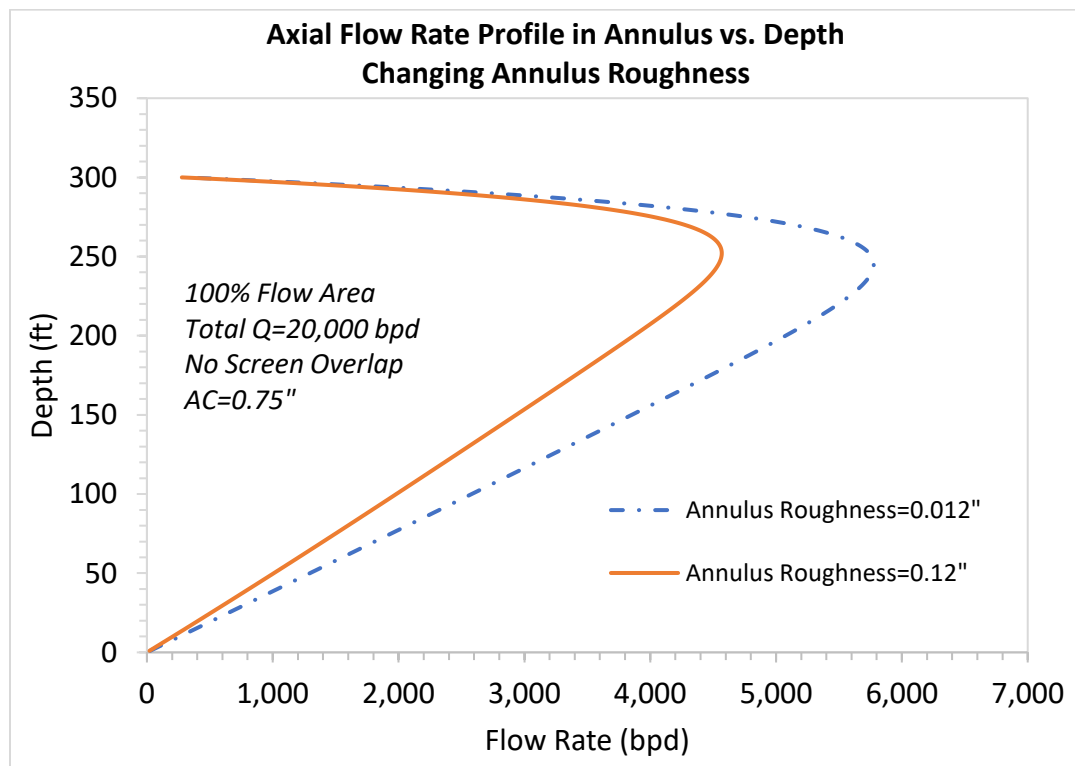44 shows increasing the annular clearance increases the amount of flow rate through the annulus. However, the location of the maximum annular flow rate is moved up closer to the formation top (at around 300 ft) due to the screen overlap which enables the annular flow to go up further before having to divert radially onto the screen top. Figure 6-45 and Figure 6-46 shows the profile of radial flow rate and radial impingement velocity (for screen surface area of 1 ft long) along the screen length, respectively. The maximum radial flow rate and velocity are entering at the top screen (at 330 ft). Similar to Figure 6-40 and Figure 6-41, a larger the annular clearance (AC) would lead to higher radial flow rate and radial velocity (V_a) entering the screen.

Figure 6-44: Axial Flow Rate Profile in Annulus with 30 ft Screen Overlap and Changing AC
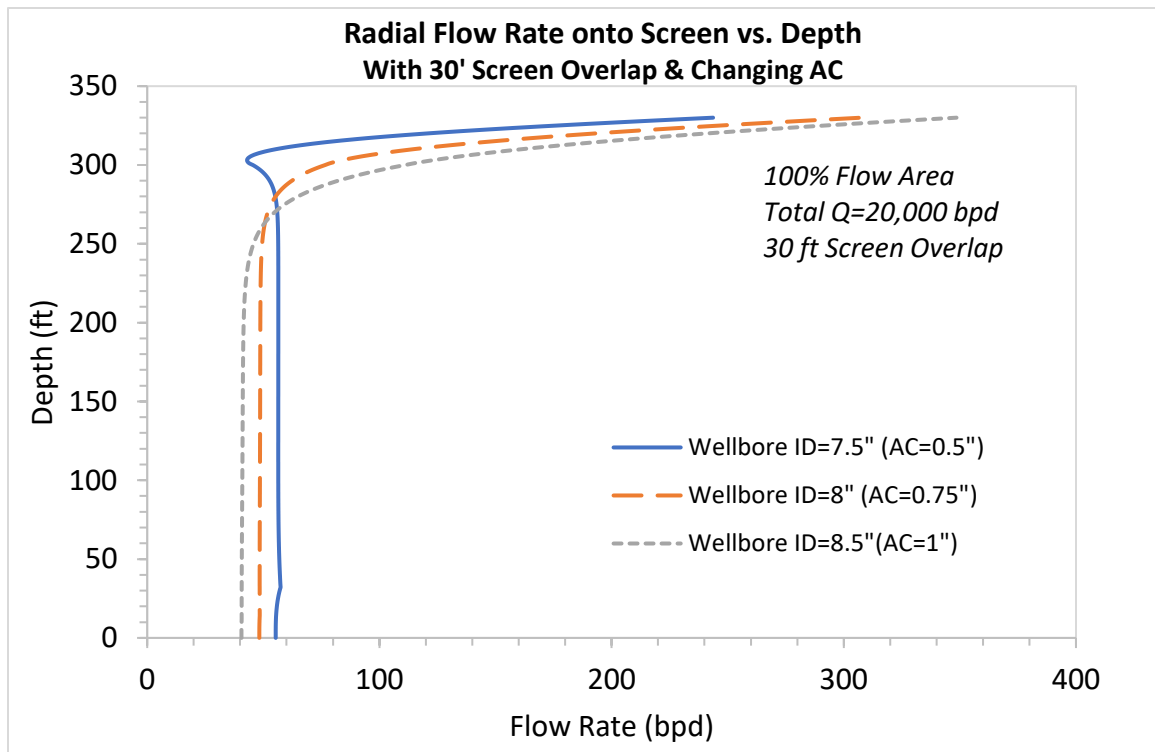
Figure 6-45: Radial Flow into Screen with 30 ft Screen Overlap and Changing AC

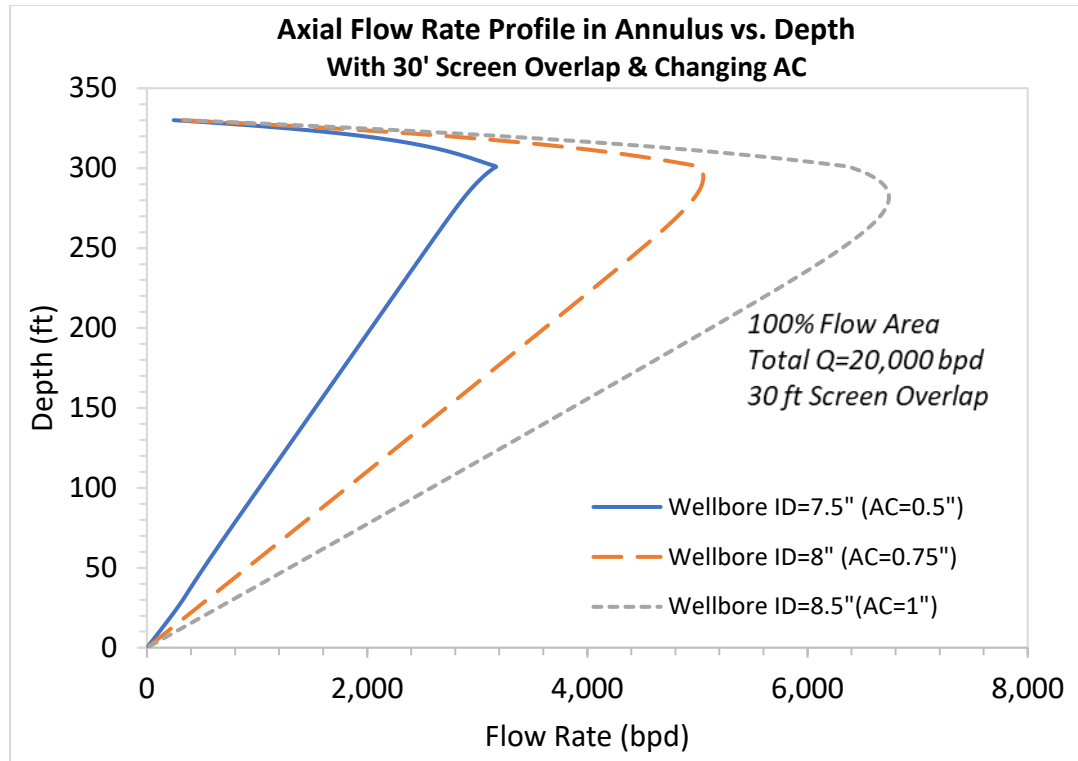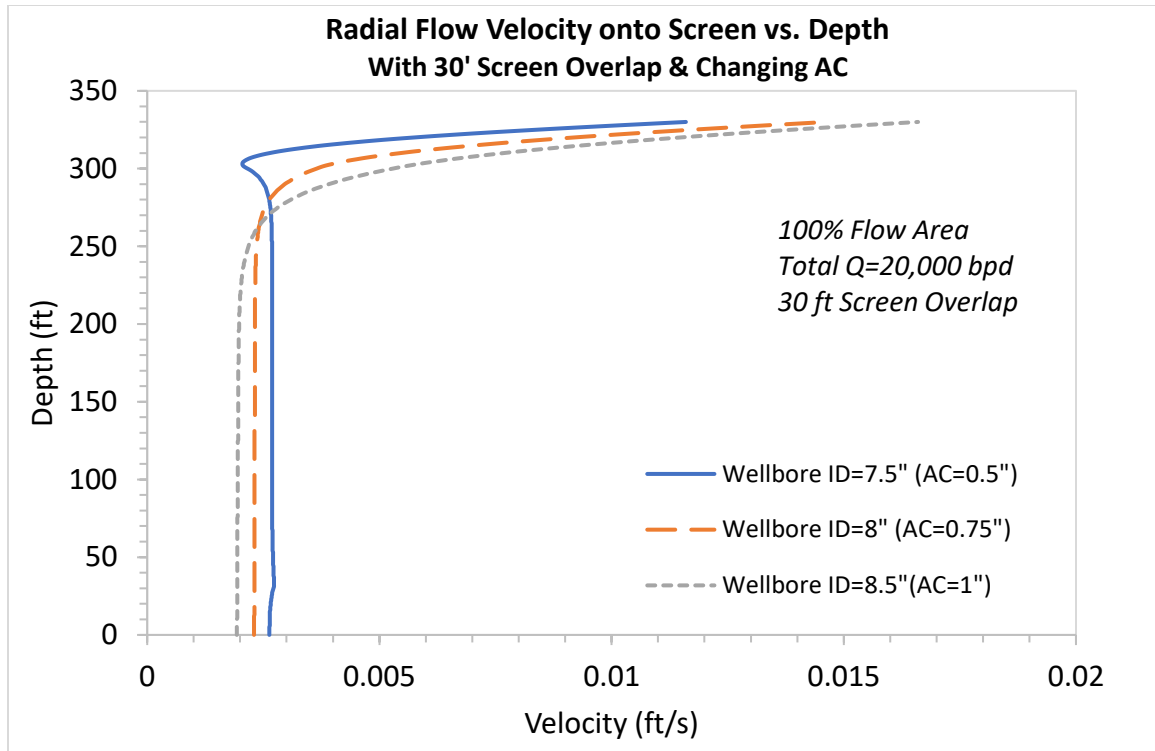Figure 6-46: Radial Flow Velocity onto Screen with 30 ft Screen Overlap & Changing AC

Effects of screen overlap length on annular scouring flow rate and screen impingement flow rate are compared in Figure 6-47 and Figure 6-48, respectively. For the annular flow rate a longer overlap results in a larger maximum annular rate; thereby, increasing the wellbore scouring risks. However, for the screen impingement or radial flow rate converging at the top of the screen, a longer overlap leads to a smaller convergent rate. Figure 6-49 and Figure 6-50 presents the screen convergent velocity (V_a) and the maximum annular scouring velocity (V_{sc}) as a function of screen overlap, respectively, for two different total production rates. As can be seen from these figures, increasing the screen overlap helps reduce the convergent velocity at the top of screen, but there is an optimum screen overlap length beyond which longer overlap would have little to no effects. On the other hand, unlike the convergent velocity, increasing the screen overlap

increases the maximum scouring velocity in the annulus. Therefore, the selection of an optimum screen overlap needs to consider or balance both the wellbore scouring and screen impingement erosion risks.
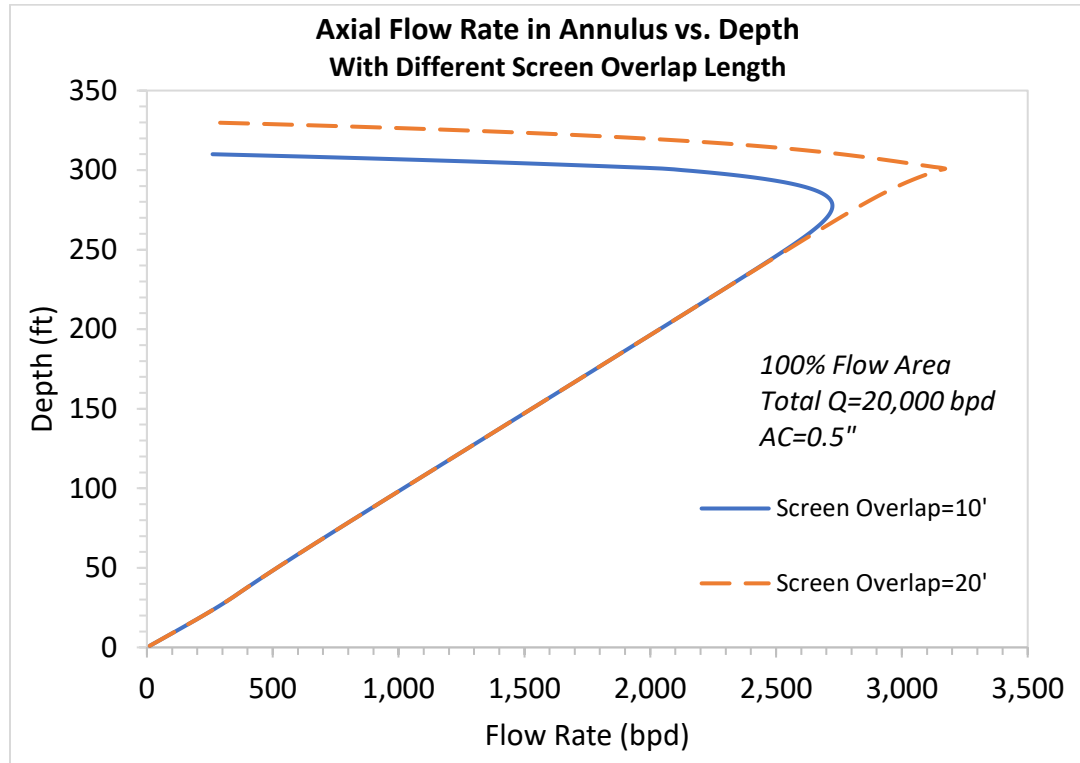
Figure 6-47: Axial Flow Rate Profile in Annulus with Screen Overlap Sensitivity
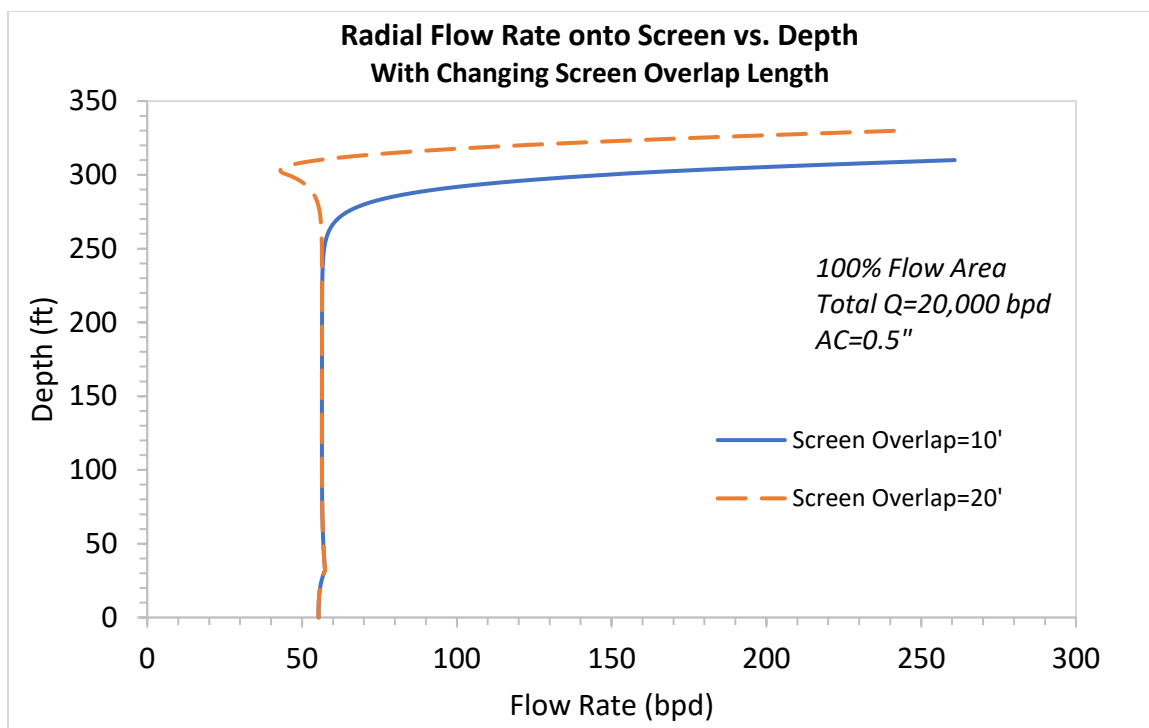
Figure 6-48: Radial Flow Rate onto Screen with Screen Overlap Sensitivity
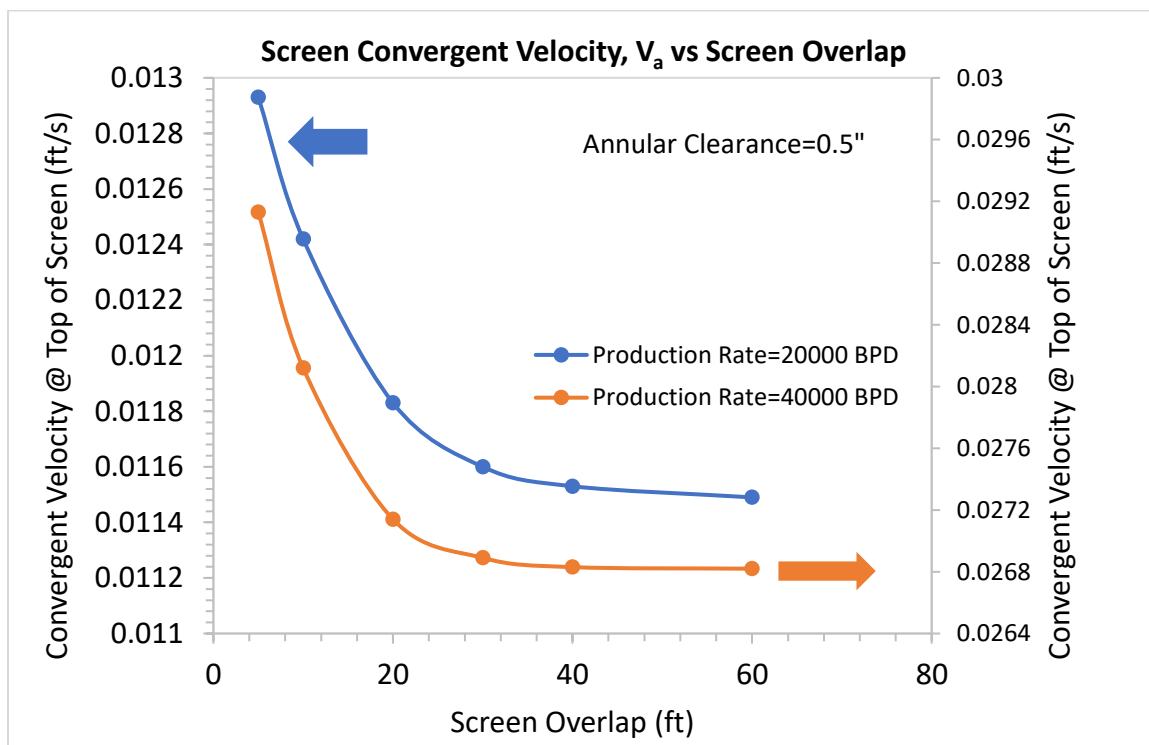
Figure 6-49: Radial Flow Velocity onto top of Screen as a function of Screen Overlap
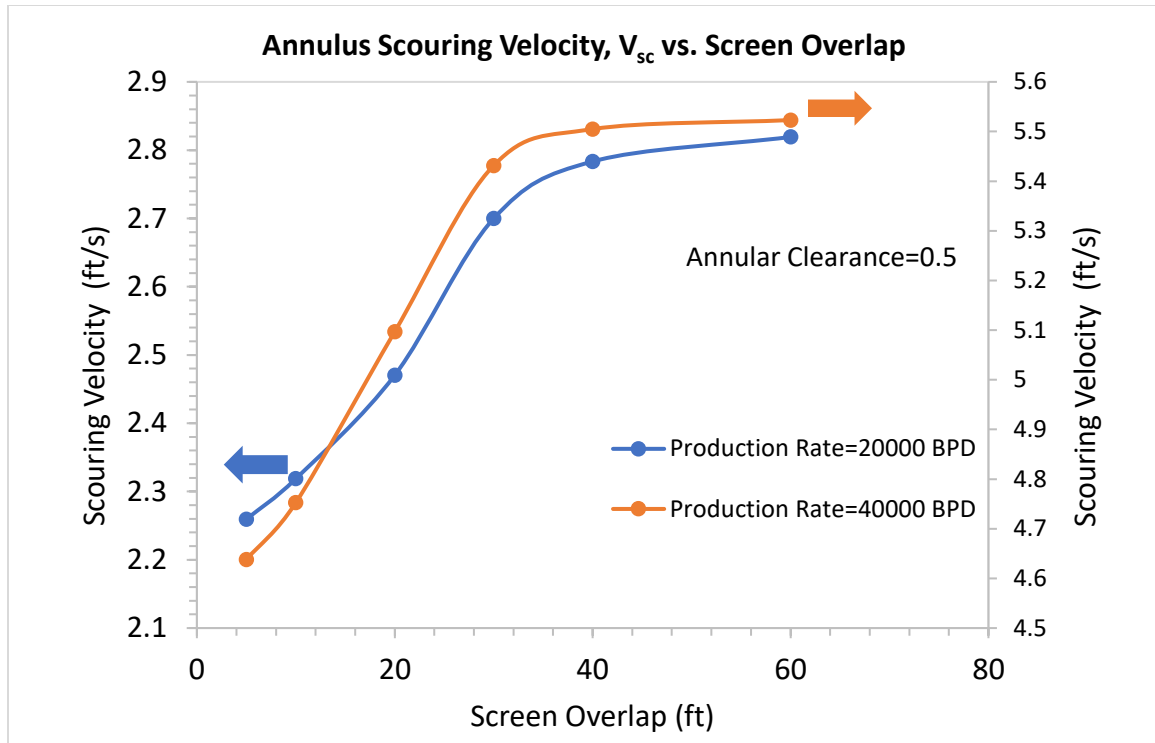
Figure 6-50: Axial Flow Scouring Velocity as a function of Screen Overlap

Case 3: With pinhole flow. The sensitivity simulations in this section are for a total

production rate of 20,000 STB/d. Figure 6-51 presents the radial convergent velocity at

top screen (V_a) as a function of open flow area (OFA) or total pinhole inflow area for cases

with and without screen overlap. Increasing OFA from 25% to 100% of the wellbore

surface area showed only a slight increase of the screen convergent velocity. However, as

shown in Figure 6-48, the screen overlap reduces the convergent velocity. Table 6-11

summarizes these results.

Figure 6-52 and Figure 6-53 present the radial convergent velocity at top screen as a

function of OFA with annular clearance of 0.5 and 1 inch for cases with 30 ft screen

overlap and no overlap, respectively. Again, for a given annulus clearance, OFA has little

effect on the convergent velocity. However, a larger annular clearance leads to higher

annular flow; thereby, higher convergent velocity. Like previous cases, a longer screen

overlap leads to lower convergent velocity.
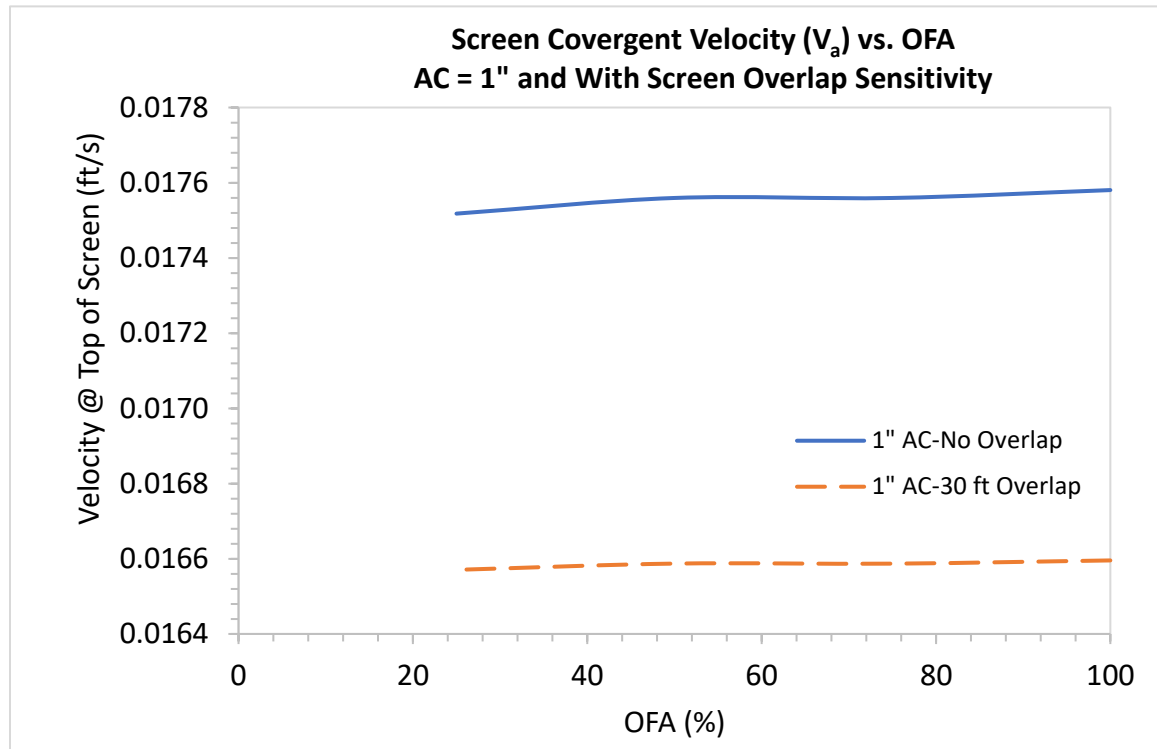
Figure 6-51: Convergent Velocity (V_a) vs. OFA with Screen Overlap Sensitivity

Table 6-11: V_s and V_a vs. OFA with Changing Screen Overlap

Screen Overlap	OFA	AC	V_s	V_a	Percentage
ft	%	inch	ft/s	ft/s	%
0	25	1	0.00268	0.013395	
0	50	1	0.00268	0.013527	0.9749
0	100	1	0.00269	0.013589	0.4606
30	25	1	0.00267	0.011585	
30	50	1	0.00268	0.011597	0.1044
30	100	1	0.00269	0.011604	0.0551
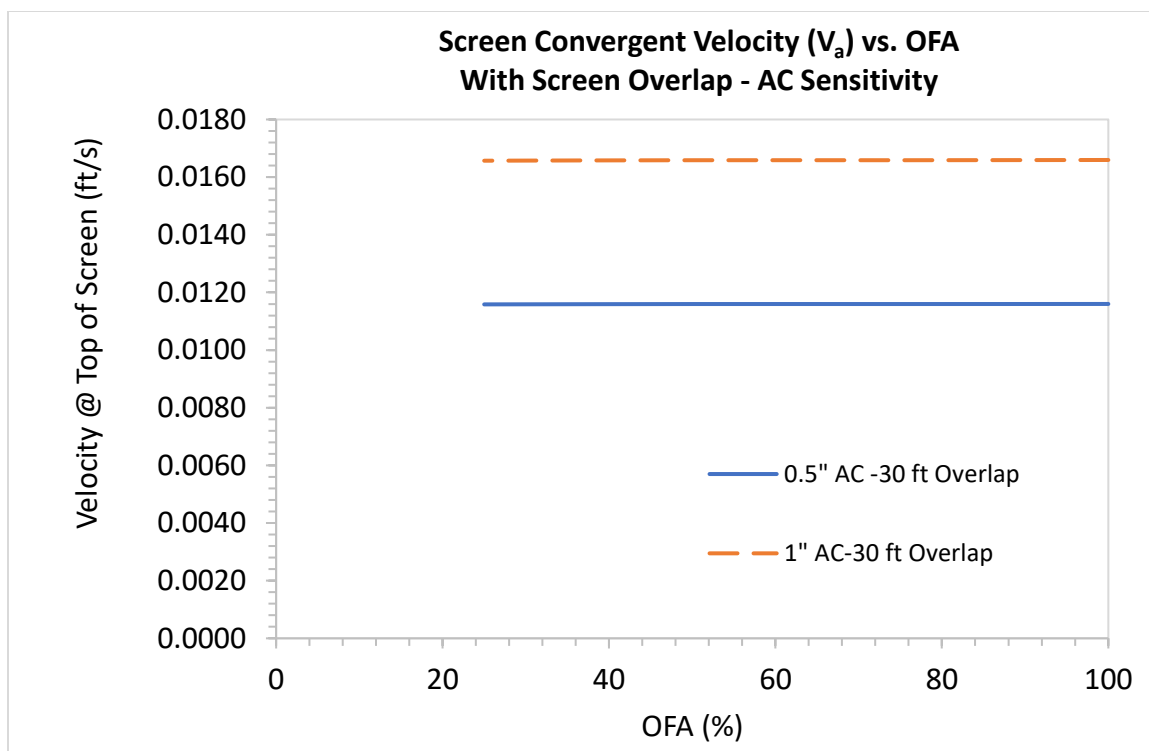
Figure 6-52: Screen Convergent Velocity (V_a) vs. OFA with AC Sensitivity and Screen Overlap
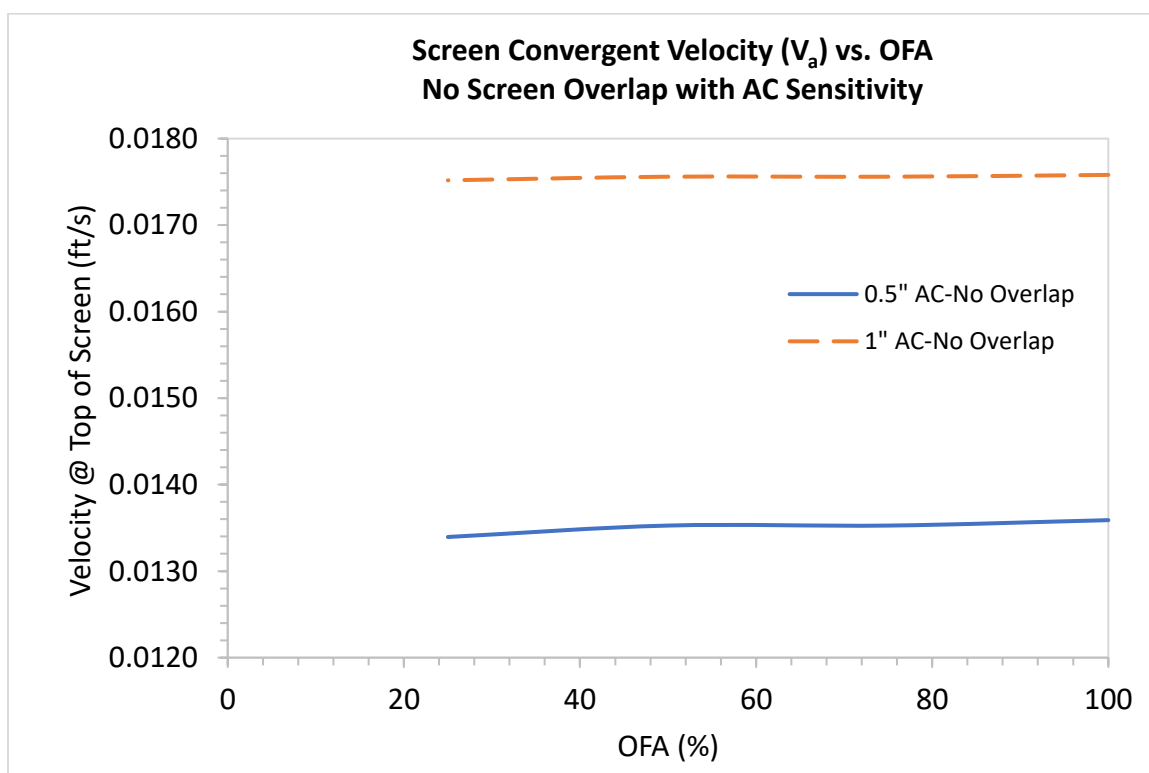
Figure 6-53: Screen Convergent Velocity (V_a) vs. OFA with AC sensitivity and No Screen Overlap

Chapter 7

Summary, Conclusions and Recommendations

7.1 Summary and Conclusions

A production surveillance methodology to monitor and ramp-up production for open hole stand-alone screen (OH-SAS) completion is developed to optimize production by considering risks of production impairment and screen erosion failure. The method is applicable for water and synthetic based drill-in fluids. This new inflow ramp-up method extends the capability to monitor and operate open-hole sand control completions and complements existing cased-hole models. The developed ramp-up methodology for OH-SAS follows the steps below:

- ➢ Identifying the operation criteria to protect the well and develop required inputs for the selected criteria

- ➢ Developing the relationship between completion pressure drop and the pinhole inflow velocity to enable linkage with PTA surveillance. The relationship or model requires filter cake properties of pinhole size or unit flow area (UFA), filter cake thickness (L_{int}) and filter cake permeability (k_{int}). They depend on the drill-in fluid used to drill the completion interval, formation rock and reservoir conditions. These input properties and procedures to obtain them were described.

  - ➢ RPT and CT Scan to determine pinhole size and the filter cake thickness.

➢ Global sensitivity analysis with a reduced order model (ROM) to determine the filter cake permeability without performing fluid flow simulations.

➢ Creating a network model to predict the fluid flow distribution for the OH-SAS completion geometry. The completion interval is discretized into sections and modeled as a network system connecting all the completion parameters (annulus/screen). The network calculations satisfy the conservation of mass and mechanical energy balance. Model predictions were tested initially against a commercial software and showed good match.

➢ Proposing a diagnostic plot of production rate versus completion pressure drop as a surveillance tool for the ramp-up process. By observing the relative positional changes of flow rate and completion pressure drop from successive PBUs of increasing production rates, surveillance engineers can assess the completion performance and screen erosion risks to help decide if continued rate ramp-up would be warranted.

Following are the main conclusions of the study.

1) Sensitivity simulations with different reservoir and completion geometries were studied and evaluated how reservoir and completion variables can impact OH-SAS productivity and completion failure.

2) Pinhole completion pressure drop versus production rate is non-linear and higher than Hawkins's case (wellbore surface area fully open for production).

   ➢ Pinhole with 100% UFA does not equal to Hawkins' case. For a given production rate and completion skin, the pinhole model would forecast a higher completion pressure drop than Hawkins' model. When used in a surveillance mode (i.e., predicting the completion pressure drop for a given flow rate), the application of pinhole model allows higher production rate than Hawkins' model.

3) The application of filter cake properties and PBU data in the pinhole surveillance method showed the filter cake properties have the most effect on the calculated result of the pinhole or concentrated inflow velocity.

4) The filter cake properties are: pinhole size or unit flow area (UFA), filter cake thickness (L_{int}), and filter cake permeability (k_{int})

   ➢ UFA, L_{int} and k_{int} are not independent parameters and should be chosen as a system using RPT, CT Scan, and ROM

   ➢ Use CT scans to get L_{int} and estimate UFA

   ➢ Use RPT and ROM to determine k_{int} with input estimates of L_{int} and UFA

5) Surveillance tool: PTA skin and formation permeability must be used together

6) By applying the wellbore-completion network flow model, the maximum annular scouring velocity (V_{sc}), the maximum screen impingement velocity (V_s) and screen convergent velocity (V_a) at the top of screen assembly can be calculated. Results showed that:

- V_a is always larger than V_s

  - Screen impingement erosion risk is highest at top of screen

  - V_a increases with larger annular clearance

  - V_a reduces with longer screen overlap

    - There is an optimum screen overlap above which V_a is not impacted

- V_{sc} is the highest velocity (about 10 times larger than V_a)

  - This high axial scouring velocity can affect wellbore enlargement and screen erosion due to the combined effects of impingement and scouring.

  - V_{sc} increases with screen overlap

    - There is a maximum screen overlap above which V_{sc} ceases to increase further

7) Adding screen above the pay interval or screen overlap reduces the screen impingement erosion risk but increases the annular scouring risk. When optimizing the screen overlap length, one must balance both V_a and V_{sc}. The effectiveness of screen overlap depends on the wellbore-completion geometry and reservoir fluid properties.

8) The convergent velocities for pinhole and non-pinhole cases were similar. The implementation of pinhole in this methodology only affected the completion pressure drop or the completion impairment risk.

9) From Global sensitivity analysis of the RPT test, internal filter cake permeability

has the most dominant effect and follows by the effect of pinhole diameter. A

reduced order model is developed and the maximum error from the comparison

of the model prediction and the CFD simulations is 8%. This reduced order model

helps determine a consistent set of UFA, L_{int}, and k_{int} that would satisfy RPT

results

7.2 Recommendations

The following recommendations are proposed for future studies

1) The estimation and determination of a representative pinhole size for the ramp-

up model is a major area for improvement. The use of CT-Scan (Figure 6-2)

provides a qualitative estimation of the pinhole flow area or UFA on the test core

plug. This dissertation uses the UFA to determine a single concentric pinhole size

for the ramp-up model. However, multiple pinholes of different diameters might

be distributed in the core plug. Establishing a consistent method to determine an

equivalent pinhole size can improve the application of the pinhole model.

2) The high axial scouring velocity in the annulus raises the risk of wellbore

enlargement and screen erosion due to this flow. Evaluations of rock resistance to

axial scouring and screen erosion resistance from the combined effects of axial

and radial flow velocity warrant further considerations.

3) As production rate increases the associated high completion pressure drop raises

the risk of wellbore collapse. Similarly, as reservoir depletion takes place following

ramp-up the extension of pinhole method with wellbore stability is another possible area of study.

4) Extend the existing ramp-up method to Open-Hole Gravel Pack (OH-GP) completion.

5) Improve the network model to address completion with the top of screen inside or below the completion interval.

References

Andrews, J. S., Kittilsen, P., Låhne, T., & Antonsen, J. R. (2017). "Optimizing bean-up procedure after well shut-in. Simple rock mechanical aspects and operational guidelines". *Society of Petroleum Engineers - SPE Bergen One Day Seminar 2017*. https://doi.org/10.2118/185906-ms

Bailey, L., Boek, E., Jacques, S., Boassen, T., Selle, O., Argillier, J.-F., & Longeron, D. (1999). "Particulate Invasion From Drilling Fluids". *SPE European Formation Damage Conference*, *5*(4), 412–419. https://doi.org/10.2118/54762-MS

Burton, B., & Hodge, R. (2010). "Comparison of inflow performance and reliability of open hole gravelpacks and open hole stand-alone screen completions". *Proceedings - SPE Annual Technical Conference and Exhibition*, *6*, 4567–4604. https://doi.org/10.2118/135294-ms

Bybee, K. (2006). "Sand Production in the Statfjord Field". *Journal of Petroleum Technology*, 58(09), 107–112. https://doi.org/10.2118/0906-0107-jpt

Cameron, J., Zaki, K., Jones, C., & Lazo, A. (2018). "Enhanced flux management for sand control completions". Proceedings - SPE Annual Technical Conference and Exhibition, 2018-September. https://doi.org/10.2118/191598-ms

Cerasi, P., & Soga, K. (2001). "*Failure modes of drilling fluid filter cake*". Géotechnique, 51(9), 777–785. https://doi.org/10.1680/geot.2001.51.9.777

Chanpura, R. A., Hodge, R. M., Andrews, J. S., Toffanin, E. P., Moen, T., & Parlar, M.

(2010). "State of the art screen selection for standalone screen applications".

Proceedings - SPE International Symposium on Formation Damage Control, 2, 570–

587. https://doi.org/10.2118/127931-ms

COMSOL Multiphysics® v. 5.4. www.comsol.com. COMSOL AB, Stockholm, Sweden.

Constien, V. G. (2008). "Evaluation of formation damage/completion impairment

following dynamic filter-cake deposition on unconsolidated sand". Proceedings - SPE

International Symposium on Formation Damage Control, 2, 910–919.

https://doi.org/10.2118/112497-ms

Economides, M.J. , Hill, A. D., C. Ehlig-Economides, and D. Zhu, "Petroleum production

systems". New Jersey: Pearson Education International, 2013

Economides, C., Tosic, & Economides, M. (2008). "Foolproof Completions for High-Rate

Production Wells". SPE International Symposium and Exhibition of Formation

Damage Control, Lafayette, LA,

Furgier, J. N., Viguerie, B., Aubry, E., & Rivet, P. (2013). "Stand alone screens: What key

parameters are really important for a successful design?". *SPE - European

Formation Damage Conference, Proceedings, EFDC*, *2*, 869–880.

https://doi.org/10.2118/165170-ms

Furui K, Zhu D, Hill AD. "A Comprehensive Model of Horizontal Well Completion

Performance". Proc - *SPE Annu Tech Conf Exhib*. 2003:3039-3054.

Geilikman, M. B., Dria, D. E., Stewart, D. R., & Wong, G. K. (2005). "Bean-up guidelines

for sand-control completions". *Proceedings - SPE Annual Technical Conference and Exhibition*, 1737–1744. https://doi.org/10.2523/95870-ms

Hawkins, M. F. (1956). *"A Note on the Skin Effect". Journal of Petroleum Technology*, *8*(12), 65–66. https://doi.org/10.2118/732-g

Hodge, R., Burton, R., Fischer, C., & Constien, V. (2010). "Productivity impairment of openhole gravel packs caused by drilling-fluid filtercake". *Proceedings - SPE International Symposium on Formation Damage Control*, *2*, 841–861. https://doi.org/10.2118/128060-ms

Karantinos, E., & Sharma, M. M. (2017). "Choke management under wellbore, completion and reservoir constraints". *Proceedings - SPE Annual Technical Conference and Exhibition*, (October), 9–11. https://doi.org/10.2118/187190-ms

Karantinos, E., Sharma, M. M., Ayoub, J. A., Parlar, M., & Chanpura, R. A. (2015). "A general method for the selection of an optimum choke management strategy". *SPE - European Formation Damage Conference, Proceedings, EFDC*, *2015-Janua*, 483–500. https://doi.org/10.2118/174196-ms

Li, Q., An, S., & Gedra, T. (2003). "Solving natural gas loadflow problems using electric loadflow techniques". *Proc. of the North American Power Symposium*. Retrieved fromhttp://citeseerx.ist.psu.edu/viewdoc/download?doi=10.1.1.80.9709&rep=rep1&type=pdf

Mahmoudi, M., Roostaei, M., Fattahpour, V., Uzcatequi, A., Cyre, J., Sutton, C., &

Fermaniuk, B. (2018). "Standalone sand control failure: The role of wellbore and near wellbore hydro-thermo-chemical phenomenon on the plugging and the flow performance impairments of the standalone sand screen". Society of Petroleum Engineers - SPE Thermal Well Integrity and Design Symposium 2018, TWID 2018. https://doi.org/10.2118/193355-ms

Morita, N., Davis, E., & Whitebay, L. (1998). "Guidelines for solving sand problems in water injection wells". Proceedings - SPE International Symposium on Formation Damage Control, 189–200. https://doi.org/10.2523/39436-ms

Morrison, F. A. (2013)." An Introduction to Fluid Mechanics", Cambridge University Press, 2013.

Overveldt, A. S. Van, Guo, H., Blok, G. De, Bedrikovetsky, P., & Pacelli, L. J. (2012). *SPE 151856 "A CT Scan Aided Core-flood Study of the Leak-off Process in Oil-based Drilling Fluids*". 1–25.

Parlar, M., Tibbles, R. J., Gadiyar, B., & Stamm, B. (2016). "A new approach for selecting sand-control technique in horizontal openhole completions". SPE Drilling and Completion, 31(1), 4–15. https://doi.org/10.2118/170691-pa

Patel, M. C., & Singh, A. (2016). "Near wellbore damage and types of skin depending on mechanism of damage". *Proceedings - SPE International Symposium on Formation Damage Control*, *2016-Janua*. https://doi.org/10.2118/179011-ms

Procyk, A., Gou, X., Marti, S. K., Burton, R. C., Knefel, M., Dreschers, D., … Glatt, E.

(2015). "Sand control screen erosion: Prediction and avoidance". Proceedings - SPE

Annual Technical Conference and Exhibition, 2015-Janua, 1562–1587.

https://doi.org/10.2118/174837-ms

Raoni, R., Secchi, A. R., & Biscaia, E. C. (2017). *"Novel method for looped pipeline

network resolution". Computers and Chemical Engineering*, *96*, 169–182.

https://doi.org/10.1016/j.compchemeng.2016.10.001

Rezaei, A., Nakshatrala, K. B., Siddiqui, F., Dindoruk, B., & Soliman, M. (2018)." *A global

sensitivity analysis and reduced order models for hydraulically-fractured horizontal

wells*". Retrieved from http://arxiv.org/abs/1812.03424

Richard, B. M., Montagna, J. M., & Penberthy, W. L. (1997). "*Stand-alone screens vary in

effectiveness*". Oil and Gas Journal, *95*(32), 63–69.

Saucier, R. J. (1974). "*Considerations in Gravel Pack Design*". JPT, Journal of Petroleum

Technology, 26, 205–212. https://doi.org/10.2118/4030-PA

Sobol, I. M. (1993). "*Sensitivity estimates for nonlinear mathematical models.

Mathematical modelling and computational experiments*". *1*(4), 407–414.

Sobol, I. M. (2001). *"Global sensitivity indices for nonlinear mathematical models and

their Monte Carlo estimates". Mathematics and Computers in Simulation*, *55*(1–3),

271–280. https://doi.org/10.1016/S0378-4754(00)00270-6

Sudret, B. (2008). *"Global sensitivity analysis using polynomial chaos expansion".

Reliability Engineering & System Safety*, *93*(7), 964–979.

https://doi.org/10.1016/j.ress.2007.04.002

Suri, A., & Sharma, M. M. (2010). "An Improved Laboratory Method to Estimate Flow

Initiation Pressures and Near Wellbore Return Permeabilities". *SPE Western*

Regional Meeting, *1*(1994), 35–53. https://doi.org/10.2118/132098-MS

Tiffin, D. L., Stein, M. H., & Wang, X. (2003). "Drawdown Guidelines for Sand Control

Completions". *Proceedings - SPE Annual Technical Conference and Exhibition*,

3901–3910. https://doi.org/10.2523/84495-ms

Van Everdingen, A. F., & Hurst, W. (1949). "*The Application of the Laplace*

Transformation to Flow Problems in Reservoirs". *Journal of Petroleum Technology*,

1(12), 305–324. https://doi.org/10.2118/949305-g

Van Zanten, R., Horton, D., & Tanche-Larsen, P. B. (2011). "Engineering drill-in fluids to

improve reservoir producibility". *Society of Petroleum Engineers - 9th European*

Formation Damage Conference 2011, *1*(June), 535–542.

https://doi.org/10.2118/143845-ms

Vaziri, H., Barree, B., Xiao, Y., Palmer, I., & Kutas, M. (2002). "What is the Magic of Water

in Producing Sand?". *Proceedings - SPE Annual Technical Conference and Exhibition*,

2973–2985. https://doi.org/10.2523/77683-ms

Vaziri, H., Xiao, Y., & Palmer, I. (2002). "Assessment of several sand prediction models

with particular reference to HPHT wells". *Proceedings of the SPE/ISRM Rock*

Mechanics in Petroleum Engineering Conference, 606–617.

https://doi.org/10.2523/78235-ms

Walton, I. C. (2000). "Optimum underbalance for the removal of perforation damage" .
SPE Reservoir Engineering (Society of Petroleum Engineers), (A), 373–386.
https://doi.org/10.2523/63108-ms

Wong, G. K., Fair, P. S., Bland, K. F., & Sherwood, R. S. (2003). "Balancing Act: Gulf of
Mexico Sand Control Completions Peak Rate Versus Risk of Sand Control Failure".
Proceedings - SPE Annual Technical Conference and Exhibition, 3921–3931.
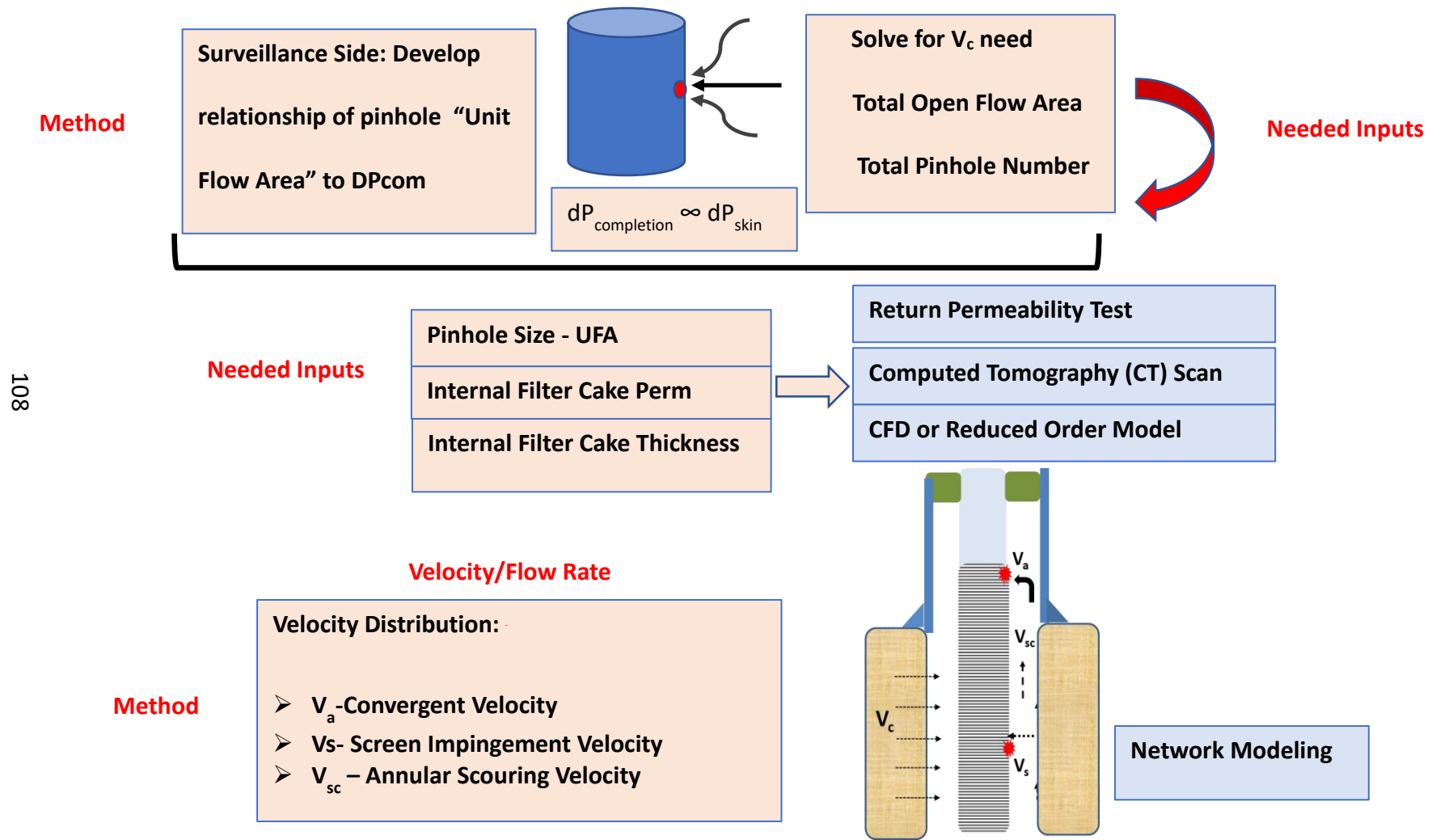https://doi.org/10.2523/84497-ms

Zain, Z. M., Suri, A., & Sharma, M. M. (2000). "Mechanisms of Mud Cake Removal During
Flowback". *SPE International Symposium on Formation Damage Control*.
https://doi.org/10.2118/58797-MS

Appendix A: Production Ramp-up Components Flowchart

Method

Surveillance Side: Develop relationship of pinhole "Unit Flow Area" to DPcom

$dP_{completion} \propto dP_{skin}$

Solve for V_c need

Total Open Flow Area

Total Pinhole Number

Needed Inputs

Needed Inputs

| Pinhole Size - UFA |
| Internal Filter Cake Perm |
| Internal Filter Cake Thickness |

| Return Permeability Test |
| Computed Tomography (CT) Scan |
| CFD or Reduced Order Model |

Velocity/Flow Rate

Method

Velocity Distribution:

➢ V_a-Convergent Velocity
➢ Vs- Screen Impingement Velocity
➢ V_{sc} – Annular Scouring Velocity

V_a

V_{sc}

V_c

V_s

Network Modeling

Appendix B: Mathematical Formulation of Sobol Technique

Mathematical formulation of this technique for an arbitrary function f is summarized by Rezaei et al. as follows (Rezaei, Nakshatrala, Siddiqui, Dindoruk, & Soliman, 2018):

$$y = f(x), \qquad \text{(B.1)}$$

at above equation, x is a set of input parameters on the n-dimensional hypercube such that:

$$\Omega^n := \{x | 0 \leq x_i \leq, i = 1, \dots, n\}.$$

Function f can be written as the ANAVO representation (abbreviated as Analysis of Variance)

$$f(x) = f_0 + \sum_{s=1}^{n} \sum_{i_1 < \dots < i_s}^{n} f_{i_1 \dots i_s}(x_{i_1}, \dots, x_{i_s}), \quad 1 \leq i_1 < \dots < i_s \leq n. \quad \text{(B.2)}$$

To increase order of Sobol functions above equation is written as

$$f(x) = f_0 + \sum_{i=1}^{n} f_i(x_i) + \sum_{i=1}^{n} \sum_{j=i+1}^{n} f_{ij}(x_i, x_j) + \dots + f_{i \dots n}(x_1, \dots, x_n). \quad \text{(B.3)}$$

Following statements should be satisfied in order to make the above equation applicable.

1) f_0 should be a constant.

2) The integral of each member over its own variables = 0

$$\int_0^1 f_{i_1 \dots i_s}(x_{i_1}, \dots, x_{i_s}) dx_k = 0 \quad \forall k = i_1, \dots, i_s \quad \text{(B.4)}$$

3) All of the members in Eq. B.3 are orthogonal, meaning that if $(i_1, ..., i_s) \neq (j_1, ..., j_t)$

then

$$\int_{\Omega^n} f_{i_1....i_s} f_{j_1....j_t} dx = 0, \tag{B.5}$$

where;

$$f_0 = \int_{\Omega^n} f(x) \, dx = 0, \tag{B.6}$$

$$f_i(x_i) = \int_{\Omega^n} f(x_i, x_{\sim i}) \, dx_{\sim i} - f_0, \tag{B.7}$$

and $\quad f_{ij}(x_i, x_j) = \int_{\Omega^{n-2}} f(x_i, x_j, x_{\sim ij}) \, dx_{\sim ij} - f_0 - f_i(x_i) - f_j(x_j), \tag{B.8}$

where $x_{\sim i}$ is the vector corresponding to all variables except x_i in the input set x, and $x_{\sim ij}$

is the vector corresponding to all variables except x_i and x_j in the input set x. Assuming

that $f(x)$ is square integrable, total variance of f is given by

$$D = V[f] = \int_{\Omega^n} f^2(x) \, dx - f_0^2 = \sum_{s=1}^{n} \sum_{i_1 < \cdots < i_s}^{n} f^2_{i_1....i_s}(x_{i_1}, ..., x_{i_5}) \, dx_{i_1} .... \, dx_{i_s}. \tag{B.9}$$

Equation 3.9 can also be written in terms of the partial variances of f as

$$D = \sum_{s=1}^{n} \sum_{i_1 < \cdots < i_s}^{n} D_{i_1....i_s} = \sum_{i=1}^{n} D_i + \sum_{i=1}^{n} \sum_{j=i+1}^{n} D_{ij} + ... D_{1...n} \quad , \tag{B.10}$$

where $D_i, D_{ij}, ..., D_{i...j}$ can be calculated by integrating the corresponding Sobol functions

as follows:

$$D_i = \int_{\Omega^1} f_i^2(x_i) \, dx_i, \tag{B.11}$$

$$D_{ij} = \int_{\Omega_2} f_{ij}^2(x_i, x_j) \, dx_i dx_j, \tag{B.12}$$

110

.

.

.

and
$$D_{i_1....i_s} = \int_\Omega f^2_{i_1...i_s}(x_{i_1}, \ldots, x_{i_s}) \, dx_{i_1} \ldots dx_{i_s} \qquad \text{(B.13)}$$

From the descriptions, Sobol indices are the ratio of the partial variances to the total variance as

$$S_i = \frac{D_i}{D} \; , \qquad \text{(B.14)}$$

$$S_{ij} = \frac{D_{ij}}{D} \, , \qquad \text{(B.15)}$$

.

.

and
$$S_{i_1...i_s} = \frac{D_{i_1...i_s}}{D} \qquad . \qquad \text{(B.16)}$$

In this preparation, higher indices imply a higher effect on the variation of the output parameter. Also, Sobol indices are non-negative indices that have the below characteristic:

$$\sum_{s=1}^{n} \sum_{i_1 < \cdots < i_s}^{n} S_{i_1....i_s} = \sum_{i=1}^{n} S_i + \sum_{i=1}^{n} \sum_{j=i+1}^{n} S_{ij} + \ldots . S_{1...n} = 1 \qquad \text{(B.17)}$$

Sobol indices allows conducting evaluations according to their Sobol indices to order input variables.

Sobol Method for Complex Functions

A Monte Carlo integration is necessary to calculate the integrals for the functions which are not polynomials that are required by Sobol analysis (Sobol 1993, Witarto et al.). Sobol functions can be calculated as follows:

$$\bar{f_0} = \frac{1}{N}\sum_{m=1}^{N} f(x_m), \tag{B.18}$$

$$\bar{D} = \frac{1}{N}\sum_{m=1}^{N} f^2(x_m) - \bar{f_0}^2, \tag{B.19}$$

$$\bar{D_\iota} = \frac{1}{N}\sum_{m=1}^{N} f(x_m)f(x_{im}, x_{\sim im}^c) - \bar{f_0}^2, \tag{B.20}$$

and
$$\overline{D_{\iota J}} = \frac{1}{N}\sum_{m=1}^{N} f(x_m)f(x_{im}, x_{\sim im}^c) - \bar{D_\iota} - \bar{D_J} - \bar{f_0}^2. \tag{B.21}$$

Sobol indices can be calculated by following steps:

1) Calculate $D_{i...j}$

2) Enter the calculated $D_{i...j}$ values into Equation

Complex functions can be represented by Sobol analysis as a simplified equation. This can be done by choosing Sobol function to a certain level of accuracy based on Sobol index values. Rezai et al. (2018) gave the details of the above procedure and equations (Rezai et al., 2018).

Appendix C: Velocity Profile Simulator

This section presents the screenshots from the simulator and describes the equation utilized in the well network system for sand screen radial pressure drop calculations. Required inputs used for the flow rate and velocity profile simulations are given in Figure C-1. The output tab screenshot from the simulator is given in Figure C-2.

Screen coefficients A and B are needed to calculate the screen pressure drop across the screen. Richard et al. (1997) conducted experiments and provided curves for different sand screen types. Figure C-3 presents a relationship between flow capacities of 1-ft long length for a conventional wire-wrapped screen. Required coefficients A & B for the simulator are extracted from the curve as 455.73 and 21.36, respectively.
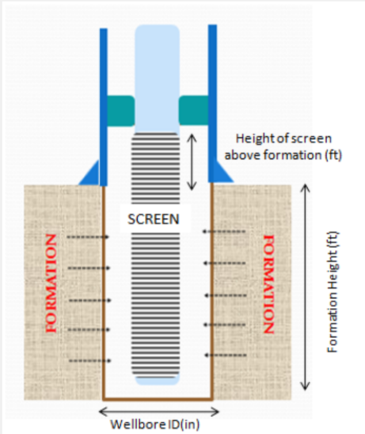
Figure C-1: Software Input Screenshot
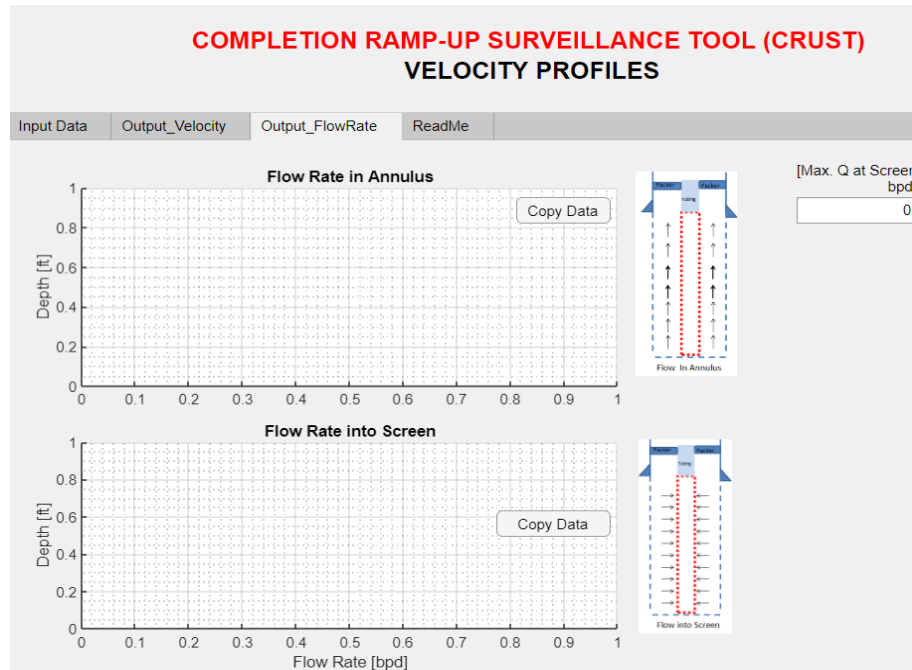
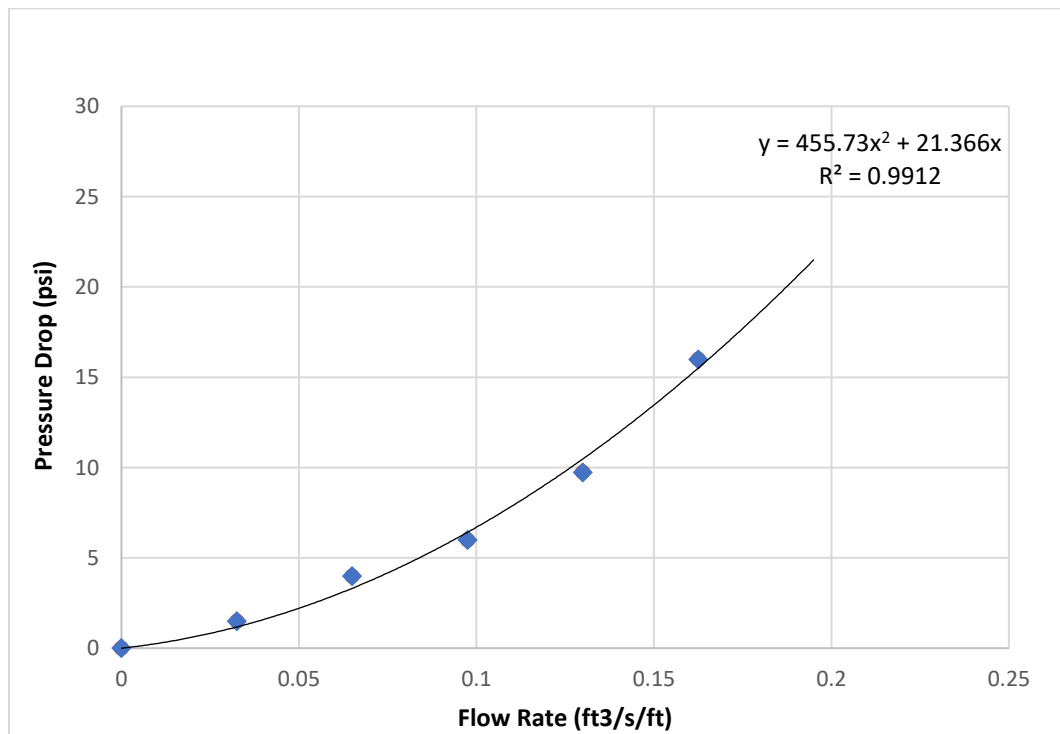Figure C-2: Software Output Section Screenshot

$$y = 455.73x^2 + 21.366x$$
$$R^2 = 0.9912$$

Figure C-3: Flow Rate vs. Radial Screen Pressure Drop

114